

Copyright

by

Mahmood Shakiba

2014

**The Thesis Committee for Mahmood Shakiba**  
**Certifies that this is the approved version of the following thesis:**

**Modeling and Simulation of Fluid Flow in Naturally and Hydraulically  
Fractured Reservoirs Using Embedded Discrete Fracture Model  
(EDFM)**

**APPROVED BY**  
**SUPERVISING COMMITTEE:**

**Supervisor:**

---

Kamy Sepehrnoori

---

Larry W. Lake

**Modeling and Simulation of Fluid Flow in Naturally and Hydraulically  
Fractured Reservoirs Using Embedded Discrete Fracture Model  
(EDFM)**

**by**

**Mahmood Shakiba, B.S.P.E**

**Thesis**

Presented to the Faculty of the Graduate School of  
The University of Texas at Austin  
in Partial Fulfillment  
of the Requirements  
for the Degree of

**Master of Science in Engineering**

**The University of Texas at Austin  
December 2014**

## **Dedication**

To my parents, my sister, and my brother

## Acknowledgements

I would like to express my immense gratitude to Professor Kamy Sepehrnoori, my research supervisor, for his inspiring guidance, insightful ideas, and continuous encouragement throughout this research. He provided me with invaluable advice and remarkable support which contributed to my progress in this research. I am indebted to Professor Larry W. Lake for providing valuable comments and feedback on my thesis.

Furthermore, I would like to thank the staff of the Petroleum and Geosystems Engineering Department, Frankie Hart, Dr. Roger Terzian, Tim Guinn, John Cassibry, and Glen Baum for their technical and administrative support.

My special gratitude goes to Ali Moinfar and Jose Sergio Cavalcante for their helpful inputs and discussions regarding the Embedded Discrete Fracture Model. I would like to thank my friends, Aboulghasem Kazemi Nia and Mojtaba Ghasemi Doroh for their technical comments and knowledge sharing regarding the UTCOMP and UTCHEM simulators. I also acknowledge Dr. Chowdhury Mamun for careful review and comments on my thesis. Additionally, I extend my appreciation to all my friends, colleagues and officemates for the memorable experience we shared.

I sincerely appreciate the financial support provided by the members of the Reservoir Simulation Joint Industry Project (RSJIP) at the Center for Petroleum and Geosystems Engineering at The University of Texas at Austin.

Finally, I am extremely grateful to my parents for encouraging me in all of my pursuits and inspiring me to follow my dreams. I am indebted to my entire family without whom none of this would have been possible.

## **Abstract**

# **Modeling and Simulation of Fluid Flow in Naturally and Hydraulically Fractured Reservoirs Using Embedded Discrete Fracture Model (EDFM)**

Mahmood Shakiba, M.S.E

The University of Texas at Austin, 2014

Supervisor: Kamy Sepehrnoori

Modeling and simulation of fluid flow in fractured subsurface systems has been steadily a popular topic in petroleum industry. The huge potential hydrocarbon reserve in naturally and hydraulically fractured reservoirs has been a major stimulant for research developments in this field. Although several models have found limited applications to study fractured reservoirs, still comprehensive models are required to be applied for more complicated problems. A recently developed Embedded Discrete Fracture Model (EDFM) incorporates the advantages of two of the well-known models, the dual continuum and the discrete fracture models, to investigate more complex fracture geometries. In EDFM, each fracture is embedded inside the matrix grid and is discretized by the cell boundaries. This approach introduces a robust methodology to represent the fracture planes explicitly in the computational domain. As part of this research, the EDFM was implemented in two of The University of Texas in-house reservoir simulators, UTCOMP and UTGEL, to provide the capability of modeling and simulation

of a broad range of reservoir engineering applications in naturally and hydraulically fractured reservoirs. To validate this work, comparisons were made against a fine-grid simulation and a semi-analytical solution. Also, the simulation results were compared to the results obtained from EDFM implementation in the GPAS reservoir simulator for more complicated fracture geometries. In all of the examples, good agreements were observed. To further illustrate the applications and capabilities of UTCOMP- and UTGEL-EDFM, several case studies were presented. First, synthetic reservoir models with networks of fractures were generated to study the impact of well placement. It was shown that considering the configuration of the background fracture networks can significantly improve well placement design and also can maximize oil recovery. The capillary imbibition effect was then investigated for the same reservoir models to display its effect on incremental oil recovery. Furthermore, UTCOMP-EDFM was applied for hydraulic fracturing design where the performances of a simple and a complex fracture networks were evaluated in reservoirs with different rock matrix permeabilities. Accordingly, the simulation outcomes indicated that a complex network is an ideal design for a very low permeability reservoir, while a simple network results in a higher recovery for the reservoir with moderate permeability. Finally, UTGEL-EDFM was employed to optimize a conformance control process. Several injection timings and several gel concentrations were specified for water flooding processes and their impact on oil recovery was evaluated henceforth.

## Table of Contents

List of Tables .....	x
List of Figures .....	xi
Chapter 1: Introduction .....	1
Chapter 2: Literature Review .....	6
2.1 Dual Porosity Models .....	7
2.2 Discrete Fracture Models .....	15
Chapter 3: Overview of UTCOMP and UTGEL Reservoir Simulators .....	20
3.1 UTCOMP Reservoir Simulator.....	20
3.1.1 Governing Formulations .....	21
3.1.1.1 Mass Conservation and Auxiliary Equations .....	21
3.1.1.2 Pressure Equation .....	24
3.1.2 Initial and Boundary Conditions .....	26
3.2 UTGEL Reservoir Simulator .....	28
3.2.1 Governing Formulations .....	29
3.2.1.1 Mass Conservation Equation.....	29
3.2.1.2 Pressure Equation .....	30
3.2.1.3 Energy Conservation Equation.....	31
3.2.2 Initial and Boundary Conditions .....	32
Chapter 4: Overview of Embedded Discrete Fracture Model (EDFM) and the Implementation Approach .....	33
4.1 Dual Continuum and Discrete Fracture Models Synergy .....	33
4.2 Embedded Discrete Fracture Model (EDFM).....	37
4.2.1 Methodology .....	40
4.2.2 Fracture Connections in EDFM .....	48
4.2.2.1 Matrix-Fracture Connection.....	50
4.2.2.2 Fracture-Fracture Connection (of two Different Fracture Planes).....	52

4.2.2.3	Fracture-Fracture Connection (of the Same Fracture Plane) ....	54
4.2.2.4	Well-Fracture Intersection .....	55
4.3	Preprocessing Code.....	58
4.4	Non-Neighboring Connection Methods.....	60
4.4.1	Method I.....	63
4.4.2	Method II .....	65
4.4.3	Method III (EDFM) .....	66
4.5	Modified Reservoir Simulators Formulations .....	69
Chapter 5:	Model Verification .....	76
5.1	Fine-Grid Simulation .....	76
5.2	Arbitrary Oriented Fractures.....	83
5.3	Inclined Fractures.....	88
5.4	Well-Fracture Intersection (Semi-Analytical Solution).....	92
Chapter 6:	Applications of UTCOMP-EDFM and UTGEL-EDFM.....	97
6.1	Water Flooding in Fractured Reservoirs.....	97
6.1.1	Well Placement .....	98
6.1.2	Capillary Pressure Effect .....	108
6.2	Hydraulic Fracturing Design and Treatment .....	118
6.3	Injection Conformance Control .....	127
6.3.1	Preformed Particle Gel (PPG).....	128
6.3.1.1	Permeability Reduction Factor .....	129
6.3.1.2	Viscosity .....	130
6.3.2	PPG Injection Timing .....	131
6.3.3	PPG Concentration.....	137
Chapter 7:	Summary, Conclusions, and Recommendations.....	143
7.1	Summary and Conclusions .....	143
7.2	Recommendations.....	146
Appendix:	Semi-Analytical Solution.....	148
References.....		151

## List of Tables

Table 5.1: Gridding information for the Fine-grid and EDFM simulations is presented in this table. Four different cases are considered for grid sensitivity.....	79
Table 5.2: Rock and fluid properties for the reservoir model in section 5.1.....	79
Table 5.3: Simulation run times for the examples presented in section 5.1.....	79
Table 5.4: Rock and fluid properties for the reservoir model in section 5.2. The relative permeability curves are straight lines for the fractures.....	85
Table 5.5: Rock and fluid properties for the reservoir model in section 5.4.....	95
Table 6.1: Rock and fluid properties of the reservoir model in section 6.1. The relative permeability curves are straight lines for fractures.....	100
Table 6.2: Two sets of parameters for capillary pressure calculations. The second set results in strong capillary pressure effects.....	110
Table 6.3: Rock and fluid properties of the reservoir model in section 6.3.2. The relative permeability curves are straight lines for the fractures.....	133

## List of Figures

Figure 1.1: Microseismic monitoring of a hydraulic fracturing job (Rahimi Zeynal <i>et al.</i> 2014). The green lines are the horizontal wells and the pink dots are microseismic events. Each event represents a rock failure. The fracture network is constructed based on the microseismic map.....	2
Figure 2.1: Idealization made by dual porosity model for a naturally fractured reservoir (Warren and Root (1963)). .....	8
Figure 2.2: Stacked and Nested discretizations used in MINC approach (Gilman (1986)).....	14
Figure 2.3: (a) Schematic of a discretization used by finite-element method and (b) a case study with 6 fractures (Karimi-Fard and Firoozabadi (2003)).....	17
Figure 2.4: A discretization example used in modeling a fractured porous medium with control-volume finite-difference formulation (Karimi <i>et al.</i> (2004)). To apply finite-difference scheme, a node is considered at the center of each element.....	18
Figure 4.1: Configuration of the dual continuum approach: (a) Schematic of a naturally fractured reservoir, (b) and the corresponding coupled matrix and fracture domains.....	34
Figure 4.2: Schematic of a discrete fracture model (Karimi-Fard <i>et al.</i> (2004)): (a) A naturally fractured reservoir, and (b) the corresponding unstructured grid, in which the red ellipses highlight the regions with highly refined cells .....	36

Figure 4.3: Representation of a fractured reservoir model using the EDFM concept:	
(a) Angled view highlighting vertical and inclined fractures, and (b) top view.....	42
Figure 4.4: Color-coded illustration of the gridblocks intersected by the matching color fractures in the (a) first, (b) second, (c) and third layers. The gridblocks with multiple intersections are shown in purple. .....	43
Figure 4.5: Possible shapes of the intersection between a plane and a cube: (a) rectangle (intersection points are on the parallel cube edges) (b) rectangle (intersection points are on the adjacent cube edges) (c) triangle (d) pentagon (e) hexagon. ....	44
Figure 4.6: Fracture planes discretization for the example reservoir model. (a) Red vertical fracture plane is composed of only rectangular segments. (b) Blue inclined fracture plane with 15 degree dip angle is composed of triangular, quadrilateral, pentagonal, and hexagonal segments. (c) Green inclined fracture with 10 degree dip angle is composed of triangular, quadrilateral, pentagonal, and hexagonal segments.....	46
Figure 4.7: Schematic of a fracture-matrix connection, known as NNC type I. (a) This intersection is considered in (b) the computational domain through a non-neighboring connection with an equivalent transmissibility factor ( $T_{m-f}$ ). .....	51
Figure 4.8: Discretized fracture planes with track of the intersection line. Segments containing the matching color part of the intersection line are connected in the computational domain.....	53

Figure 4.9: Schematic of a fracture-fracture connection of two different fracture planes, known as NNC type II. (a) This intersection is considered in (b) the computational domain through a non-neighboring connection with an equivalent transmissibility factor ( $T_{f-f'}$ ). ..	53
Figure 4.10: Schematic of a fracture-fracture connection of same fracture plane, known as NNC type III. (a) This connection is considered in (b) the computational domain through a non-neighboring connection with an equivalent transmissibility factor ( $T_{f-f'}$ ). ..	55
Figure 4.11: Illustration of the control-volume dimensions used in the definition of well index for (a) a matrix gridblock containing a well (b) and a fracture segment intersecting a well. The fracture segment bounded inside the gridblock is shown in green. The vertical dimension for the fracture is equal to the aperture.....	57
Figure 4.12: Framework for modeling flow in fractured reservoirs using EDFM approach.....	59
Figure 4.13: Neighboring connections in a conventional computational grid. ....	61
Figure 4.14: A $3\times 3$ grid with a single fracture to illustrate the NNC concept. ....	62
Figure 4.15: The connectivity matrix for a $3\times 3$ grid without fracture consideration.....	62
Figure 4.16: The connectivity matrix in Method I for the $3\times 3$ grid with a single fracture. ....	64
Figure 4.17: The connectivity matrix in Method II for the $3\times 3$ grid with a single fracture. ....	65
Figure 4.18: The $3\times 3$ grid with a single fracture to illustrate the EDFM approach. The fracture is cut into 5 pieces with respect to the intersections with matrix gridblocks.....	67

Figure 4.19: The connectivity matrix in Method III (EDFM) for the $3 \times 3$ grid with a single fracture. The dotted lines show the limits of the connectivity matrix for the non-fractured reservoir model.....	68
Figure 4.20: In EDFM approach (a) a gridblock that is intersected by two fracture planes has a total of (b) eight connections. The red arrows show the non-neighboring connections between the matrix block “ijk” and the fracture segments confined inside the block. ....	70
Figure 4.21: In EDFM approach, all the connections of a fracture cell are treated as non-neighboring connections. In this example, (a) a gridblock is intersected by two different fracture planes $f$ and $f'$ . (b) Hence, the blue fracture cell is connected to one matrix gridblock, one fracture cell from other plane (green plane), and three neighboring cells of the same fracture plane. .....	71
Figure 5.1: A reservoir model with 3 vertical fractures: (a) Map view of the reservoir and the location of fractures. (b) The $20 \times 20$ grid used in the EDFM approach. The reservoir thickness has magnified 20 times for a better illustration. ....	78
Figure 5.2: (a) Oil and (b) water production rates for UTCOMP-EDFM and the fine-grid models. Four cases with different gridblock sizes are considered for EDFM. The $50 \times 50$ case is the optimum one. ....	80
Figure 5.3: (a) Oil and (b) water production rates for UTGEL-EDFM and the fine-grid models. Four cases with different gridblock sizes are considered for EDFM. The $50 \times 50$ case is the optimum one. ....	81

Figure 5.4: Water saturation profiles for the reservoir model after (a) 96 days (left column) and (b) 168 days (right column). The rows from top to bottom show the water saturation profiles for the fine-grid, UTCOMP-EDFM, and UTGEL-EDFM, respectively.....	82
Figure 5.5: A reservoir model with 14 vertical fractures with various orientations (from Moinfar (2013)). (a) Map view of the reservoir and the location of fractures (b) The $20 \times 20$ grid used in the EDFM approach .....	84
Figure 5.6: Comparison of oil production rates obtained from UTGEL-EDFM and UTCOMP-EDFM with Moinfar (2013) results for a 2D reservoir model with 14 fractures with various orientations.....	86
Figure 5.7: Water saturation profiles for the model reservoir after (a) 150 days (left column) and (b) 250 days (right column). The rows from top to bottom show the water saturation profiles for Moinfar (2013), UTCOMP-EDFM, and UTGEL-EDFM, respectively.....	87
Figure 5.8: A 3D reservoir model with 13 inclined fractures (from Moinfar (2013)). (a) Map view of the reservoir and the location of fractures. (b) The $20 \times 20 \times 4$ grid used in the EDFM approach. ....	89
Figure 5.9: Comparison of oil production rates obtained from UTGEL-EDFM and UTCOMP-EDFM with Moinfar (2013) results for a 3D reservoir model with 13 inclined fractures.....	90
Figure 5.10: Water saturation profiles for (a) Moinfar (2013), (b) UTCOMP-EDFM, and (c) UTGEL-EDFM after 80 days. In each column, saturation profiles are shown for the 4 layers, starting from the top layer at the top to the bottom layer at the bottom. ....	91

Figure 5.11: Schematic of fracture network discretization used in the semi-analytic solution of unsteady state gas flow in unconventional reservoirs, developed by Zhou <i>et al.</i> (2014).....	93
Figure 5.12: A reservoir model with 4 hydraulic fractures. The hydraulic fractures (red lines) intersect the horizontal well (black line) at 60 degree.....	94
Figure 5.13: Comparison of gas flow rate obtained from UTCOMP-EDFM with the semi-analytical solution for a 2D reservoir model with 4 hydraulic fractures intersecting well at 60 degree. ....	96
Figure 5.14: Pressure profiles after (a) 350 and (b) 1500 days for the reservoir model in section 5.4. The fractures interference starts almost at 350 days. ....	96
Figure 6.1: A reservoir model with a network of 22 fractures with preferential orientation. The effect of well placement is considered in this example. In the first case, injector-producer line is parallel to the SW-NE direction (blue circles), while for the second case, the line is in the SE-NW direction (red circles). .....	99
Figure 6.2: Oil production rates for the reservoir model with a network of 22 fractures. Results are shown for two different well placements. ....	101
Figure 6.3: Water production rates for the reservoir model with a network of 22 fractures. Results are shown for two different well placements. ....	101
Figure 6.4: Oil recovery for the reservoir model with a network of 22 fractures. Results are shown for two different well placements. ....	102
Figure 6.5: Water saturation profiles for the reservoir model with a network of 22 fractures after 150 days (top row) and 350 days (bottom row). Results are shown for two different well placements, (a) SW-NE and (b) SE-NW.....	103

Figure 6.6: A reservoir model with 2 networks of 39 fractures. The effect of well placement is considered in this example. In the first case, injector-producer line is parallel to the SW-NE direction (blue circles), while for the second case, the line is in the SE-NW direction (red circles). ....	104
Figure 6.7: Oil production rates for the reservoir model with two sets of fracture networks. Results are shown for two different well placements. ....	106
Figure 6.8: Water production rates for the reservoir model with two sets of fracture networks. Results are shown for two different well placements. ....	106
Figure 6.9: Oil recovery for the reservoir model with two sets of fracture networks. Results are shown for two different well placements. ....	107
Figure 6.10: Water saturation profiles for the reservoir model with two fracture networks after 130 days (top row) and 360 days (bottom row). The results are shown for two different well placements, (a) SW-NE and (b) SE-NW.....	108
Figure 6.11: Oil production rates for the reservoir model with one set of fracture network and the SW-NE well placement. Results are shown for two cases with different capillary pressure values as well as one case with no capillary pressure. ....	111
Figure 6.12: Water production rates for the reservoir model with one set of fracture network and the SW-NE well placement. Results are shown for two cases with different capillary pressure values as well as one case with no capillary pressure. ....	111

Figure 6.13: Oil recovery for the reservoir model with one set of fracture network and the SW-NE well placement. Results are shown for two cases with different capillary pressure values as well as one case with no capillary pressure. ....	112
Figure 6.14: Water saturation profiles at 300 days for the reservoir model with one set of fracture network. Profiles are shown for (a) no capillary pressure, (b) $P_c^1$ , and (c) $P_c^2$ cases.....	112
Figure 6.15: Oil production rates for the reservoir model with one set of fracture network and the SE-NW well placement. Results are shown for two cases with different capillary pressure values as well as one case with no capillary pressure. ....	113
Figure 6.16: Water production rates for the reservoir model with one set of fracture network and the SE-NW well placement. Results are shown for two cases with different capillary pressure values as well as one case with no capillary pressure. ....	113
Figure 6.17: Oil recovery for the reservoir model with one set of fracture network and the SE-NW well placement. Results are shown for two cases with different capillary pressure values as well as one case with no capillary pressure. ....	114
Figure 6.18: Oil production rates for the reservoir model with two sets of fracture networks under high capillary pressure effects ( $P_c^2$ ). Results are shown for two different well placements. ....	115
Figure 6.19: Water production rates for the reservoir model with two sets of fracture networks under high capillary pressure effects ( $P_c^2$ ). Results are shown for two different well placements. ....	116

Figure 6.20: Oil recovery for the reservoir model with two sets of fracture networks under high capillary pressure effects ( $P_c^2$ ). Results are shown for two different well placements.....	116
Figure 6.21: Water saturation profiles at 220 days for the reservoir model with two sets of fracture networks for (a) the SW-NE and (b) the SE-NW well placements. The top row shows the results without capillary pressure consideration while the bottom row shows the results with capillary pressure consideration ( $P_c^2$ ).....	117
Figure 6.22: Reservoir models for (a) the simple and (b) complex hydraulic fracture networks. The well, the primary fractures, and the small branched fractures are shown in orange, red, and blue, respectively. ....	120
Figure 6.23: Cumulative gas production for the simple and complex fracture networks. In this case, the rock matrix permeability is 50 nd.....	122
Figure 6.24: Average reservoir pressure versus time for the simple and complex fracture networks. In this case, the rock matrix permeability is 50 nd. ....	123
Figure 6.25: Pressure profiles for (a) the simple and (b) complex fracture networks after 3000 days. In this case, the rock matrix permeability is 50 nd.....	123
Figure 6.26: Cumulative gas production for the simple and complex fracture networks. In this case, the rock matrix permeability is 50 $\mu$ d. ....	124
Figure 6.27: Average reservoir pressure versus time for the simple and complex fracture networks. In this case, the rock matrix permeability is 50 $\mu$ d. ....	124
Figure 6.28: Pressure profiles for (a) the simple and (b) complex fracture networks after 400 days. In this case, the rock matrix permeability is 50 $\mu$ d. ....	125
Figure 6.29: Cumulative gas production for the simple and complex fracture networks. In this case, the rock matrix permeability is 5 md. ....	125

Figure 6.30: Average reservoir pressure versus time for the simple and complex fracture networks. In this case, the rock matrix permeability is 5 md.	126
Figure 6.31: Pressure profiles for (a) the simple and (b) complex fracture networks after 400 days. In this case, the rock matrix permeability is 5 md.	126
Figure 6.32: A reservoir model with a high conductivity channel made with 4 intersecting fracture planes.	133
Figure 6.33: Injection schedules for the waterflood conformance control case study presented in section 6.3.2.	134
Figure 6.34: Oil recovery for PPG injection timing case study. The results are shown for early, intermediate, and late injections of PPG as well as no PPG treatment result.	134
Figure 6.35: Oil production rates for PPG injection timing case study. The results are shown for early, intermediate, and late injections of PPG as well as no PPG treatment result.	135
Figure 6.36: Water production rates for PPG injection timing case study. The results are shown for early, intermediate, and late injections of PPG as well as no PPG treatment result.	135
Figure 6.37: Water saturation profiles after (a) 0.25, and (b) 0.45 PV injection. In part (a), the PPG has only been injected in the “Early” scenario, while in part (b), the “Intermediate” injection has been performed as well.	136
Figure 6.38: A reservoir model with 8 channels for the case study in section 6.3.3. The red channel intersects all the formation as well as the injector well while the blue and green fractures penetrate only one and two layers, respectively.	138

- Figure 6.39: Oil recovery for the case study of section 6.3.3. The results are shown for 1000 and 4000 ppm as well as the waterflood with “No PPG”. .....140
- Figure 6.40: Water production rates for the case study of section 6.3.3. The results are shown for 1000 and 4000 ppm as well as the waterflood with “No PPG”. 140
- Figure 6.41: Oil production rates for the case study of section 6.3.3. The results are shown for 1000 and 4000 ppm as well as the waterflood with “No PPG”. 141
- Figure 6.42: Water saturation profiles after 0.2 PV total injection for (a) waterflood with “No PPG”, (b) waterflood with injection of 1000 ppm gel, and (c) waterflood with injection of 4000 ppm gel. In each column, saturation profiles are shown for the 3 layers, starting from the top layer at the top to the bottom layer at the bottom. .....142

## **Chapter 1: Introduction**

Modeling and simulation of fluid flow in both natural and induced fracture systems has improved progressively over the past sixty years. The huge potential hydrocarbon reserve and the significance of fractures in the recovery process have pushed the research forward on this topic since then. Based on a market analysis by Schlumberger in 2007<sup>1</sup>, almost sixty percent of total oil and forty percent of total gas reserves reside in fractured carbonate reservoirs. Such reserves have made the naturally fractured reservoirs to one of the primary targets for further development and investment. Several recovery mechanisms have been studied thoroughly in petroleum industry to enhance oil and gas productions out of such reservoirs. However, one intrinsic characteristic, i.e. the existence of natural fractures and the corresponding networks, has triggered several challenges and problems associated with the modeling and simulation of the recovery processes in fractured reservoirs. The effectiveness of a recovery mechanism in a real field study is strongly tied to the characteristics of the fracture networks. Fracture domain exhibits a huge contrast in properties compared to the background rock matrix. Low porosity-high permeability fractures are coupled to high porosity-low permeability matrix rock. Although the hydrocarbon initially resides in rock matrix pore volume, the fluid flow is governed mostly by fractures. In reservoir simulation, although natural fractures are accounted as subscale phenomena compared to typical computational cells, their contribution to fluid transport is significant. Hence, to better understand the underlying principles of fluid flow in naturally fractured reservoirs, a multi-scale multi-variable outlook is required.

---

<sup>1</sup> “Carbonate Reservoirs: Meeting unique challenges to maximize recovery”, Schlumberger, 2007

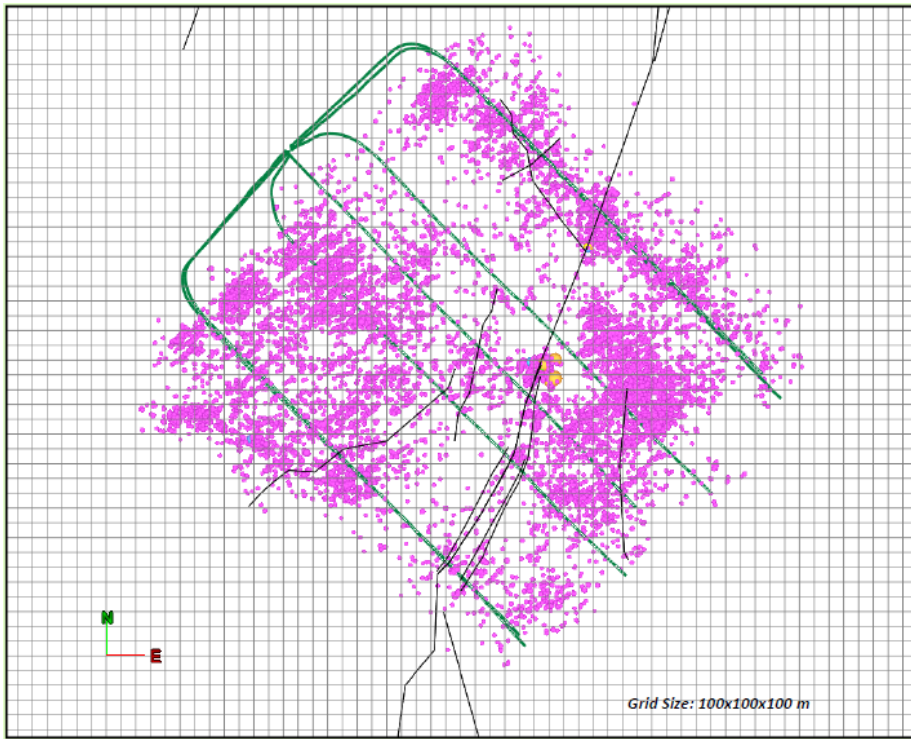


Figure 1.1: Microseismic monitoring of a hydraulic fracturing job (Rahimi Zeynal *et al.* 2014). The green lines are the horizontal wells and the pink dots are microseismic events. Each event represents a rock failure. The fracture network is constructed based on the microseismic map.

Besides natural fractures, induced fracturing has received a great deal of attention over the past few decades. This technology has transformed the previously untapped shale and tight formations to one of the most reliable sources of energy and to the fastest growing area in the petroleum industry. Based on this technology, to increase the productivity of wells drilled in low permeability reservoirs, the near wellbore region is stimulated using high pressure fluid injection, creating systems of simple to complex fracture networks. In such situations, as studied by several researchers, the well performance and the behavior of whole reservoir are substantially affected by the developed fracture networks inside the rock. Although numerous geomechanics research studies are devoted to predict the final shape of fracture networks, the accurate

characterization of such systems still remains a challenge. Figure 1.1 depicts a hydraulic fracturing job monitored by microseismic mapping. Microseismic is a new technology in which the rock failure is recorded by the emitted signals and the data is used to estimate the shape and the extent of fracture networks. As observed in Figure 1.1, the stimulation job has created a complex fracture network in which the intensity and the connectivity of the fractures vary significantly. For such cases, in addition to properties of single fractures, the connectivity of the network is a major parameter as well. Thus, to measure the effectiveness of such a stimulation job, a comprehensive modeling tool is required to capture the complexity of the fracture networks.

Although several models have found limited applications to study flow in fracture systems in the petroleum industry, still there is a need for new models to be applied for more practical purposes. One of the first proposed classes of models is based on the Dual Porosity and Dual Permeability (DPDP) concept. In this class of models, to represent the effect of small-scale densely distributed fractures, an equivalent structured domain is coupled to the rock matrix grid and a new set of properties is assigned to that. The main advantage of the dual continuum approach is the simplicity of the model. Instead of dealing with highly heterogeneous fracture systems, two coupled domains are considered, matrix and fracture domains. However, depending on the type of problem, the accuracy of this approach is questionable. Since an upscaling approach is taken into account by the dual continuum models, an accurate characterization of individual fractures becomes impossible. Thus, for sparse distributions of channels or fractures, these models lose applicability and fail to represent the effect of individual fractures appropriately. To look into more details and capture the behavior of fractures accurately, Discrete Fracture Models (DFMs) were developed. In this class of models, unstructured gridding is performed to construct fracture networks with different shapes and configurations, thus

providing a powerful tool to study a broad range of problems. Each fracture in the DFM approach is a 2D interface and is generated by polyhedral cells of matrix gridblocks. Although more realistic compared to the dual continuum models, the DFMs are still computationally expensive for field-scale simulations. To perfectly reveal the geometry and the configuration of fractures, the size of unstructured cells decreases as the latter locate closer to fractures. In addition, since the majority of commercial reservoir simulators work with structured grids, the implementation of DFMs in such simulators is challenging.

Over the past few years, several methods have been proposed to incorporate the advantages of the dual continuum and the discrete fracture models. The objective has been first to employ the DFMs in characterization and analysis of fracture networks and then to apply the outcome in the form of input for further modeling and simulation using the dual continuum approaches. In fact, the DFMs are used for modeling the fractures interactions, while the rock matrix domain remains in the structured format. A recently developed model of this kind is the Embedded Discrete Fracture Model (EDFM) developed by Li and Lee (2008) and Moinfar *et al.* (2012, 2014). In EDFM, each fracture is embedded inside the matrix grid and is discretized by the cell boundaries. The connection between matrix and fracture cells is defined based on the geometry of fractures. The rock matrix composed of structured cubical cells, similar to dual continuum approach, while the fracture is discretized into unstructured polygons.

As part of this research, UTCOMP and UTGEL, The University of Texas in-house reservoir simulators, were augmented with the capability of modeling and simulation of fluid flow in complex fracture systems to investigate several recovery mechanisms in fractured reservoirs and to study the efficiency of hydraulic fracturing in unconventional resources. To do so, the EDFM approach was implemented in these

reservoir simulators using a non-neighboring connection approach. Since EDFM is compatible with the structured grid, the implementation of the model and the required modifications were straightforward. To handle the connections between matrix and fracture cells, extra directions were defined for the corresponding control-volumes. Consequently, the mass balance and pressure equations were modified to account for matrix-fracture and fracture-fracture fluid transfers.

In Chapter 2, some of the proposed models in the literature for studying fractured reservoirs are reviewed and the recent improvements in this field are discussed. A brief description of the UTCOMP and UTGEL reservoir simulators is then presented in Chapter 3 where the governing equations are reviewed. Next in Chapter 4, the EDFM approach description and the methodology for implementing this model into the reservoir simulators are described. In Chapter 5, UTCOMP-EDFM and UTGEL-EDFM are compared against a fine-grid and more complex simulation problems as well as one semi-analytical solution to verify the implementation work. To show some of the applications of UTCOMP-EDFM and UTGEL-EDFM to study fractured reservoirs, several simulation case studies are conducted in Chapter 6. Finally, in Chapter 7, summary and conclusions of this research study are presented and a few recommendations for future works are offered.

## **Chapter 2: Literature Review**

Numerical modeling and simulation of flow in fractured reservoirs has a long history in the petroleum industry. For more than 50 years, researchers have been studying the behavior of fractured reservoirs to capture the physics of fluid flow in such systems. Due to significant contribution of fractured reservoirs in daily production of hydrocarbon, the research in this field has moved progressively toward more practical approaches. The erstwhile models have been further modified and extended in order to predict the performance of these reservoirs more accurately. In general, a fracture is defined as a discontinuity in the formation rock originated from loss of cohesion between matrix grains (Van Golf-Racht (1982)). Such discontinuities alter the flow characteristics of the host rock and turn the formation rock into a complex system to be analyzed. In terms of geologic life, almost every formation has withstood severe stresses and has undergone tectonic movements, while the rock material itself was not solid enough (Saidi (1987)). Hence, it is not unusual to think that almost all reservoirs are somehow fractured regardless of whether or not the fractures are active and effective on fluid flow (Aguilera (1995)). To better understand the effect of fractures, several approaches have been proposed, most of which are grounded on the basis of two classes of models, the dual porosity (or dual continuum) and the discrete fracture models. Each class of models has developed to answer some of the challenges associated with modeling and simulation of fractured reservoirs. However, due to high degree of complexity of such systems, still more improvements are required in the available models in order to study the behavior of fractured reservoirs more accurately. In this chapter, a literature review of dual continuum and discrete fracture models is presented. The recently developed Embedded

Discrete Fracture Model (EDFM) is then introduced in Chapter 4, which is the main focus of this research.

## 2.1 DUAL POROSITY MODELS

In the dual porosity approach, a naturally fractured reservoir model is represented by two collocated domains, the fracture domain and the matrix domain. Thus, in every spatial point, two sets of parameters are defined, one for matrix and one for fracture, and the corresponding fluid flow equations are coupled by a term called the Transfer Function. Usually the matrix domain represents the hydrocarbon storage and is regarded as discrete blocks surrounded by the interconnected fracture system. On the other hand, the fracture domain is considered as the conductive path with small, if not zero, storage capacity. Since the fractures are fed by the matrix blocks, the latter are handled as source or sink terms for the fracture elements. The original assumptions in the model development are homogenous and isotropic matrix gridblocks, uniform fracture networks aligned with major coordinates, and semi-steady state flow in matrix gridblocks. These idealizations are suitable for a dense fractured reservoir with highly interconnected networks. Figure 2.1 illustrates the well-known schematic of the dual porosity concept. The matrix domain is usually composed of regularly-shaped blocks such as slabs, cubes, or parallelepipeds. If a communication is defined between matrix gridblocks as well, then the model is called Dual Porosity-Dual Permeability (DPDP) or simply Dual Continuum model.

Barrenblatt *et al.* (1960), for the first time, introduced the mathematical concept of dual porosity model for studying fluid flow in fissured rocks. They considered two overlapped medium with different properties in which coupled mass conservation

equations were solved analytically. Later, Warren and Root (1963) proposed a similar mathematical model to describe the behavior of a naturally fractured reservoir. In their model, they considered two collocated domains, one as the main storage for the fluid (primary porosity) and the other as the pathway for the fluid flow in porous medium (secondary porosity), while the two domains are coupled with a transfer function. Accordingly, two parameters were defined that govern the behavior of this idealized model:  $\omega$  as the storage capacity of the fracture system and  $\lambda$  as the measure of flow capacity of the matrix domain. Next, they utilized these two parameters to analyze the pressure transient of fractured reservoirs. Odeh (1965), however, showed mathematically that under the same type of assumptions, similar to Warren and Root's model, field measured pressure build-up and drawdown data of fractured reservoirs look similar to those of a homogenous reservoir in some specific cases, and it is difficult to distinguish between them.

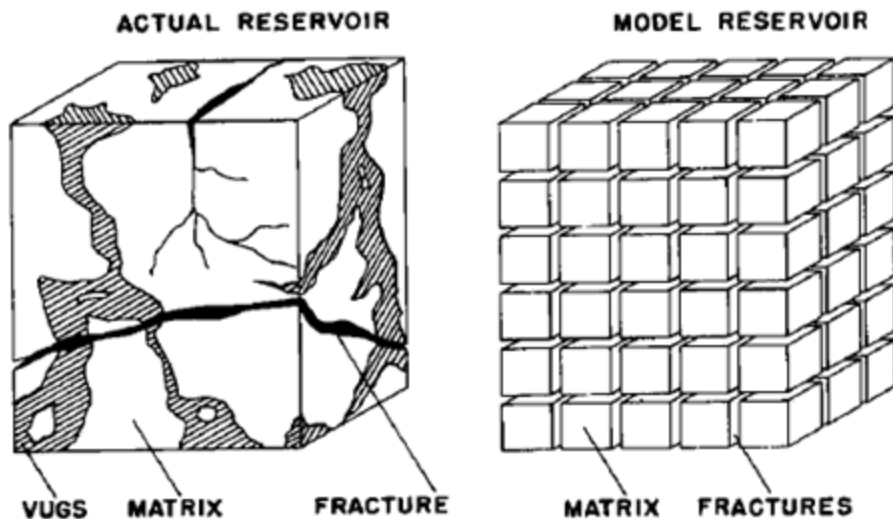


Figure 2.1: Idealization made by dual porosity model for a naturally fractured reservoir (Warren and Root (1963)).

Later, Kazemi (1969) used a cylindrical reservoir with horizontal fractures to verify the Warren and Root's model in the case that unsteady state regime is considered for single-phase flow in the matrix as well. He showed that their model is valid for the cases where the contrast between matrix and fracture flow characteristics is high.

Kazemi *et al.* (1976) developed a three-dimensional numerical reservoir simulator to study two-phase water-oil displacement in fractured reservoirs. They used the same concept of Warren and Root's model for the two-phase flow. They studied water imbibition in fractured reservoirs and investigated its effect on reservoir performance. The formulations they used for fracture and matrix domains are given in Eqs. (2.1) and (2.2), respectively, where  $\lambda$  is relative mobility,  $P$  is pressure,  $\rho$  is density,  $Z$  is depth,  $T$  is matrix/fracture transmissibility coefficient,  $q$  is rate,  $\phi$  is porosity,  $S$  is saturation, and  $B$  is formation volume factor. Also, the subscripts  $j$ ,  $m$ , and  $f$  denote phase, matrix domain, and fracture domain, respectively.

$$\nabla \cdot \left[ \lambda_{j-f} \left( \nabla P_{j-f} - \rho_j g \nabla Z \right) \right] + \left[ T_{j-m} \left( P_{j-m} - P_{j-f} \right) \right] + q_j = \frac{\partial}{\partial t} \left( \frac{\phi_f S_{j-f}}{B_{j-f}} \right). \quad (2.1)$$

$$-T_{j-m} \left( P_{j-m} - P_{j-f} \right) = \frac{\partial}{\partial t} \left( \frac{\phi_m S_{j-m}}{B_{j-m}} \right). \quad (2.2)$$

The left hand side of Eq. (2.2) is the Transfer Function ( $\tau_{m-f}$ ) which accounts for matrix/fracture communication. To calculate relative mobility and matrix/fracture transmissibility, they used

$$\lambda_{j-f} = \left( \frac{kk_{rj}}{\mu_j B_j} \right)_f , \quad (2.3)$$

and

$$T_{j-m} = V_b \sigma \left( \frac{kk_{rj}}{\mu_j B_j} \right)_m , \quad (2.4)$$

where  $k_r$  is relative permeability,  $\mu$  is viscosity, and  $V_b$  is matrix block bulk volume. In equation (2.4),  $\sigma$  is the shape factor which represents the geometry of matrix gridblocks and controls the fluid exchange between matrix and fracture. To calculate shape factor, they used the following equation, where  $L_x$ ,  $L_y$ , and  $L_z$  are matrix block dimensions. However, Coats (1989) illustrated that including transient flow will result in a shape factor twice as large as the one used by Kazemi *et al.* (1976).

$$\sigma = 4 \left( \frac{1}{L_x^2} + \frac{1}{L_y^2} + \frac{1}{L_z^2} \right). \quad (2.5)$$

Compared to Warren and Root's model, in addition to studying two-phase flow, Kazemi *et al.*'s simulator was capable of modeling some degree of heterogeneity by considering various properties for individual matrix and fracture blocks. However, although gravity effect was considered in the 3D domain, its effect was neglected in the transfer function definition. Also, the pressure and saturation gradients in matrix block were neglected.

As another two-phase reservoir simulator, Rossen (1977) developed a single porosity simulator to study naturally fractured reservoirs. To handle the matrix/fracture communication, he considered the fluid exchange as source/sink term in mass balance

equations for fracture domain, and treated them using a semi-implicit scheme to increase the speed and stability of the solution.

Later, Kazemi *et al.* (1979) used the numerical simulator developed in their earlier work to match experimental results. They used water flooding data in fractured cylindrical cores, as well as rectangular blocks, to examine the reliability of their simulator. They used capillary pressure end points as the matching parameters.

De Swaan (1976) developed a mathematical model for unsteady state flow in fractured reservoirs. He showed that the pressure response of a fractured reservoir during well test is modeled by two linear lines corresponding to early and late times. However, this approach does not predict the transition between these two lines. Furthermore, his model contains only the fluid and reservoir properties and no shape factor is required in his model.

If the proposed models of the dual porosity concept are closely inspected, it is evident that they are mostly constructed on the same core, in which two collocated domains with high contrast are coupled by the transfer function. Hence, one approach to boost the accuracy of such models would be modification of the transfer function. Basically, the transfer function describes the fluid exchange between matrix blocks and surrounding fractures. This fluid exchange occurs due to viscous, capillary, and gravitational forces. However, based on Eqs. (2.1) to (2.4), the capillary and gravitational forces were not considered properly in the definition of the transfer function and only viscous forces were included. To resolve this problem, Litvak (1985) added an explicit term to the transfer function calculation as presented in Eq. (2.6). In this equation,  $CG_{m-f}$  is the difference between capillary and gravity forces between matrix block and surrounding fractures and is presented by Eq. (2.7) where  $L_Z$  is the height of the matrix block,  $Z_{j-m}$  is the height to which the matrix block is immersed in phase  $j$ ,  $P_{c-m}$  is oil-

water capillary pressure in matrix block, and  $S_{j-f}$  is the saturation of phase  $j$  in the fracture. The latter is used as the correction for partially fracture immersion ( $L_z$  correction). Also, in their model, they assumed zero capillary pressure in the fracture.

$$\tau_{m-f} = -T_{j-m} (P_{j-m} - P_{j-f}) + CG_{m-f}. \quad (2.6)$$

$$CG_{m-f} = T_{m-f} S_{j-f} [(\rho_w - \rho_o) g (L_z - Z_{j-m}) + P_{c-m}]. \quad (2.7)$$

Later, Sonier *et al.* (1988) computed a dynamic phase height to which the matrix block is immersed using normalized saturations with respect to initial and residual saturations of oil and water. Also, they used a weighting factor to calculate the upstream properties. A comparison between Sonier's and Litvak's results is available in Chen (1993). Also, as an evaluation of Eq. (2.7), a discussion was presented by Aldejain (1999) regarding the fracture saturation term. He expressed that matrix capillary pressure and fluid height in matrix block should not be multiplied by the fracture saturation, and thus he proposed a modified form of capillary and gravity terms.

Another approach to modify the transfer function definition is to apply pseudo relative permeability and pseudo capillary pressure curves. The aim is to reduce the three-dimensional problem to a two-dimensional one by accounting for gravitational effects. Thomas *et al.* (1983) used the following equation to calculate oil-water capillary pressure in matrix including the gravity forces (Coats *et al.* (1971)). Later, some modifications were made to this equation by Dean and Lo (1988) and Rossen and Shen (1989).

$$P_{c-m} = \frac{1 - S_{w-m} - S_{or-m}}{1 - S_{wi-m} - S_{or-m}} (\rho_w - \rho_o) g L_z. \quad (2.8)$$

Although inclusion of the capillary and gravity forces improved the definition of the transfer function, still more modifications were required to capture the transient flow and the pressure and saturation gradients in matrix blocks. Saidi (1983) proposed that subgridding of the matrix block can properly capture the gravity drainage effect. To do so, he discretized the matrix domain into radial and vertical subdomains creating a two-dimensional model. In his model, fracture pressure was determined according to the distance to water-oil contact (WOC). However, due to further discretization of matrix blocks, this approach increased the computational cost significantly.

Pruess and Narasimhan (1985) introduced the concept of Multiple Interacting Continua (MINC) based on the assumption that distribution of thermodynamic properties (including pressure) in a matrix block depends on the distance from the nearest fracture. This allowed a subgridding pattern with nested volume elements to properly represent the isopotential surfaces parallel to fractures. According to this concept, Gilman and Kazemi (1983) and Gilman (1986) proposed two matrix subgridding approaches, called nested blocks and stacked blocks, discretized in horizontal and vertical directions, respectively (Figure 2.2). This approach not only decreased the dimension of the problem, but also improved the calculation of the gravity effects allowing phase segregation in matrix block as well. The MINC method was later applied by Wu and Pruess (1988) to study oil-water imbibition process. They observed that accurate results are obtained using the MINC method in imbibition process, while the conventional transfer function gave rise to a significant error. Similar to other subgridding techniques, due to an increase in the number of matrix blocks, more computational time was required; however, since the dimension of the problem decreased to a two-dimensional one, simpler equations were to be solved.

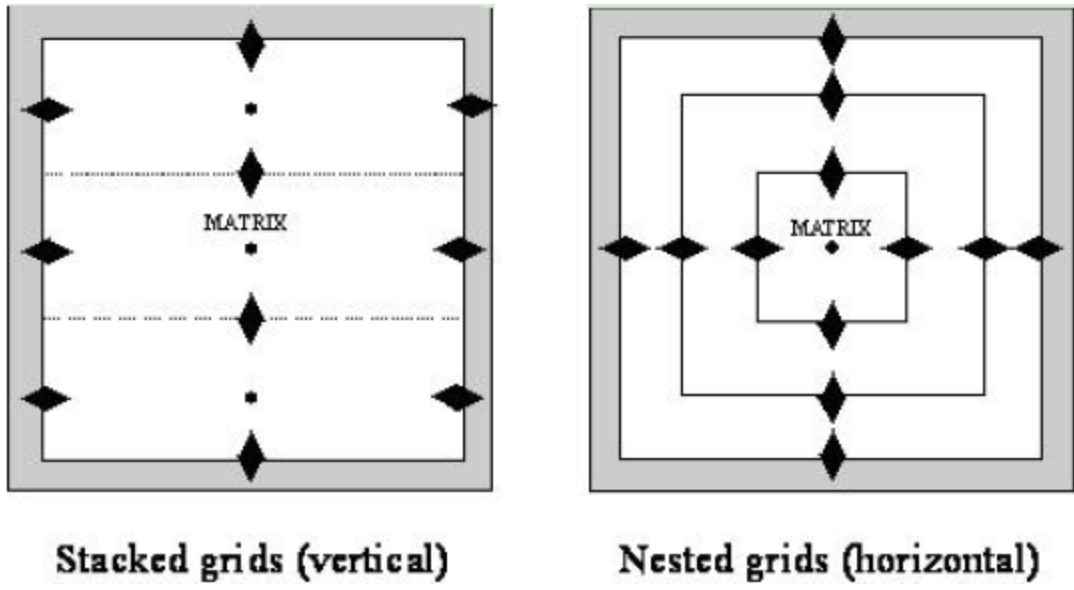


Figure 2.2: Stacked and Nested discretizations used in MINC approach (Gilman (1986)).

As another major improvement in the dual porosity concept, several authors studied the impact of flow in the matrix domain as well as the fracture system, on the overall performance of a naturally fractured reservoir (Hill and Thomas (1985), Dean and Lo (1988)). Since in addition to porosity, permeability is defined for both domains, this type of models is called Dual Porosity-Dual Permeability (DPDP) or Dual Continuum models. Dean and Lo (1988) observed that a much higher oil recovery was obtained when the matrix block communications were considered. This increase was even more significant when vertical permeability in matrix domain was considerable. Since then, several comprehensive reservoir simulators have developed based on the dual porosity-dual permeability approach to study several scenarios in naturally fractured reservoirs (Chen (1993), Aldejain (1999), Naimi-Tajdar *et al.* (2007), and Tarahhom (2008)). Although, this modification enabled more accurate simulation of such reservoirs, more effort was required for the computational time.

## 2.2 DISCRETE FRACTURE MODELS

Although dual porosity models substitute a highly complex fracture network with a simple structured continuum, they fail to provide accurate results when the behavior of individual fractures is of more interest. In a number of fractured reservoirs, the fractures do not establish a connected network and thus the continuum assumption is no longer valid. Also, when fractures length is comparable to the size of the computational grid, upscaling and averaging of the fractures properties alter the realistic representation of the network (Long *et al.* (1982), Long and Witherspoon (1985)). To further eliminate such obstacles in studying fractured reservoirs, a new class of models, called the Discrete Fracture Model (DFM), was proposed. In DFMs, each fracture is modeled explicitly through the application of unstructured gridding. Unstructured cells are utilized in order to conform to the exact geometry and location of each fracture. The cells could be 3D polyhedral cells, 2D interfaces, or 1D lines. This technique provides the capability to consider different fracture geometries. The specification of fractures attributes is made either deterministically, by outcrop characterization studies or microseismic monitoring, or stochastically. To solve the fluid flow equations for such systems, mostly finite-element or finite-volume (control-volume finite-difference) based approaches are used. Moreover, since fracture geometry is honored through unstructured gridding, there is no need for the transfer function to compute the fluid exchange between matrix and fracture cells. However, the main drawback of the DFMs is the computational cost. Due to refined unstructured cells adjacent to fractures, the numerical solution of such systems is computationally expensive. Moreover, the implementation of these models into structured grid conventional reservoir simulators is another challenge. In the following sections, a brief literature review of both finite-element- and finite-volume-based discrete fracture models is presented.

In an attempt to solve a two-dimensional transient solute transport in a fractured porous medium, Noorishad and Mehran (1982) used a finite-element method (FEM) to consider fractures as discrete elements. They used two-nodal point elements to represent fractures in the model. Later, Baca *et al.* (1984) used FEM and the superposition concept to study flow and transport in a fractured medium for a two-dimensional problem.

Therrien and Sudicky (1996) used a control-volume finite-element (CVFE) approach to study variably-saturated flow and solute transport in a three-dimensional model. They included advection, dispersion, molecular diffusion and sorption in their model. CVFE is similar to FEM in terms of interpolation functions for dependent variables, while it applies a different technique for flux calculations. In CVFE, fluid flux between nodes is calculated explicitly and then mass balance equation is solved, while in finite-element approach, fluid potentials are computed initially (Fu *et al.* (2005)).

Kim and Deo (2000) employed FEM with standard Galerkin method to solve two-phase flow in a 2D fractured porous medium. The formulation was fully implicit and was solved using the inexact Newton method. They discretized the domain into a set of triangular elements of matrix and line elements of fractures. Using their model, they studied the effect of matrix absolute permeability, injection rate, and capillary pressure on oil recovery. For 3D problems, Juanes *et al.* (2002) proposed a modified finite-element approach to study groundwater flow. Later, Karimi-Fard and Firoozabadi (2003) proposed a similar model to Kim and Deo's, but using IMPES scheme where pressure equation is solved implicitly while saturation equation is solved explicitly. They used 1D entities for fractures and 2D triangles for the matrix domain. Figure 2.3 depicts a schematic of their discretization method and a case study with six fractures. They performed a few simulation case studies for water-wet and mixed-wet media and concluded that the FEM is more robust compared to finite-difference approach for

studying complex fracture configurations.

Hoteit and Firoozabadi (2005) combined the mixed finite-element and the discontinuous Galerkin (DG) methods to solve non-linear flow equations and to approximate more accurately interface fluxes in a single-phase fractured media. One problem with models developed based on the classical finite-element approach is the local mass conservation in highly heterogeneous reservoirs. This issue is observed in the case of multiphase flow examples. Although a mixed finite element method can solve this problem, it is computationally expensive to use such formulations.

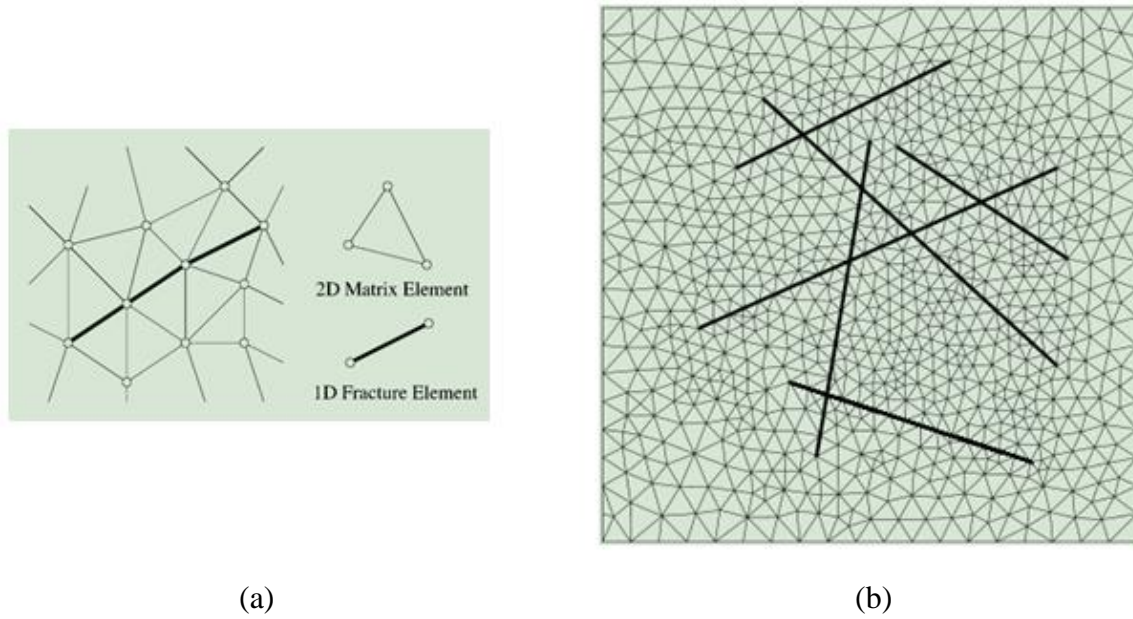


Figure 2.3: (a) Schematic of a discretization used by finite-element method and (b) a case study with 6 fractures (Karimi-Fard and Firoozabadi (2003)).

Karimi-Fard *et al.* (2004) used a control-volume finite-difference approach with a two-point flux approximation to develop a DFM suitable for conventional reservoir simulators working by a grid connectivity list. They used lower-dimensional objects to represent fractures such as segments and polygons in 2D and 3D problems, respectively.

Although this technique eliminates fractures in the grid domain, the thickness of fractures is considered in the computational domain for flow-rate calculation. To solve flow equations, they considered a node at the center of each element (Figure 2.4) and applied a finite-difference scheme.

Monteagudo and Firoozabadi (2004) developed a two-phase fractured reservoir simulator based on the control-volume (CV) approach. The CV approach (Baliga and Patankar (1980)) is a finite volume formulation over dual cells of a Delaunay mesh and is locally conservative. Also, it performs upstream winding based on flow potentials at control-volume boundaries. Monteagudo and Firoozabadi (2004) used their model to study capillary and gravity effects on simulation of two-phase immiscible and incompressible flow in a 3D problem. Later, Paluszny et al. (2007) employed a hybrid finite-element finite-volume discretization to solve flow equations in complex geometry domains.

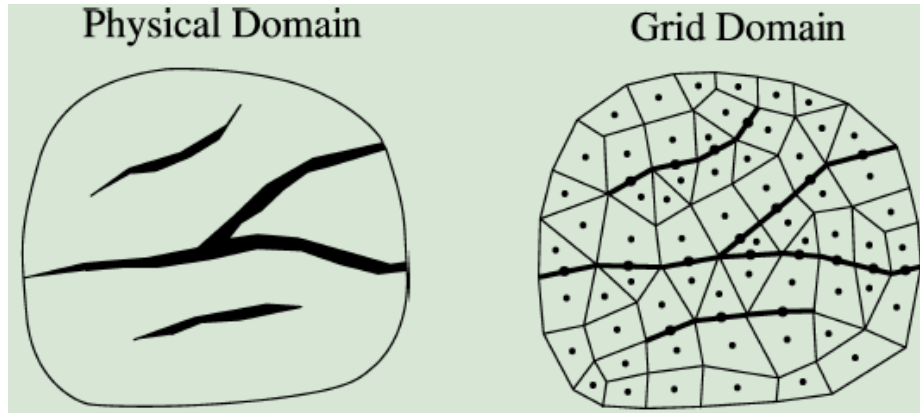


Figure 2.4: A discretization example used in modeling a fractured porous medium with control-volume finite-difference formulation (Karimi *et al.* (2004)). To apply finite-difference scheme, a node is considered at the center of each element.

According to all the discrete fracture models discussed above, an unstructured gridding is required to conform to geometry of fractures. As the complexity of the fracture network increases, a more detailed discretization is required to capture the exact shape of fractures. This problem not only complicates the development of gridding algorithms, but also hinders their implementation in conventional reservoir simulators. To eliminate gridding problems associated with DFMs, Lee *et al.* (2000, 2001) and Li and Lee (2008) introduced a novel model, the Embedded Discrete Fracture Model (EDFM). Using EDFM, they explicitly modeled fracture planes without discretization of the matrix domain into unstructured elements. In their model, fracture planes intersect the matrix grid and thus are discretized by matrix cell boundaries. In fact, fracture planes are surrounded by matrix gridblocks and their boundaries do not coincide. Since EDFM is the main focus of this research, a detailed description of this model along with the implementation scheme is presented in Chapter 4.

## **Chapter 3: Overview of UTCOMP and UTGEL Reservoir Simulators**

For modeling and simulation of flow in the complex fractured reservoirs, the formulation of UTCOMP and UTGEL, the in-house reservoir simulators, has been extended to enhance their capabilities in modeling such reservoirs. To do so, the Embedded Discrete Fracture Modeling approach (EDFM) has been implemented using the non-neighboring connection concept. In this chapter, in view of introducing the structure and features of UTCOMP and UTGEL reservoir simulators, a brief overview of formulations and solution schemes is presented. Later, in Chapter 4, a detailed methodology of EDFM and the corresponding modifications are discussed.

### **3.1 UTCOMP RESERVOIR SIMULATOR**

The University of Texas compositional reservoir simulator (UTCOMP) was first developed by Chang (1990) to model miscible gas flooding. However, after more than two decades of development, it has transformed into a more comprehensive reservoir simulator capable of modeling a variety of three-dimensional equation of state (EOS) compositional simulation problems with up to four phases (aqueous phase, oil phase, gas phase, and second non-aqueous liquid phase). There are several features available in UTCOMP that allow simulation of more complex problems, such as polymer flooding, surfactant flooding, asphaltene precipitation, CO<sub>2</sub> sequestration, miscible and immiscible gas flooding, gas-foam flooding, and several non-isothermal processes.

UTCOMP is an IMPEC-type reservoir simulator in which the pressure equation is solved implicitly followed by an explicit solution of concentrations and saturations. To more accurately model reservoir simulation problems, several numerical features have

been added over the past few years including higher-order finite-difference methods and robust numerical solvers.

In the next section, the mathematical and governing equations of the UTCOMP reservoir simulator are presented and the procedures for deriving such equations are expressed. Although these equations cover the general mathematical structure of the simulator, the discussions of a few principal concepts, such pertaining to phase equilibrium calculations, relative permeability models etc., are not presented in this chapter. For detailed formulation and description of these features, one is referred to Chang (1990) and to UTCOMP Technical Documentation 3.8 (2011).

### 3.1.1 Governing Formulations

In this section, the principal mathematical formulations of UTCOMP are expressed; these are mass conservation and auxiliary equations, pressure equation, and initial and boundary conditions. For certain equations, the basic assumptions and the calculations for deriving the equations are presented.

#### 3.1.1.1 Mass Conservation and Auxiliary Equations

To derive the conservation of mass statement, we start from the strong form of the conservation equation for component  $i$  in a multiphase flow (Eq. (3.1)), which applies to every point of the system of interest.

$$\frac{\partial W_i}{\partial t} + \vec{\nabla} \cdot \vec{F}_i - R_i = 0 \quad \text{for } i=1\dots N_c, \quad (3.1)$$

where  $W_i$ ,  $\vec{F}_i$ ,  $R_i$ ,  $N_c$  are total concentration of component  $i$ , flux of component  $i$ , source terms, and number of components, respectively (Lake *et al.* 1984). The unit of this equation is mole per unit bulk volume per unit time. For further development of Eq. (3.1), the following auxiliary equations are employed (Eqs. (3.2) through (3.6)). Eq. (3.2) leads to the definition of the accumulation term which includes the adsorption on solid surface as well. However, the adsorption term is neglected in the version used in this work. The flux definition in Eq. (3.3) is comprised of two terms, convection and dispersion. Eqs. (3.4) and (3.5) are Darcy's law for multiphase flow and the relative mobility definition, respectively. It is noteworthy to point out that all of these auxiliary relations have an empirical basis.

$$W_i = \phi \sum_{j=1}^{N_p} \xi_j S_j x_{ij} + (1-\phi) \underbrace{\xi_s x_{is}}_{\text{Adsorption}} \quad \text{for } i=1 \dots N_c + 1, \quad (3.2)$$

$$\vec{F}_i = \sum_{j=1}^{N_p} \left( \underbrace{\xi_j x_{ij} \vec{u}_j}_{\text{Convection}} - \phi S_j \xi_j \vec{K}_{ij} \cdot \vec{\nabla} x_{ij} \right) \quad \text{for } i=1 \dots N_c + 1, \quad (3.3)$$

$$\vec{u}_j = -\vec{k} \lambda_{rj} (\nabla P_j - \gamma_j \nabla D) \quad \text{for } j=1 \dots N_p, \quad (3.4)$$

$$\lambda_{rj} = \frac{k_{rj}}{\mu_j} \quad \text{for } j=1 \dots N_p, \quad (3.5)$$

$$R_i = \frac{q_i}{V_b} \quad \text{for } i=1 \dots N_c + 1, \quad (3.6)$$

where

$\phi$  = Porosity

$N_p$  = Number of phases

$\xi_j$  = Molar density of phase  $j$

$\xi_s$  = Molar density of solid phase

$S_j$  = Saturation of phase  $j$

$x_{ij}$  = Mole fraction of component  $i$  in phase  $j$

$x_{is}$  = Mole fraction of component  $i$  adsorbed on solid

$\vec{u}_j$  = Velocity of phase  $j$

$\vec{\vec{K}}_{ij}$  = Components of dispersion tensor

$\vec{k}$  = Absolute permeability diagonal tensor

$\lambda_{rj}$  = Relative mobility of phase  $j$

$P_j$  = Pressure of phase  $j$

$\gamma_j$  = Specific gravity of phase  $j$

$D$  = Depth

$k_{rj}$  = Relative permeability of phase  $j$

$\mu_j$  = Viscosity of phase  $j$

$q_i$  = Molar flow rate of component  $i$

$V_b$  = Bulk volume of gridblock

In the above equations, phase indices are 1-Aqueous phase, 2-Oilic phase, 3-Gaseous phase, and 4-Second non-aqueous liquid phase. In terms of component numbering, numbers from 1 to  $N_c$  are for hydrocarbon components, while  $N_c+1$  accounts for water component. Also, we assume complete immiscibility between water and other hydrocarbon phases.

If we substitute Eqs. (3.2) through (3.6) into Eq. (3.1), we obtain the mass conservation equation for each component. Thus, we have

$$\frac{\partial \left( \phi \sum_{j=1}^{n_p} \zeta_j S_j x_{ij} \right)}{\partial t} - \vec{\nabla} \cdot \left[ \sum_{j=1}^{n_p} \zeta_j \lambda_j x_{ij} (\nabla P_j - \gamma_j \nabla D) + \phi \zeta_j S_j \vec{K}_{ij} \nabla x_{ij} \right] - \frac{q_i}{V_b} = 0 \quad (3.7)$$

*for  $i = 1, 2, \dots, N_c$ .*

These non-linear partial differential equations are solved along with other additional equations. For more detail about the discretization of these equations and the solution procedure, one is referred to Chang (1990) and UTCOMP Technical Documentation 3.8 (2011).

### **3.1.1.2 Pressure Equation**

The pressure equation is derived based on a total mass balance statement on all of the existing phases in the system. To do so, at every time step, the summation of volumes occupied by all of the phases is set to be equal to the total pore volume (Chang (1990)). This statement is shown by Eq. (3.8) where  $V_t$  is the total fluid volume,  $V_p$  is the pore volume as a function of pressure, and  $\vec{N}$  is the vector of the total number of moles for every component  $N_i$ .

$$V_t(P, \vec{N}) = V_p(P). \quad (3.8)$$

If we differentiate both sides of the above equation with respect to time and follow with the chain rule, we obtain

$$\left( \frac{\partial V_t}{\partial P} \right)_{\vec{N}} \left( \frac{\partial P}{\partial t} \right) + \sum_{i=1}^{n_c+1} \left( \frac{\partial V_t}{\partial N_i} \right)_{P, N_{k(k \neq i)}} \left( \frac{\partial N_i}{\partial t} \right) = \left( \frac{dV_p}{dt} \right) \left( \frac{\partial P}{\partial t} \right). \quad (3.9)$$

If we assume a slightly compressible formation (linear change in porosity with respect to pressure) and use Eq. (3.2) to calculate total number of moles for each component, we can substitute all the resultant information back into Eq. (3.9) and come up with the final form of the pressure equation as

$$\begin{aligned} & \left( V_p^0 c_f - \frac{\partial V_t}{\partial P} \right) \left( \frac{\partial P}{\partial t} \right) - V_b \sum_{i=1}^{n_c+1} \vec{V}_{ti} \vec{\nabla} \cdot \sum_{j=1}^{n_p} \vec{k} \lambda_{rj} \xi_j x_{ij} \nabla P \\ &= V_b \sum_{i=1}^{n_c+1} \vec{V}_{ti} \vec{\nabla} \cdot \sum_{j=1}^{n_p} \vec{k} \lambda_{rj} \xi_j x_{ij} (\nabla P_{c2j} - \gamma_j \nabla D) \\ &+ V_b \sum_{i=1}^{n_c+1} \vec{V}_{ti} \vec{\nabla} \cdot \sum_{j=1}^{n_p} \phi \xi_j x_{ij} S_j \vec{k} \nabla x_{ij} + \sum_{i=1}^{n_c+1} \vec{V}_{ti} q_i, \end{aligned} \quad (3.10)$$

where

$V_p^0$  = Pore volume at reference pressure

$c_f$  = Formation compressibility

$\vec{V}_{ti}$  = Partial molar volume of component  $i$

$P_{c2j}$  = Capillary pressure between phase 2 and phase  $j$

The other parameters are the same as the ones introduced for Eq. (3.7).

To solve the pressure and mass balance equations, an IMPEC-type formulation is employed. At every time step, after the calculation of basic parameters, a system of linear matrix equations is formed where the pressure for all of the gridblocks is solved simultaneously and implicitly. To do that, several robust numerical solvers have been

added to the reservoir simulator capable of solving numerous types of linear system of equations. Later, in the next chapter, it is shown that the implementation of the Embedded Discrete Fracture Model (EDFM) would alter the structure of the linear equations. After solving the system, the updated pressures are used to calculate concentrations and saturations of all of the components and phases. Since the pressure in the next time step is known, it is called an explicit solution of concentration. Finally, all of the updated values are used in the next loop to perform the calculations for the next time step.

### 3.1.2 Initial and Boundary Conditions

To solve the pressure and mass balance equations for the set of non-linear partial differential equations, we need initial and boundary conditions. The initialization process is defined as either introducing the unknowns directly at the very first time step, or computing them from other relations indirectly. Gridblock pressures, phase saturations, and phase molar compositions of components are deemed as unknown parameters that are required for simulation initialization. If the total moles of hydrocarbon components are input to the simulation, phase behavior calculation is needed to solve for initial concentrations and hydrocarbon phases saturations. Also, the initial saturation of water is given by the user. Likewise, in terms of static equilibrium, there are two ways to determine pressures at every gridblock. The simplest one is to directly input initial pressures; however, if the proposed initial condition does not satisfy the static equilibrium condition, after one or two time steps the simulator itself modifies the pressure distribution. The second approach is to determine a datum and the corresponding

initial pressure; therefore, the pressures for other gridblocks are determined based on the static pressure head considering the depth of each gridblock.

In UTCOMP, the boundary conditions are divided into three classes: no-flow, inflow, and outflow boundaries (Chang (1990)). The no-flow boundary condition is simply expressed as zero velocity across the impermeable boxed-shaped reservoir limits. This condition is satisfied by setting transmissibility factors to zero at the specified direction for boundary gridblocks. More detail about the formulation of transmissibility factors is given in the next chapter. On the other hand, to implement inflow and outflow boundary conditions, well models are necessary. Well models define the relation between well rates, bottomhole pressure, and well cell pressure as presented in Eq. (3.11), where  $Q_j$  is the flow rate for phase  $j$ ,  $PI_j$  is the phase productivity index,  $P_{wf}$  is flowing bottomhole pressure, and  $P_j$  is phase pressure at well cell.

$$Q_j = PI_j (P_{wf} - P_j) \quad \text{for } j = 1 \dots N_P. \quad (3.11)$$

The Peaceman's relation and the Babu and Odeh model have been implemented in UTCOMP to compute the productivity index. In the next chapter, where well-fracture intersection is investigated, more detail is presented about these models. In terms of well operating conditions, several constraints are available, such as constant flowing bottomhole pressure and constant flow rate.

### **3.2 UTGEL RESERVOIR SIMULATOR**

The UTGEL reservoir simulator is a specific version of the well-known chemical flooding compositional simulator, UTCHEM, developed at The University of Texas at Austin. UTGEL has developed and tuned additionally for modeling conformance control using several types of polymer gels through permeability reduction factors. However, it is still capable of modeling three-dimensional, non-isothermal, multiphase and multicomponent compositional problems, such as surfactant flooding, polymer flooding, tracer flooding, and non-isothermal EOR processes. In terms of the components, UTGEL can track water, oil, surfactant, polymer, anions, cations, alcohol, tracer, and up to seven gel species. The overall phases are aqueous phase, oleic phase, and microemulsion phase, all in the state of liquid.

Similar to UTCOMP, to discretize flow equations, a finite-difference approach is used, and the solution scheme is IMPES (Implicit solution of pressure equation followed by explicit solution of saturations). Also, an energy balance equation is solved explicitly to compute temperature changes due to heat transfer in the reservoir. Moreover, to increase the numerical accuracy of the solution schemes, higher-order methods are added to the formulations.

In the following sections, the governing equations of UTGEL are presented. Since the derivations follow the same concept as UTCOMP, the final forms of equations are only discussed. Later in Chapter 6, a brief discussion of UTGEL capabilities in modeling several types of gel conformance control is introduced. For more detail about the general features of UTGEL, one can refer to UTGEL Technical Documentation V.01 (2010). Also, since UTGEL is adopted from UTCHEM, more information about the formulations is found in Datta Gupta (1986), Saad (1989), and Bhuyan *et al.* (1990).

### 3.2.1 Governing Formulations

The overall mathematical formulation of UTGEL is described by three principal equations: mass balance for the volume occupying components, pressure equation obtained by an overall mass balance, and energy equation. There are other auxiliary relations used in every time step to calculate required properties.

#### 3.2.1.1 Mass Conservation Equation

If we start again from Eq. (3.1) and substitute the corresponding auxiliary equations in terms of mass per unit volume, we obtain a conservation statement, which is similar to Eq. (3.7) with equivalent parameters.

$$\frac{\partial(\phi\tilde{C}_\kappa\rho_\kappa)}{\partial t} + \vec{\nabla} \cdot \left[ \sum_{l=1}^{n_p} \rho_\kappa \left( C_{\kappa l} \vec{u}_l - \phi S_l \vec{\tilde{K}}_{\kappa l} \nabla C_{\kappa l} \right) \right] = R_\kappa \quad (3.12)$$

for  $\kappa = 1 \dots n_c$ ,

where

$\phi$  = Porosity

$\tilde{C}_\kappa$  = Overall volume concentration of component  $\kappa$

$\rho_\kappa$  = Mass density of component  $\kappa$

$n_p$  = Number of phases

$n_c$  = Number of components

$C_{\kappa l}$  = Volume concentration of component  $\kappa$  in phase  $l$

$\vec{u}_l$  = Velocity of phase  $l$

$S_l$  = Saturation of phase  $l$

$\vec{\tilde{K}}_{\kappa l}$  = Components of dispersion tensor

$R_\kappa$  = Source term for component  $\kappa$

In the above equation, the overall volume of component  $\kappa$  per unit volume is defined as

$$\tilde{C}_\kappa = \left(1 - \sum_{\kappa=1}^{n_{CV}} \hat{C}_\kappa\right) \sum_{l=1}^{n_p} S_l C_{\kappa l} + \hat{C}_\kappa \quad \text{for } \kappa = 1 \dots n_c, \quad (3.13)$$

where  $n_{CV}$  is the total number of volume occupying components,  $\hat{C}_\kappa$  is the adsorbed concentration of component  $\kappa$ , and  $\left(1 - \sum_{\kappa=1}^{n_{CV}} \hat{C}_\kappa\right)$  is reduction in pore volume due to adsorption. If we neglect the adsorption term and replace the mass concentration terms (i.e.  $\rho_\kappa C_{\kappa l}$ ) with molar concentrations (i.e.  $\xi_j x_{ij}$ ), we obtain Eq. (3.7).

### 3.2.1.2 Pressure Equation

To obtain the pressure equation, we need to examine the total material balance over all of the volume occupying components. Thus, if we sum Eq. (3.12) over all the volume occupying components and expand the derivation term on the left hand side, we get to the final form of pressure equation, which is applied to water phase:

$$\phi C_t \frac{\partial P_1}{\partial t} - \vec{\nabla} \cdot \vec{k} \lambda_{rTc} \vec{\nabla} P_1 = - \vec{\nabla} \cdot \sum_{l=1}^{n_p} \vec{k} \lambda_{rlc} \vec{\nabla} h + \vec{\nabla} \cdot \sum_{l=1}^{n_p} \vec{k} \lambda_{rlc} \vec{\nabla} P_{cl1} + \sum_{\kappa=1}^{n_{CV}} Q_\kappa, \quad (3.14)$$

where

$$\lambda_{rlc} = \frac{k_{rl}}{\mu_l} \sum_{\kappa=1}^{n_{CV}} \rho_\kappa C_{\kappa l}, \quad (3.15)$$

$$\lambda_{rTc} = \sum_{\kappa=1}^{n_{cv}} \lambda_{rlc}, \quad (3.16)$$

$$C_t = C_r + \sum_{\kappa=1}^{n_{cv}} C_{\kappa}^0 \tilde{C}_{\kappa}, \quad (3.17)$$

where

$C_t$  = Total compressibility

$C_r$  = Rock compressibility

$C_{\kappa}^0$  = Component compressibility

$P_1$  = Water phase pressure

$\lambda_{rlc}$  = Relative mobility with correction for fluid compressibility

$\lambda_{rTc}$  = Total mobility with correction for fluid compressibility

$h$  = Elevation with respect to datum

$P_{cl1}$  = Capillary pressure with respect to water

The other parameters are the same as the ones in material balance equation.

### 3.2.1.3 Energy Conservation Equation

Several chemical EOR processes are temperature-dependent. To determine temperature at every time step, we need to solve the energy balance equation. If we assume that advection and heat conduction are the only processes involved in heat transfer, we can solve the following energy balance equation to compute temperature.

$$\frac{\partial}{\partial t} \left[ (1-\phi) \rho_s C_{vs} + \phi \sum_{l=1}^{n_p} \rho_l S_l C_{vl} \right] T + \vec{\nabla} \cdot \left( \sum_{l=1}^{n_p} \rho_l C_{pl} u_l T - \lambda_T \vec{\nabla} T \right) = q_H - Q_L, \quad (3.18)$$

where

$T$  = Reservoir temperature

$C_{vs}$  = Rock heat capacities at constant volume

$C_{vl}$  = Phase  $l$  heat capacities at constant volume

$C_{pl}$  = Phase  $l$  heat capacities at constant pressure

$\lambda_T$  = Constant thermal conductivity

$q_H$  = Enthalpy source term per bulk volume

$Q_L$  = Heat loss to overburden and underburden formations

### 3.2.2 Initial and Boundary Conditions

Similar to UTCOMP, there are direct and indirect methods to input initial conditions for the reservoir model. Pressures, phase saturations, and components volume fraction are the properties whose values are required to start the simulation run. In terms of boundary conditions, the external boundaries are of no flow and no heat transfer; for the internal boundaries, i.e. wells, there are several operating conditions defined in the code.

The solution scheme for UTGEL is IMPES. For IMPES-type formulation, at first the pressure equation is solved implicitly. Then, after updating some properties, the mass balance equation for each component is solved explicitly. Finally, after updating the rest of the parameters, temperature is obtained by explicit solution of the energy balance equation.

## **Chapter 4: Overview of Embedded Discrete Fracture Model (EDFM) and the Implementation Approach**

The Embedded Discrete Fracture Model (EDFM) was originally proposed by Li and Lee (2008) to take advantage of the synergy between dual continuum and discrete fracture models. Later, this approach was developed further by Moinfar *et al.* (2012, 2014) to enhance its capability in modeling arbitrary oriented, dip angled fractures. Based on this model, the fractures are inserted explicitly in the matrix grid and are coupled with the matrix domain by the modified transmissibility factors.

To better understand the concept of EDFM, the methodology for fractures treatment and the derivation of the transmissibility factors are discussed in the next sections, followed by a number of simple examples. Moreover, Non-Neighboring Connections (NNC) approach is introduced in this chapter, which has been used to implement EDFM in UTCOMP and UTGEL reservoir simulators.

### **4.1 DUAL CONTINUUM AND DISCRETE FRACTURE MODELS SYNERGY**

Accurate and comprehensive models are required to capture the high degree of complexity associated with the fracture domain and to investigate the flow in fractured reservoirs. Several approaches have been proposed to simulate and study the behavior of fractured reservoirs (with natural and/or induced fractures). Dual continuum and discrete fracture models are the ones that are widely used in the industry.

The dual porosity and dual permeability (or dual continuum) approaches have the upper hand in terms of simplicity in gridding and in setting up the model parameters. Based on the dual continuum approaches, the pressure and the transport equations for the

two communicating grids are solved simultaneously using a finite-difference method (FDM). The gridding is straightforward for both the matrix and the fracture systems. Similar to conventional methods, the structured gridding is used to discretize both the matrix and the fracture domains, where one fracture control-volume is connected to every matrix gridblock. Often, the same grid is selected for discretization of both domains, although the fracture system can be discretized into coarser gridblocks. To account for the communication between these two coupled systems, a term, called the transfer function, is defined for every matrix gridblock. However, because of uncertainty over the structure and the geometry of fractures, defining the transfer function for real fractured reservoirs is very challenging. Figure 4.1 illustrates the configuration of a dual continuum approach for modeling a naturally fractured reservoir.

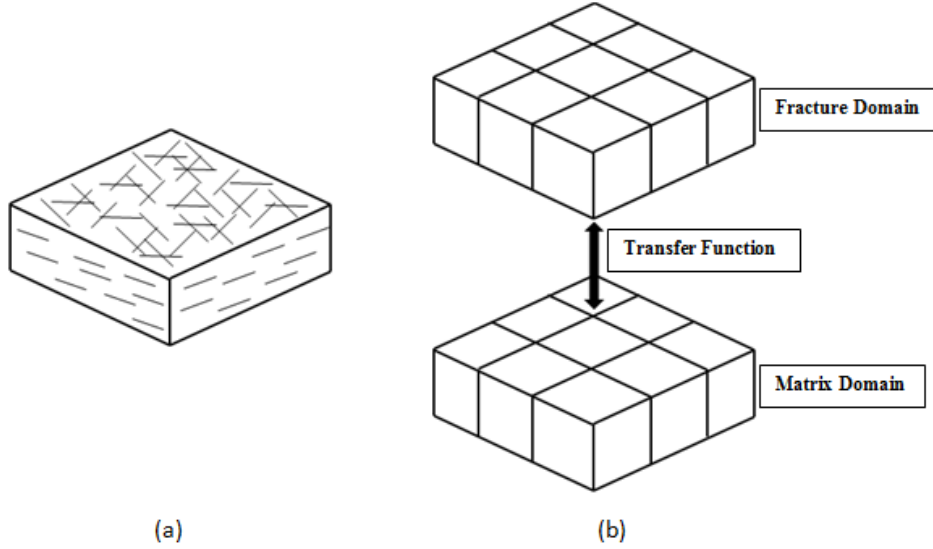


Figure 4.1: Configuration of the dual continuum approach: (a) Schematic of a naturally fractured reservoir, (b) and the corresponding coupled matrix and fracture domains.

The mentioned capabilities have made dual continuum models into one of the most popular approaches in the petroleum industry for studying naturally fractured reservoirs (NFR). However, on account of several major simplifications (in terms of upscaling the fractures effect), dual continuum models fail to represent problems with multi-scale, slanted, irregularly spaced, non-uniform fractures. These deficiencies become more significant when we are interested in investigating the effect of individual fracture planes on reservoir performance, such as in the case of hydraulically fractured reservoirs.

For a more accurate evaluation of the performance of fractured reservoirs, especially when few fractures dominate the fluid flow, discrete fracture modeling approaches have developed. To capture the complex configuration of fractures, unstructured grid is used in this approach, where the matrix block is represented by polygons and polyhedrons in 2D and 3D problems, respectively. Moreover, since the fracture aperture is not being considered in the gridding algorithm, fractures are discretized into segments and polygons in 2D and 3D problems, respectively (i.e. fractures have lower Euclidean dimensions). The communication of these control-volumes is then defined based on the modified transmissibility factors, Hence, the discrete fracture models enable explicit consideration of fracture entities.

The discrete fracture models, although more accurate compared to dual continuum methods, are still computationally expensive. To conform to the complex reservoir elements or geometries (such as fractures and irregular boundaries), the gridding algorithms tend to refine the cells as one gets closer to such features. Therefore, for a complex fracture configuration, a higher number of cells are required as shown in Figure 4.2, which in turn results in a significant increase in the computational time. Also, due to small volume of the refined cells next to the fractures, the numerical stability and

the time step size of the simulation runs are reduced. These problems, albeit alleviated significantly over the past few years, are the major obstacles to an expanded commercial use of the discrete fracture models in the petroleum industry.

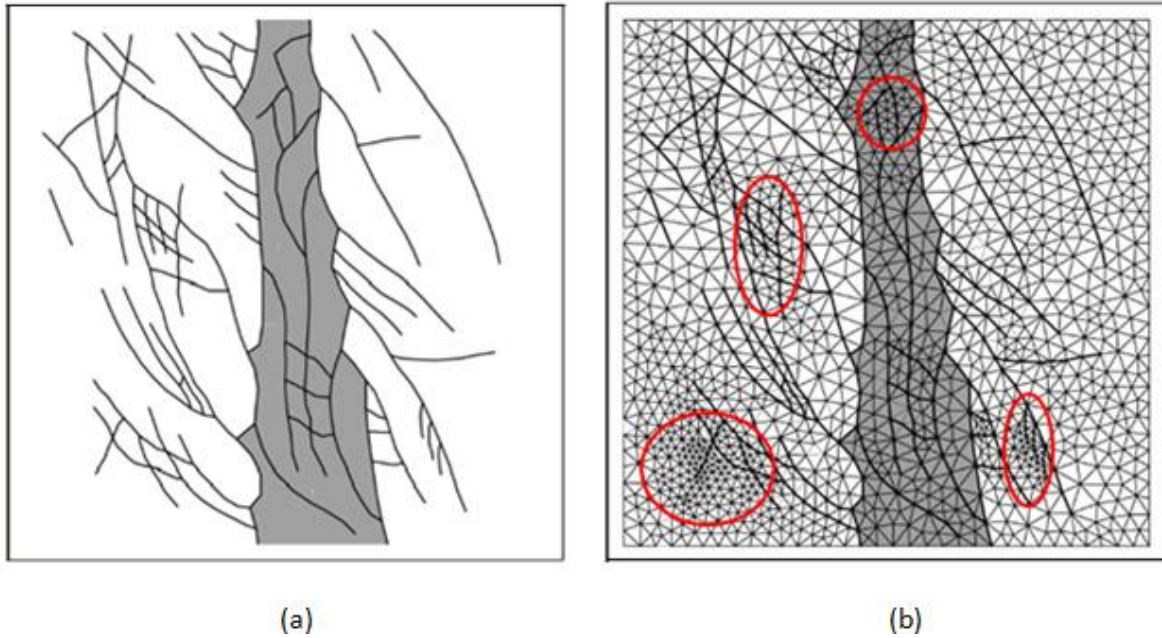


Figure 4.2: Schematic of a discrete fracture model (Karimi-Fard *et al.* (2004)): (a) A naturally fractured reservoir, and (b) the corresponding unstructured grid, in which the red ellipses highlight the regions with highly refined cells.

In view of pros and cons of the above discussed models, several methods have been proposed recently in the petroleum literature, offering methodologies to merge the dual continuum and discrete fracture models. In these new methods, the discrete fracture models are applied to achieve the transport parameters more accurately (including upscaled permeabilities, transfer functions, or transmissibility factors) by explicit consideration of individual fractures. These modified parameters are then utilized in a structured grid similar to dual continuum models. Hence, the accuracy of discrete fracture models is combined with the gridding convenience of dual continuum models.

The Embedded Discrete Fracture Model (EDFM) has developed recently based on the similar concept of dual continuum and discrete fracture models synergy. This model has been implemented in UTCOMP and UTGEL reservoir simulators to enhance their capabilities in modeling a variety of hydrocarbon recovery methods in fractured reservoirs. The following section describes in detail the EDFM methodology.

#### **4.2 EMBEDDED DISCRETE FRACTURE MODEL (EDFM)**

As mentioned above, the EDFM belongs to a new class of models that employ simultaneously the benefits of the dual continuum and the discrete fracture models in studying flow in fractured porous medium. In this class of models, the reservoir is divided into different domains based on the contrast between properties throughout the formation. Each domain is then characterized accordingly by the dual continuum or discrete fracture models to determine the effective properties. After examining each domain separately, a proper methodology is used to couple fluid flow between different domains and finally in the whole formation.

As a base for the EDFM concept, Lee *et al.* (2000, 2001) introduced a hierarchical approach to divide the fracture domain into three categories based on the fractures length-scale. These categories included short, medium-length, and long fractures compared to the size of the matrix gridblocks. The effects of the first two classes of fractures were upscaled and added to the original permeability tensor of the corresponding matrix gridblocks. However, the long-scale fractures were modeled explicitly using the similar formulation as well productivity equation, while a new parameter, the transport index, was used instead of the productivity index (PI). However, they did not explain exactly how to compute the transport index and instead used a fixed value due to numerical

instability in the presented problems. Also, for simplicity, they limited the long-scale fractures only to vertical rectangular planes.

For modeling short- and medium-length fractures, Lee *et al.* (2000, 2001) used an analytical solution and a boundary element method, respectively, to incorporate the effect of fractures on flow in the rock matrix. The permeability of the matrix gridblocks was then replaced by the effective permeability tensor derived from these two methods. In fact, to account for the effect of these types of fractures, a single porosity approach was utilized. However, using this technique, a separate analysis of flow in matrix and fracture domains was impossible. Therefore, dual continuum approach was preferred in the case where studying coupled flow between fracture and matrix systems was of more interest.

Later, Li and Lee (2008) improved the application of EDFM in modeling fracture networks. They introduced a mathematical approach to approximate the transmissibility index. In their model, the long-scale fractures were treated as 2D rectangular planes with arbitrary orientations, and the transmissibility factors were defined based on the geometry and the position of the fracture planes inside the matrix grid. Moreover, they proposed a similar method that allowed inclusion of the well-fracture intersection. They assumed negligible pressure drop in the fracture segment bounded inside the well block; therefore, they used the same definition of the transmissibility factor as the productivity index to account for well-fracture flow.

Although Li and Lee (2008) provided a suitable approach to model naturally fractured reservoirs, they limited their study only to simple fracture configurations such as vertical rectangular planes. Also, they focused more on the fluid transfer between fracture and matrix gridblocks and skipped the explanation for calculating the transmissibility index between two intersecting fracture planes.

To enhance the capability of EDFM in modeling more realistic fractured

reservoirs, Moinfar *et al.* (2012, 2014) extended the scope of the model to investigate arbitrary dip-angled fracture planes with dynamic properties. They devised a systematic approach to compute the fluid exchange in matrix-fracture, fracture-fracture, and well-fracture combinations. Moreover, they proposed a framework to implement EDFM into conventional reservoir simulators working with structured grids. They incorporated EDFM in the General Purpose Adaptive Simulator (GPAS), developed under fully implicit formulation scheme, and examined several production scenarios in naturally and hydraulically fractured reservoirs. They demonstrated that application of EDFM with a proper specification of the gridblock size results in accurate and also computationally efficient simulation runs compared to the fine-grid simulations.

The successful implementation of EDFM in the GPAS brought up the question whether or not EDFM is applicable in IMPES-type reservoir simulators (Implicit Pressure, Explicit Saturation) as well. Although IMPES formulations are less stable, they require less numerical effort and are more accurate in most of the reservoir simulation problems compared to the fully implicit solution techniques. In addition, adding new features to the IMPES-type reservoir simulators is much easier. These benefits have made the IMPES formulation scheme to one of the most popular methods for development of new reservoir simulators in the petroleum industry. Hence, incorporating the EDFM with the available IMPES-type in-house reservoir simulators enables us to investigate a broad range of reservoir engineering applications in fractured reservoirs.

To evaluate the performance of EDFM using IMPES-type formulations, this model has been implemented in the UTCOMP and UTGEL reservoir simulators. To do so, a similar methodology to the one proposed by Moinfar (2013) is used, which is described in detail in the following sections. Moreover, due to the differences in the formulation schemes, several modifications have been made that are discussed later in

this chapter.

#### 4.2.1 Methodology

According to the work of Lee *et al.* (2001), Li and Lee (2008), and Moinfar (2013), EDFM has developed based on the combined advantages of the dual continuum and discrete fracture models. To capture all the possible complexities inherent in the fracture network, a discrete modeling approach is selected to treat the fractures. However, to simplify the setting of the model parameters and to achieve convenient representation of the reservoir geometry, the rock matrix is discretized using structured grids. In fact, the matrix gridding is somehow independent of the fracture network configuration.

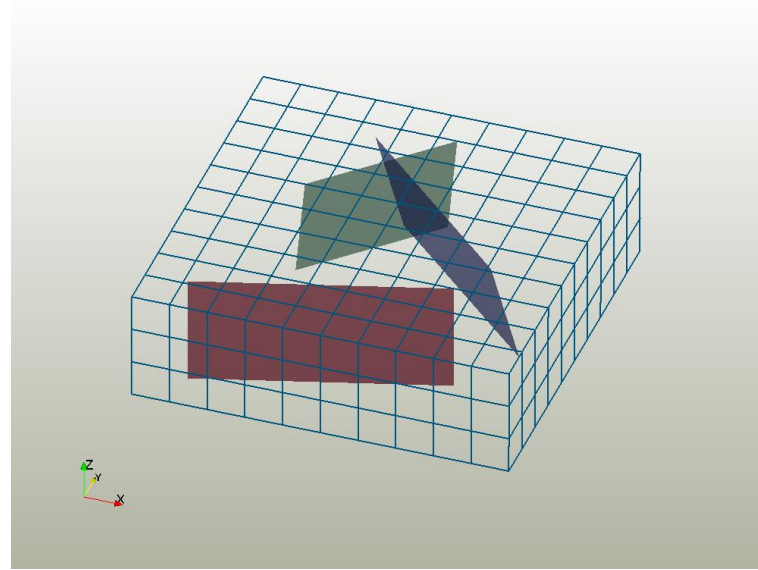
To set up a reservoir model using EDFM, two coupled domains are required, the matrix domain and the fracture system. The matrix domain consists of one or more layers of cubic blocks known as structured gridblocks. The number and the size of the matrix gridblocks depend on the type of the problem and also the numerical aspects. The smaller the size of the gridblocks, the more accurate solution is obtained; however, the computational cost is sacrificed. On the topic of sensitivity analysis on the size of the matrix gridblocks, a discussion is presented in Chapter 5. To represent the fracture system, however, 2D rectangular planes are used in which the position of each fracture plane is determined using the coordinates of the rectangle vertices. Figure 4.3 depicts a simple model containing three fracture planes. As observed in the figure, the fracture planes can have arbitrary orientation and dip angles and are not necessarily aligned with the major coordinate axes. As seen in the top view of the model (Figure 4.3b), since the red fracture is perpendicular to the bedding plane, it is displayed as a line while the other two inclined fractures appear as rectangles in the map view. The dip angles of the green

and the blue fractures are 10 and 15 degrees, respectively.

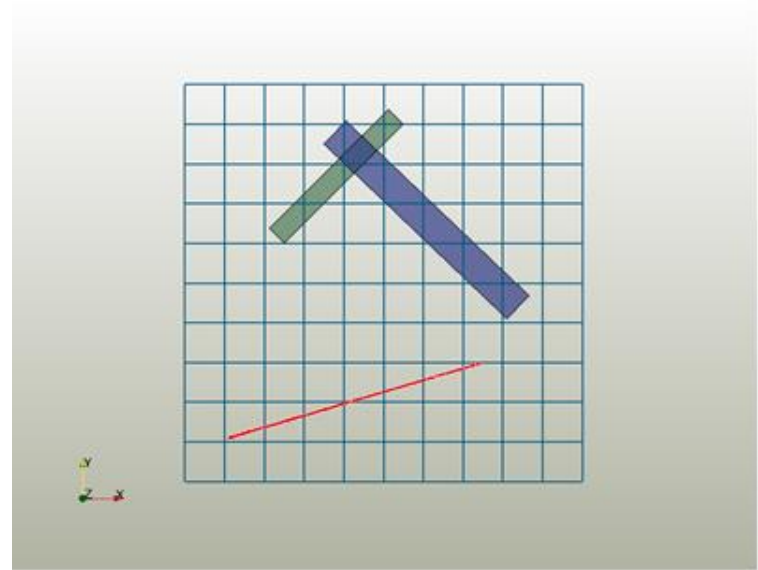
Depending on position, orientation, dip angle, and height of fracture planes, each rectangle cuts through several gridblocks in each layer. To check whether or not a gridblock is intersected by a fracture plane, the position and the coordinates of blocks vertices are checked against the rectangular plane equation. Figure 4.4 illustrates the gridblocks intersected by the fracture planes in different layers for the reservoir model presented in Figure 4.3. The color of each gridblock represents the color of the fracture plane that has intersected that specific gridblock. If a block is cut by more than one fracture, it is shown in purple. As presented in Figure 4.4, since the red fracture is vertical, the intersection pattern remains the same from top layer to the bottom. However, for the green and the blue fractures, the intersection pattern as well as the number of intersected gridblocks changes from one layer to another due to the dip angle.

As a result of the intersection between rectangular planes and the matrix grid, each fracture is cut into several pieces by the block boundaries. Each fracture piece is considered as a control-volume and is accounted for in the mass balance calculation and in the fluid exchange between fracture and matrix gridblocks. Before running a simulation problem, a list of the corresponding fracture control-volumes and matrix gridblocks is generated and used as an input for the reservoir simulator.

Depending on the orientation and the dip angle of fracture planes, the intersection between a fracture plane and a gridblock is a polygon with 3 to 6 vertices. All the five possible shapes for the intersections are illustrated in Figure 4.5. If the fracture plane is perpendicular to the bedding, then regardless of the plane orientation, the intersection would be a rectangle (Figures 4.5a & 4.5b).



(a)



(b)

Figure 4.3: Representation of a fractured reservoir model using the EDFM concept: (a) Angled view highlighting vertical and inclined fractures, and (b) top view.

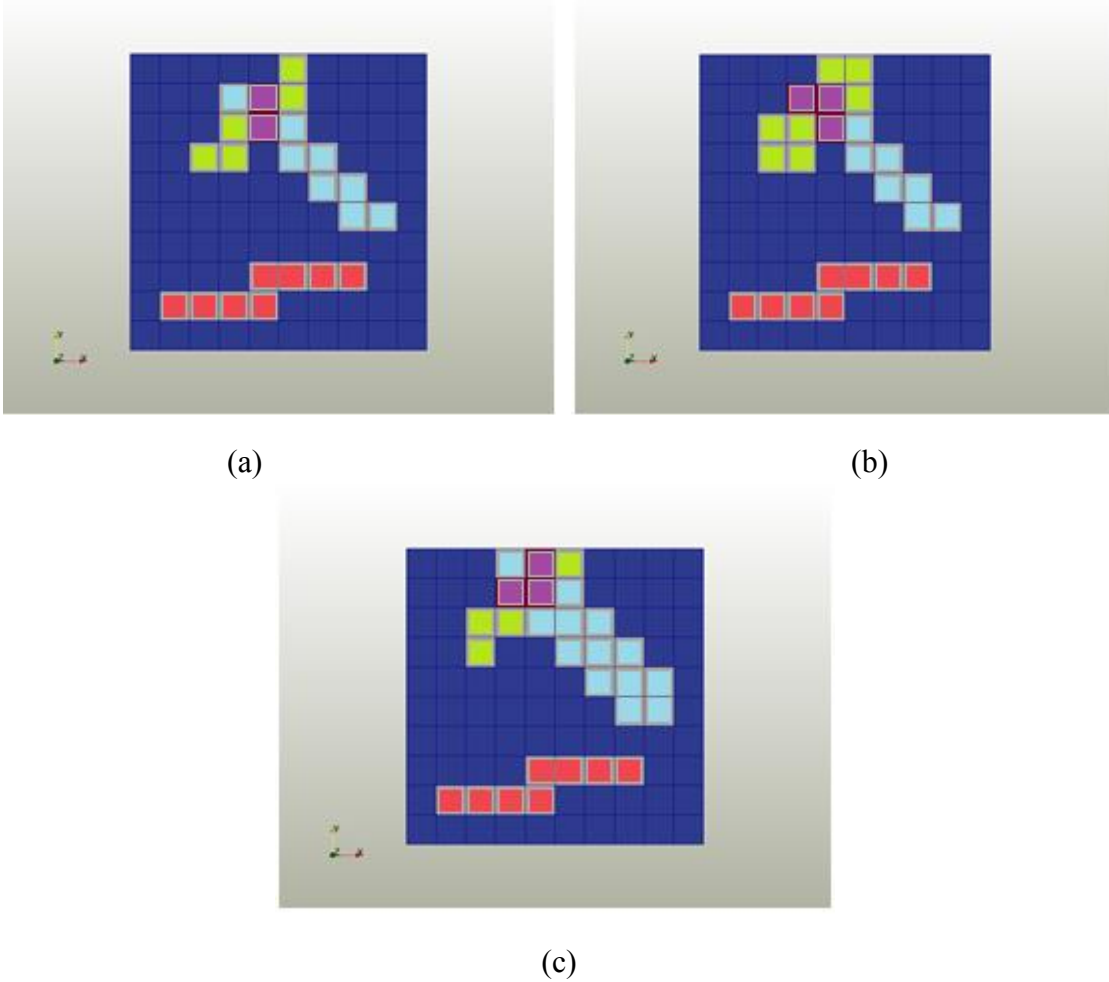


Figure 4.4: Color-coded illustration of the gridblocks intersected by the matching color fractures in the (a) first, (b) second, (c) and third layers. The gridblocks with multiple intersections are shown in purple.

In general, in EDFM, although the rock matrix domain contains structured blocks, the fracture planes are discretized into unstructured elements. Similar to the discrete fracture models, the fractures are of lower dimensions compared to the matrix cells and are discretized into 2D unstructured elements. The fracture discretization depends mainly on the geometry of the fractures and also on the matrix gridblock dimensions. For the case of inclined fractures, the plane may be discretized into segments with various sizes

and shapes.

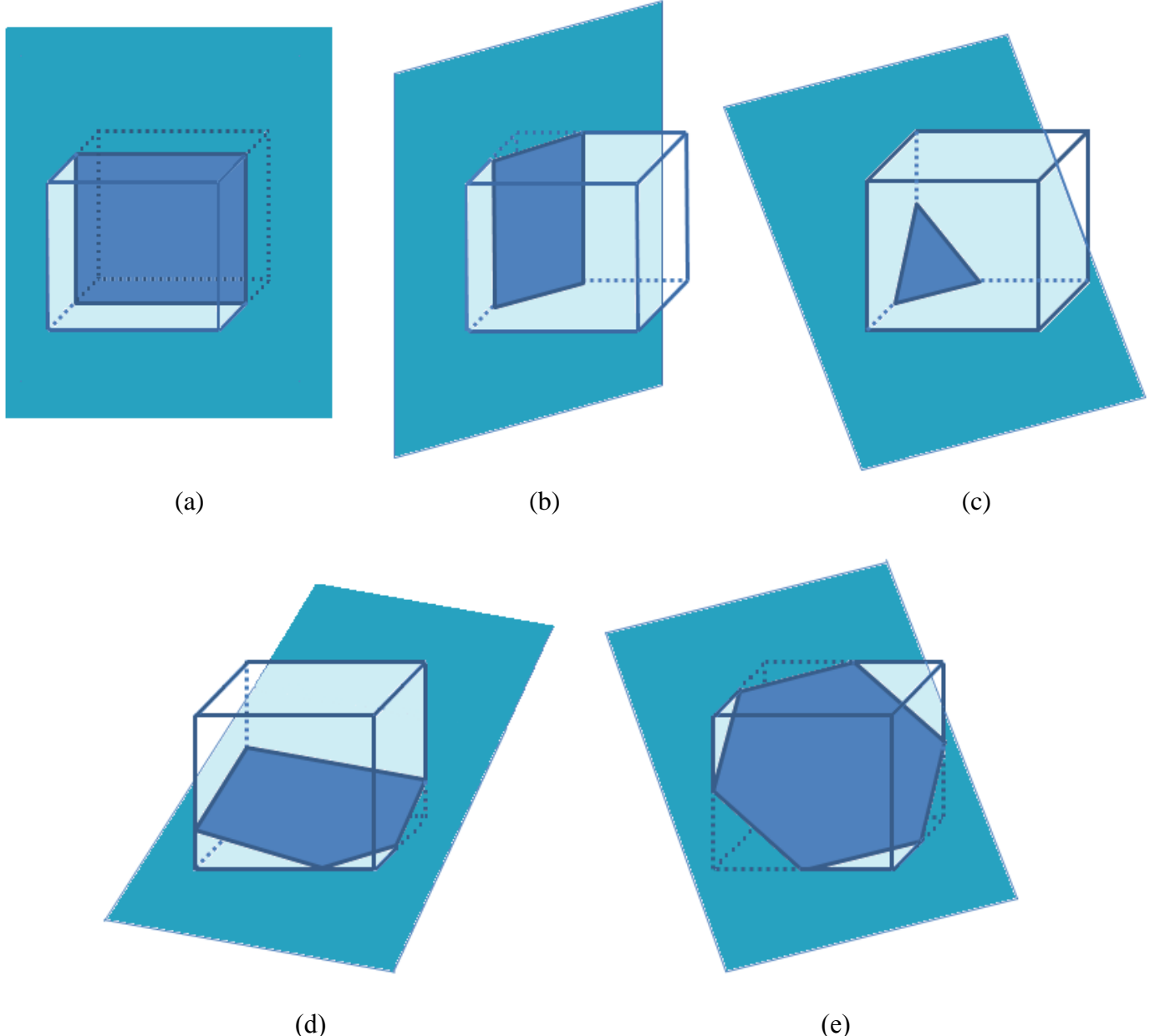
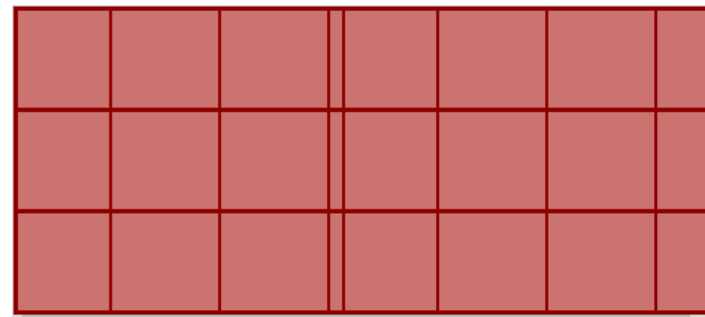


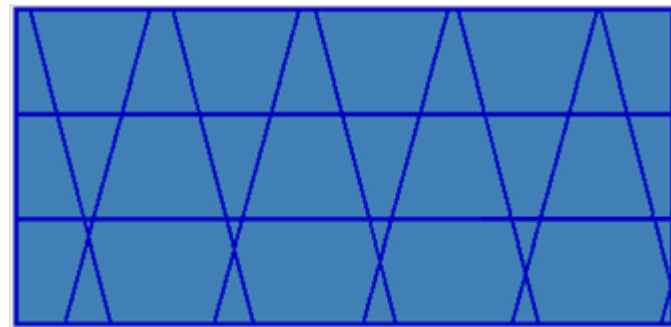
Figure 4.5: Possible shapes of the intersection between a plane and a cube: (a) rectangle (intersection points are on the parallel cube edges) (b) rectangle (intersection points are on the adjacent cube edges) (c) triangle (d) pentagon (e) hexagon.

Figure 4.6 illustrates the discretization of the three fracture planes presented in the previous example. The planes have been discretized by boundaries of the intersected gridblocks in all the three layers. Based on this figure, the shape and the size of the fracture segments vary significantly, even in the case of the vertical fracture. Although all of the segments are rectangular, as the intersection between the vertical fracture (red plane) and the grid system, there are thin pieces in the middle of the plane where the plane has almost cut the corner of a few gridblocks. On the other hand, for inclined fractures, the discretized segments are different polygons. For instance, the slanted fractures (the blue and green planes) consist of triangular, quadrilateral, pentagonal, and hexagonal shapes located next to each other. The summation of all of these pieces adds up to the original fracture planes. In terms of the size of the segments, a number of small triangles have been formed (Figure 4.6b and 4.6c) as a result of the intersection between the fracture planes and the corner of matrix blocks. These small portions can cause numerical problems and can increase simulation time substantially.

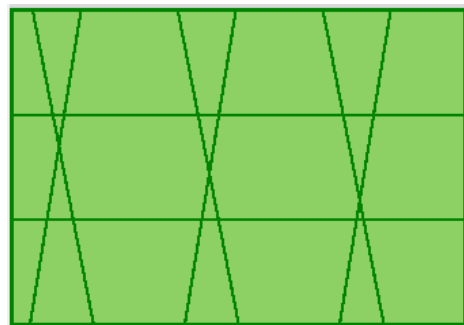
In general, each fracture segment is a control-volume, similar to matrix gridblocks, and is characterized by rock and fluid properties. To compute such attributes, exact calculations of the shape and the geometry of the fracture segments are necessary. Parameters such as permeability, porosity, and transmissibility factors of the fracture control-volumes are strongly dependent on the shape and configuration of the fracture planes. The permeability of the fractures either can be derived using the aperture based formulations or can be used as an input directly. However, to compute porosity and transmissibility factors, the surface area of each fracture control-volume confined in the matrix block is required. Eq. (4.1) represents the porosity of each fracture control-volume



(a)



(b)



(c)

Figure 4.6: Fracture planes discretization for the example reservoir model. (a) Red vertical fracture plane is composed of only rectangular segments. (b) Blue inclined fracture plane with 15 degree dip angle is composed of triangular, quadrilateral, pentagonal, and hexagonal segments. (c) Green inclined fracture with 10 degree dip angle is composed of triangular, quadrilateral, pentagonal, and hexagonal segments.

as a function of the surface area of the fracture segment. In Eq. (4.1),  $(\phi_f)_i$ ,  $\omega$ , and  $(A_f)_i$  are porosity, aperture, and surface area of the fracture segment number  $i$ , respectively; and  $\Delta x$ ,  $\Delta y$ , and  $\Delta z$  are the dimensions of the matrix gridblock corresponding to the fracture cell number  $i$ . As realized from this equation, small surface area of a segment results in a very low porosity compared to other adjacent control-volumes, especially matrix gridblocks. As mentioned before, this contrast may cause numerical and time step problems over the simulation run.

$$(\phi_f)_i = \frac{(A_f)_i \times \omega}{(\Delta x \times \Delta y \times \Delta z)_i}. \quad (4.1)$$

As mentioned previously, each fracture control-volume is connected to a matrix gridblock. In addition, due to fracture discretization, each segment is connected to neighboring fracture cells as well. Thus, for solving mass balance equations, all of these connections must be taken into account in order to calculate fluid exchange between the neighboring cells. To do so, the transmissibility factor between every adjacent pair needs to be computed. For connections involving a fracture control-volume, the transmissibility factor is modified to reflect the geometry and properties of the fracture. In the subsequent section, these new types of connections are classified into four groups and then the formulation for calculating the transmissibility factor for each type is defined.

#### 4.2.2 Fracture Connections in EDFM

After finishing the discretization process, to study the fluid flow in a coupled matrix-fracture system, the connections between communicating control-volumes need to be quantified. For neighboring matrix gridblocks, the transmissibility factors have already been derived and used in conventional reservoir simulators. However, due to explicit consideration of fractures embedded inside the matrix grid, and the unstructured nature of the discretization, the transmissibility factors for connections involving a fracture cell have to be modified.

Although Li and Lee (2008) introduced an approach to approximate the transmissibility index between a fracture and the corresponding matrix gridblock, the more systematic formulation was proposed by Moinfar *et al.* (2012). They defined three types of new connections in EDFM for the communicating matrix and fracture cells. Since they arranged a separate computational domain for fractures than the matrix grid, they used the concept of Non-Neighboring Connections (NNC) to numerically attach the communicating fracture and matrix cells. They then defined a few formulations based on cell properties to compute the transmissibility factors for NNC types I, II, and III. The subsequent sections overview these formulations and the process for deriving the parameters.

The transmissibility factors for the three types of NNCs are derived based on the similar concept of flow rate calculation between two adjacent gridblocks using the multiphase Darcy formulation for 1D flow (Eq. (4.2)). In this equation, the subscript  $j$  denotes the phase number and  $i+1/2$  refers to the block face between the gridblocks number  $i$  and  $i+1$ . Based on this equation, the flow rate for each phase between two neighboring matrix gridblocks is proportional to the potential difference. In some notations, the proportionality constant is called the “transmissibility,” which consists of

time-dependent parameters, such as phase relative permeability ( $k_{rj}$ ) and viscosity ( $\mu_j$ ), and constant properties, such as absolute permeability ( $k_{i+1/2}$ ), area ( $A_{i+1/2}$ ) and the size of the gridblocks ( $d_{i+1/2}$ ). For our discussion, we use “transmissibility factor” to refer to the constant portion of the transmissibility. The definitions of transmissibility and transmissibility factor are given by Eqs. (4.3) and (4.4), respectively.

$$(q_j)_{i+1/2} = -A_{i+1/2} \frac{k_{i+1/2} k_{rj}}{\mu_j} \frac{1}{d_{i+1/2}} \left( (\Phi_j)_{i+1} - (\Phi_j)_i \right) = (T_j)_{i+1/2} \left( (\Phi_j)_{i+1} - (\Phi_j)_i \right). \quad (4.2)$$

$$(T_j)_{i+1/2} = A_{i+1/2} \frac{k_{i+1/2} k_{rj}}{\mu_j} \frac{1}{d_{i+1/2}}. \quad (4.3)$$

$$T_{i+1/2} = \frac{k_{i+1/2} A_{i+1/2}}{d_{i+1/2}}. \quad (4.4)$$

For more accurate estimation of the block face properties (subscripted by  $i+1/2$ ), averaging techniques are required to incorporate the properties of both neighboring gridblocks. For instance, harmonic average is used to compute the absolute permeability at the face between two gridblocks, while arithmetic average is used to calculate the average block size. Inserting the average properties back into the Eq. (4.4) yields

$$T_{x+1/2} = \frac{2\Delta y \Delta z}{\left( \frac{\Delta x}{k_x} \right)_i + \left( \frac{\Delta x}{k_x} \right)_{i+1}}, \quad (4.5)$$

where  $T_{x+1/2}$  is the transmissibility factor between two adjacent gridblocks in the X-

direction;  $k_x$  is the absolute permeability in X- direction; and  $\Delta y$ ,  $\Delta x$ , and  $\Delta z$  are the gridblock dimensions. Thus, if we compute the appropriate equivalent transmissibility factors for the connections involving a fracture cell, we can use Eqs. (4.2) and (4.3) to compute the fluid exchange between fracture-matrix and fracture-fracture cells. However, since fracture cells are unstructured elements, the definition of dimensions of a fracture control-volume would be different compared to a structured matrix gridblock.

Moinfar *et al.* (2012) proposed an approach, mainly based on the work of Li and Lee (2008) and Karimi-Fard *et al.* (2004), to derive the transmissibility factors between fracture-matrix and fracture-fracture cells. This approach was developed basically based on Eq. (4.4) to compute every term in this equation honoring the geometry and the shape of the fracture segments. Hence, accurate approximations of the position and the surface area of the individual fracture segments are of critical importance in this approach. In the following sections, the different types of fracture connections and the corresponding formulations for calculating transmissibility factors are discussed.

#### **4.2.2.1 Matrix-FractureConnection**

This type of connection, known as NNC type I, is created as the result of intersection between a fracture plane and a matrix gridblock. Every term in the Eq. (4.4) is computed based on the position and the properties of the matrix gridblock and the fracture segment. The calculated transmissibility factor is then used to connect these two cells in the computational domain (Figure 4.7).

For this type of connections, the average permeability ( $k_{m-f}$ ) is defined as the harmonic average of the corresponding matrix and fracture permeabilities. The subscript  $m-f$  refers to the matrix-fracture connection. The area ( $A_{m-f}$ ) is the fracture segment

surface area bounded inside the gridblock. Unlike the average permeability, the area changes from segment to segment due to the geometry and configuration of the intersections (Figure 4.6).

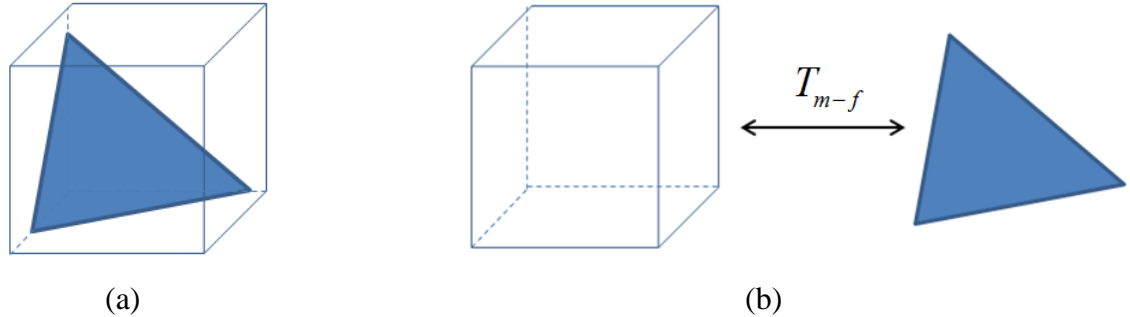


Figure 4.7: Schematic of a fracture-matrix connection, known as NNC type I. (a) This intersection is considered in (b) the computational domain through a non-neighboring connection with an equivalent transmissibility factor ( $T_{m-f}$ ).

For the average distance between matrix and fracture control-volumes ( $d_{m-f}$ ), Li and Lee (2008) proposed an integral equation to calculate the average normal distance  $\langle d \rangle$  (Eq. (4.6)). They assumed that pressure everywhere in the gridblock is equal to the cell average pressure and flow is always perpendicular to the fracture segment. Later, the following equation was used by Hajibeygi *et al.* (2011) and Moinfar *et al.* (2012) to calculate the normal distance in 3D problems. In this equation,  $n$  is the unit normal vector to the fracture plane;  $dv$  is the volume element;  $V$  is the volume of the matrix gridblock; and  $x$  is the vector locating the volume element. The integral in the numerator is calculated using a numerical method. Further examples are available in Hajibeygi *et al.* (2011) and Moinfar *et al.* (2012).

$$d_{m-f} = \frac{\int n \cdot x \, dv}{V}. \quad (4.6)$$

Using all of the derived parameters, the following equation is used, similar to Eq. (4.4), to calculate the equivalent transmissibility factor for the connection between a fracture segment and a matrix gridblock. It is important to mention that every fracture segment has only one connection of this type, while a matrix gridblock can have many.

$$T_{m-f} = \frac{k_{m-f} A_{m-f}}{d_{m-f}}. \quad (4.7)$$

#### **4.2.2.2 Fracture-Fracture Connection (of two Different Fracture Planes)**

When two fracture planes intersect each other, in a number of matrix gridblocks, the created fracture segments cross each other as well. For example in Figure 4.3, the blue and green fractures intersect each other in some of the gridblocks. Hence, after fracture discretization, segments containing a piece of the intersection line communicate to each other. This type of connections is known as NNC type II in Moinfar *et al.* (2012). Figure 4.8 depicts the track of the intersection line on the blue and green fractures after discretization. The fracture segments containing the matching color parts of the intersection line are connected in the computational domain. This type of connection is defined based on the equivalent transmissibility factor as shown in Figure 4.9. Although eight gridblocks have more than one fracture segments (colored in purple in Figure 4.4), only four of them have intersecting segments (shown in Figure 4.8). In fact, in other cases, the two fractures pass through the gridblocks but they do not intersect each other.

To calculate the transmissibility factor for NNC type II, a formulation by Karimi-

Fard *et al.* (2004) is applied. Based on Eq. (4.8), this transmissibility factor is derived as the harmonic average of the transmissibility factors of each individual fracture cell given by Eq. (4.9), where  $\omega$  is aperture and  $L_{\text{int}}$  is length of the intersection line between two fracture segments. The subscripts  $f$  and  $f'$  denote two different fracture planes. Unlike NNC type I, there is no limitation on the number of NNC type II for a fracture segment.

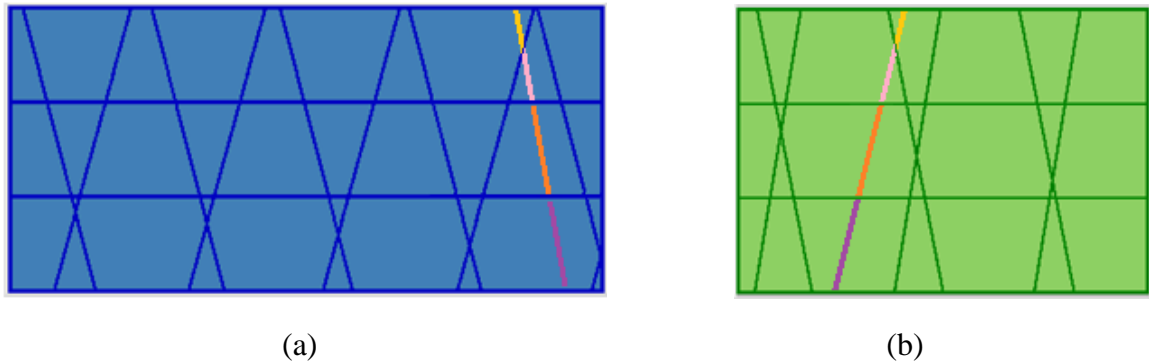


Figure 4.8: Discretized fracture planes with track of the intersection line. Segments containing the matching color part of the intersection line are connected in the computational domain.

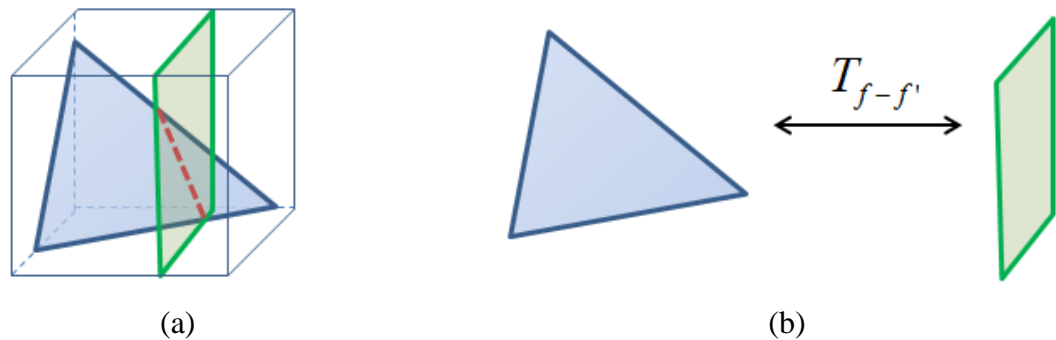


Figure 4.9: Schematic of a fracture-fracture connection of two different fracture planes, known as NNC type II. (a) This intersection is considered in (b) the computational domain through a non-neighboring connection with an equivalent transmissibility factor ( $T_{f-f'}$ ).

$$T_{f-f'} = \frac{T_1 T_2}{T_1 + T_2}. \quad (4.8)$$

$$T_i = \frac{k_{fi} \omega_{fi} L_{int}}{d_{fi}} \quad i=1,2. \quad (4.9)$$

#### 4.2.2.3 Fracture-Fracture Connection (of the Same Fracture Plane)

Similar to the matrix domain, when a fracture plane is discretized, neighboring segments must be connected in the computational domain. This type of connection exists only between segments of the same fracture plane and is known as NNC type III in Moinfar *et al.* (2012). Since a fracture segment can have up to six edges, the maximum number of connections of this type is six in the computational domain. Based on Figure 4.6, this type of connection is similar to the connections between 2D unstructured matrix gridblocks in a corner point problem. The expression for the transmissibility factor is presented by Eq. (4.10) in which  $k_f$  is the fracture permeability;  $d_f$  is the distance between centers of two neighboring cells; and  $A_f$  is the open face between two cells and is computed as aperture times length of the common edge. Figure 4.10 shows two fracture cells discretized by adjacent matrix gridblocks. In addition to matrix blocks, these fracture control-volumes communicate with each other as well.

$$T_{f-f} = \frac{k_f A_f}{d_f}. \quad (4.10)$$

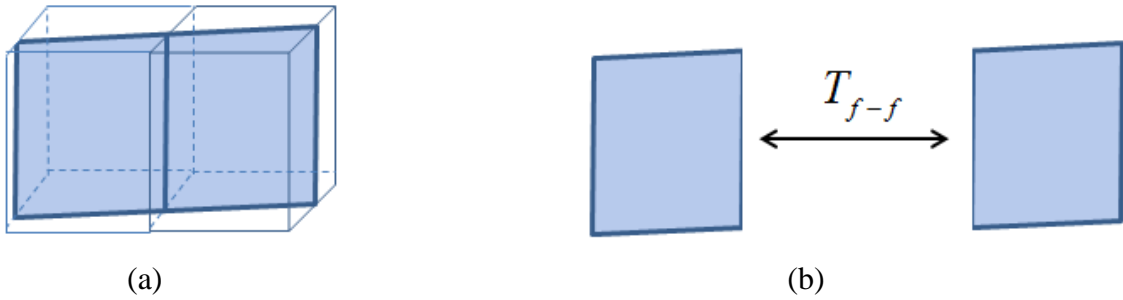


Figure 4.10: Schematic of a fracture-fracture connection of same fracture plane, known as NNC type III. (a) This connection is considered in (b) the computational domain through a non-neighboring connection with an equivalent transmissibility factor ( $T_{f-f}$ ).

#### 4.2.2.4 Well-FractureIntersection

When a well intersects a fracture, or when it is stimulated with a hydraulic fracturing job, the most important feature that controls the well flow is the fracture connection. In tight and unconventional reservoirs, almost all the fluid first gets into the fracture and then into the well. Thus, how the well-fracture communication is modeled is vital. To model well-fracture intersection, Moinfar *et al.* (2012) used a methodology similar to the Peaceman (1983) model to relate the well flow rate to the fracture segment pressure through which the intersection has occurred.

In numerical reservoir simulation, the relation between volumetric well rate,  $Q_j$ , and the pressure difference between bottomhole and gridblock pressures,  $(P_{wf} - P_j)$ , is defined as

$$Q_j = PI_j(P_{wf} - P_j), \quad (4.11)$$

where  $PI_j$  is the productivity index and is described by the following equation for a vertical well in a three-dimensional reservoir.

$$PI_j = \frac{\sqrt{k_x k_y} \Delta z}{\ln(r_o / r_w)} \lambda_{rj} = (WI) \lambda_{rj}. \quad (4.12)$$

In Eq. (4.12), the fraction on the right hand side, called the well index ( $WI$ ) in literature, consists of well block dimension, absolute permeabilities, and well radius. Moreover, the term  $r_o$  is given by an expression introduced by Peaceman (1983), which similarly includes well block dimensions and absolute permeabilities (Eq. (4.13)).

$$r_o = \frac{\sqrt{\left(\frac{k_y}{k_x}\right)^{0.5} \Delta x^2 + \left(\frac{k_x}{k_y}\right)^{0.5} \Delta y^2}}{\left(\frac{k_y}{k_x}\right)^{0.25} + \left(\frac{k_x}{k_y}\right)^{0.25}}. \quad (4.13)$$

Therefore, based on Eqs. (4.12) and (4.13), if we know the absolute permeabilities and the well radius, all we need to compute the well index is the size of the matrix gridblock containing the well. Figure 4.11a shows the required dimensions for the above formulations. Moinfar *et al.* (2012) used the same analogy to find the dimensions of a fracture segment intersecting a well. By replacing the fracture cell dimensions and setting the directional absolute permeabilities to be equal, Eqs. (4.14) and (4.15) are derived for calculating  $WI$  and  $r_o$  when a vertical well is intersected by a fracture segment. Figure 4.11b shows the corresponding fracture cell dimensions. Likewise, the equations for a horizontal well intersected by a transverse fracture are computed based on the

corresponding dimensions.

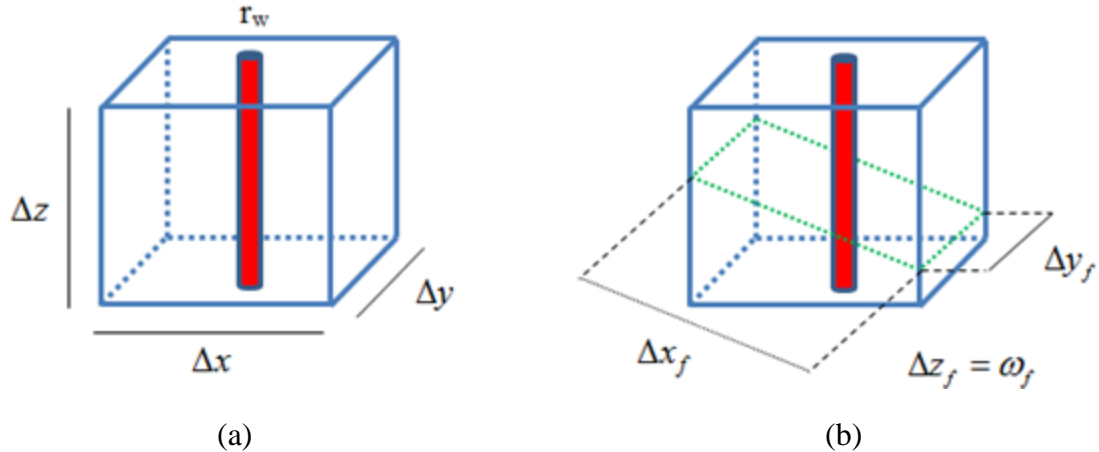


Figure 4.11: Illustration of the control-volume dimensions used in the definition of well index for (a) a matrix gridblock containing a well (b) and a fracture segment intersecting a well. The fracture segment bounded inside the gridblock is shown in green. The vertical dimension for the fracture is equal to the aperture.

$$WI_{w-f} = \frac{k_f \omega_f}{\ln\left(\frac{r_o}{r_w}\right)}. \quad (4.14)$$

$$r_o = 0.14 \sqrt{\Delta x_f^2 + \Delta y_f^2}. \quad (4.15)$$

#### **4.3 PREPROCESSING CODE**

To run a fractured reservoir simulation problem using EDFM approach, a few sets of new parameters are required to be added to the original input file. As discussed in preceding sections, due to introduction of fracture planes into a grid of matrix blocks, new types of control-volumes as well as new inter-cell communications are created. A preprocessing code has been developed outside the reservoir simulator environment by Cavalcante Filho *et al.* (2015), written in Python, to accurately locate the fracture planes and to calculate the EDFM parameters for the simulation runs carried out by UTCOMP-EDFM and UTGEL-EDFM reservoir simulators. In the preprocessing code, first, the fracture planes discretization is performed based on the location and geometry of the fractures and then the total number of fracture cells is determined. After calculation of the properties of fracture cells, all the created segments are added to the initial computational domain composed of the matrix gridblocks. Next, to account for fluid communication between non-neighboring control-volumes, the transmissibility factors are computed based on the methodology described in the previous section. Finally, after full characterization of the model, a list of required parameters is printed in one or more input files to be attached to the main reservoir simulator input file. The new inputs include porosity, permeability, depth, and dimensions of every cell, number of non-neighboring connections, list of non-neighboring connections and the corresponding transmissibility factors, and the well indices for well-fracture intersections. Figure 4.12 depicts the framework for modeling and simulation of flow in fractured reservoirs using EDFM approach.

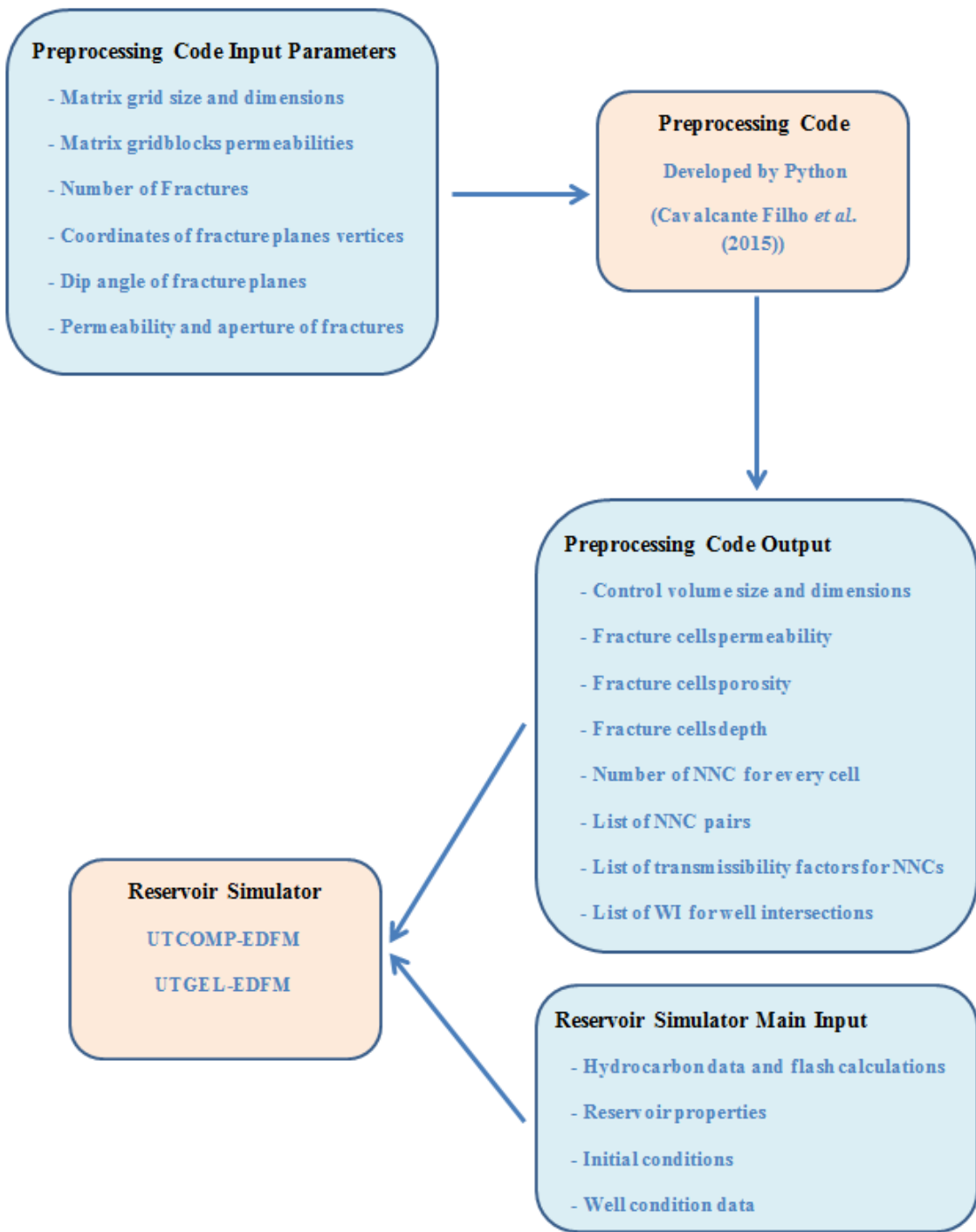


Figure 4.12: Framework for modeling flow in fractured reservoirs using EDFM approach.

Until this stage, the fractured reservoir model has been broken down to a series of matrix and fracture control-volumes and a tool has been provided to quantify cell properties and transmissibility factors. Next, in order to perform a reservoir simulation study, all the cells need to be put together again in the computational domain. To do so, the original structures of the UTCOMP and UTGEL reservoir simulators need to be modified. In the subsequent sections, the methodologies for such modifications are introduced through the concept of non-neighboring connections, and the most efficient approach is specified.

#### **4.4 NON-NEIGHBORING CONNECTION METHODS**

Non-Neighboring Connection (NNC) is defined as a connection between two control-volumes or cells that are not physically adjacent to each other in the computational grid domain. In a general three-dimensional problem, each gridblock, at maximum, is connected to six other gridblocks (two in X-, two in Y-, and two in Z-directions) (Figure 4.13). Locating these six cells in a cubical grid system follows simple procedures by inclusion of the conventional numbering techniques (which start numbering gridblocks first in X-direction, then Y-, and finally to the next layer or Z-direction). In conventional simulators, all these six gridblocks are accounted as neighboring cells. In order to account for fluid transfer between a matrix gridblock and a fracture control-volume bounded inside the block (Figure 4.7), we need to add extra connections. However, since the number of neighboring connections cannot exceed six in the computational grid, to do so, these new types of connections have to be defined through non-neighboring connections. In fact, the communication between a matrix block and a fracture segment occurs in a direction rather than the major coordinates. Later,

these extra connections are used in solving mass balance and pressure equations as well. The amount of fluid that transfers between a matrix and fracture cells through these routes is significant and needs to be accounted for.

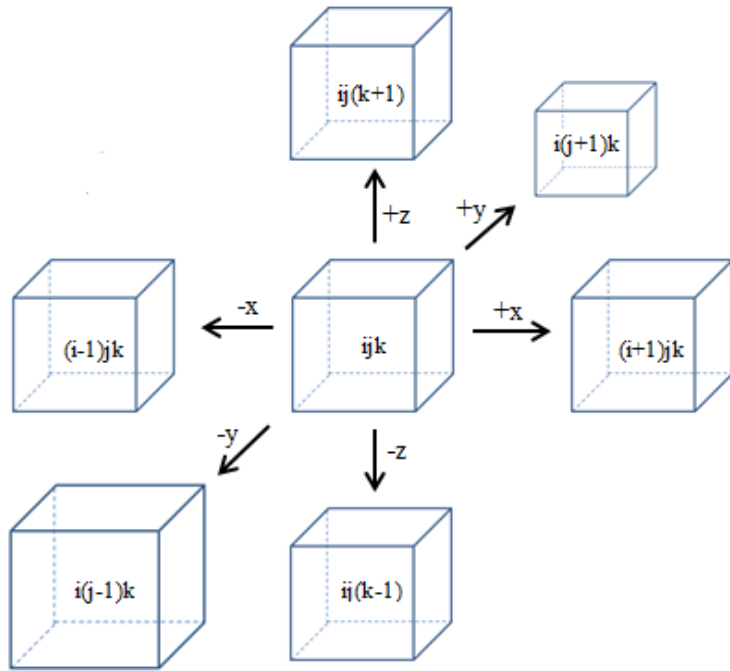


Figure 4.13: Neighboring connections in a conventional computational grid.

As a simple example of non-neighboring connections, we consider a  $3 \times 3$  grid domain that contains a single non-orthogonal fracture (Figure 4.14). As shown in this illustration, the fracture line hits a number of gridblocks creating new interactions. To better understand the grid connectivity, the connections between communicating cells are depicted in a matrix format in which the X represents the connection between two cells. The matrix configuration for this example without fracture consideration is shown in Figure 4.15 representing typical grid connectivity. For a conventional grid domain, the

connectivity matrix is a bounded matrix with five and seven non-zero diagonals in 2D and 3D problems, respectively. However, inserting a fracture into the matrix domain will introduce additional connections between gridblocks. Hence, defining the matrix-fracture connections would alter the whole configuration and the structure of the connectivity matrix.

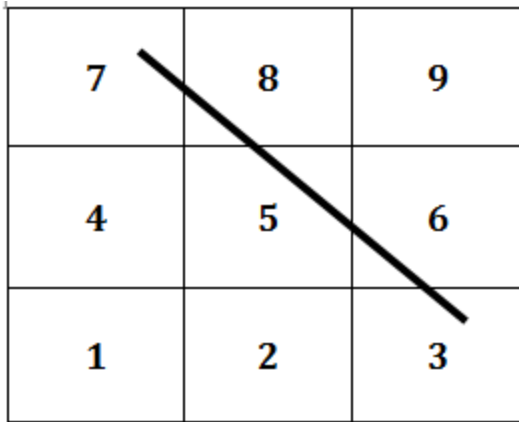


Figure 4.14: A  $3 \times 3$  grid with a single fracture to illustrate the NNC concept.

	1	2	3	4	5	6	7	8	9
1	X	X	0	X	0	0	0	0	0
2	X	X	X	0	X	0	0	0	0
3	0	X	X	0	0	0	X	0	0
4	X	0	0	X	X	0	X	0	0
5	0	X	0	X	X	X	0	X	0
6	0	0	X	0	X	X	0	0	X
7	0	0	0	X	0	0	X	X	0
8	0	0	0	0	X	0	X	X	X
9	0	0	0	0	0	X	0	X	X

Figure 4.15: The connectivity matrix for a  $3 \times 3$  grid without fracture consideration.

In the subsequent sections, to model a fractured domain and the corresponding computational grid, three approaches are discussed and several patterns of non-neighboring connections are presented. Moreover, the pros and cons of these methods are investigated in terms of models accuracy, computational cost, and requirements for the new parameters.

#### 4.4.1 Method I

As the simplest approach, by considering the fracture as a line in the 2D grid, we can assume that the fracture connects the gridblocks containing the head and the tail of the fracture line. For instance, in Figure 4.14, gridblocks number 3 and 7 are connected although they are not adjacent to each other (NNC). This non-neighboring connection is shown in red in the connectivity matrix (Figure 4.16). However, in this approach, the effect of gridblocks intersected by the rest of the fracture is neglected. In other words, the fracture is modeled as an open pipe with sealed walls with no communication with the matrix domain unless through the inlet and the outlet. In fact, this assumption is acceptable for modeling the breakthrough time of an injected fluid (such as water) in a fractured reservoir. When the injected fluid enters a fracture, because of the high conductivity of the fracture compared to the surrounding rock, it does not leave the fracture unless at the fracture tip due to high pressure gradient. Thus, it is valid to assume that fracture connects only two gridblocks.

Moreover, in this approach, the fluid exchange between the gridblocks number 3 and 7 is considered to be instantaneous in which the fluid travelling time in the fracture is neglected. Due to very high permeability of the fracture compared to the rock matrix, the fluid front movement in fracture is much faster than in the matrix domain. Therefore, in

low density fractured reservoirs in which the fluid movement is mostly governed by the rock matrix, the fluid travelling time in the fracture can be skipped.

	1	2	3	4	5	6	7	8	9
1	X	X	0	X	0	0	0	0	0
2	X	X	X	0	X	0	0	0	0
3	0	X	X	0	0	X	X	0	0
4	X	0	0	X	X	0	X	0	0
5	0	X	0	X	X	X	0	X	0
6	0	0	X	0	X	X	0	0	X
7	0	0	X	X	0	0	X	X	0
8	0	0	0	0	X	0	X	X	X
9	0	0	0	0	0	X	0	X	X

Figure 4.16: The connectivity matrix in Method I for the  $3\times 3$  grid with a single fracture.

In this method the transmissibility factor between non-neighboring gridblocks (i.e.  $T_{3-7}$ ) is calculated using the harmonic average of the transmissibility factors for the matrix-fracture intersections (i.e.  $T_{3-f}$  and  $T_{7-f}$ ) as presented in Eq. (4.16). The transmissibility factors for matrix-fracture intersections are computed using Eq. (4.7).

$$T_{3-7} = \frac{T_{3-f} T_{7-f}}{T_{3-f} + T_{7-f}}. \quad (4.16)$$

#### 4.4.2 Method II

In this approach, the fracture connects all the intersected gridblocks and the fluid exchange occurs between every pair of the intersected cells. This method provides a more realistic modeling approach compared to Method I in which two gridblocks were only connected. In fact, in Method II, the fracture represents a highly conductive pathway that communicates to the surrounding matrix at every point due to potential difference. However, similar to the previous method, the fluid transport through the fracture itself is neglected and the mass conservation equation is only solved for the matrix domain.

As shown in Figure 4.17, the connectivity matrix in Method II has more non-zero elements compared to Method I. In fact, by increasing the number of fractures, the connectivity matrix tends to be more like a full matrix rather than a sparse matrix. The connectivity matrix is similar to the pressure matrix in terms of the number and the location of non-zero elements which needs to be inverted over every time step of the simulation.

	1	2	3	4	5	6	7	8	9
1	X	X	0	X	0	0	0	0	0
2	X	X	X	0	X	0	0	0	0
3	0	X	X	0	X	X	X	X	0
4	X	0	0	X	X	0	X	0	0
5	0	X	X	X	X	X	X	X	0
6	0	0	X	0	X	X	X	X	X
7	0	0	X	X	X	X	X	X	0
8	0	0	X	0	X	X	X	X	X
9	0	0	0	0	0	X	0	X	X

Figure 4.17: The connectivity matrix in Method II for the  $3 \times 3$  grid with a single fracture.

In terms of transmissibility factors, Eq. (4.16) is applied again for every pair of the **matrix gridblocks intersected by the same fracture**. Based on Figure 4.17, we need to add 10 new transmissibility factors between gridblocks number 3, 5, 6, 7, and 8. Although a number of these gridblocks are already neighbors in the computational domain, the existence of fracture in these gridblocks alters the previous connections.

#### 4.4.3 Method III (EDFM)

If we choose EDFM to model the mentioned fractured reservoir model, unlike the previous approaches, the fracture needs to be discretized into several control-volumes (or cells) based on the intersection of the fracture line and the grid system. Then, the new cells are added to the computational domain through non-neighboring connections, and the connectivity matrix is modified. This method was discussed in detail in the preceding sections.

To simply illustrate the NNC concept in EDFM approach, Figure 4.18 presents the previous grid domain with the discretized fracture. In this figure, the fracture is cut into 5 new cells numbered from 10 to 14. Each of these new elements is connected to the surrounding matrix blocks and the adjacent fracture cells. Consequently, the connectivity matrix needs to be enhanced to account for these new communications (Figure 4.19). In this example, the size of the connectivity matrix increases to  $14 \times 14$  and the matrix becomes sparser.

The EDFM approach, not only takes into account all the possible connections, but also provides a tool to evaluate the fluid flow in the fracture itself. In some type of fractured reservoirs, due to high density of the natural fractures, the fluid transport is mainly governed by the fracture system. Thus, evaluation of various fracture parameters

using this method leads to better understanding of the flow in such reservoirs. However, using Methods I & II, the significance of the fracture is ignored. So, in terms of modeling accuracy, the EDFM approach provides better capabilities to study flow in fractured reservoirs.

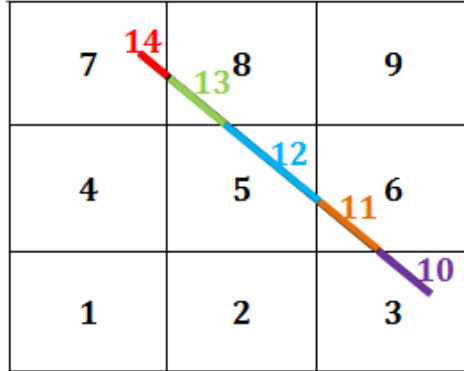


Figure 4.18: The  $3 \times 3$  grid with a single fracture to illustrate the EDFM approach. The fracture is cut into 5 pieces with respect to the intersections with matrix gridblocks.

Although more accurate compared to other NNC methods, EDFM requires more computational time. In every time step of simulation, a system of linear equations is solved to calculate pressure for every cell in the computational domain, including the fracture cells. This system is solved in the form of a matrix equation. The size of the matrix equation is equal to the size of the connectivity matrix, which is proportional to the number of cells in the simulation. Hence, by increasing the number of cells or control-volumes, more effort is required to solve the linear matrix equation. In other words, EDFM is computationally more expensive because in this method, the fracture planes are discretized and the created cells are added to the computational domain. Also, unlike the conventional simulation problems, the connectivity matrix is not banded

anymore, which eliminates a number of the candidate solvers for solving such systems. Using a robust and efficient solver can significantly decrease the required time for this type of calculations.

	1	2	3	4	5	6	7	8	9	10	11	12	13	14
1	X	X	0	X	0	0	0	0	0	0	0	0	0	0
2	X	X	X	0	X	0	0	0	0	0	0	0	0	0
3	0	X	X	0	0	X	0	0	0	X	0	0	0	0
4	X	0	0	X	X	0	X	0	0	0	0	0	0	0
5	0	X	0	X	X	X	0	X	0	0	0	X	0	0
6	0	0	X	0	X	X	0	0	X	0	X	0	0	0
7	0	0	0	X	0	0	X	X	0	0	0	0	0	X
8	0	0	0	0	X	0	X	X	X	0	0	0	X	0
9	0	0	0	0	0	X	0	X	X	0	0	0	0	0
10	0	0	0	X	0	0	0	0	0	X	X	0	0	0
11	0	0	0	0	0	X	0	0	0	X	X	X	0	0
12	0	0	0	0	X	0	0	0	0	0	X	X	X	0
13	0	0	0	0	0	0	X	0	0	0	X	X	X	0
14	0	0	0	0	0	0	X	0	0	0	0	X	X	0

Figure 4.19: The connectivity matrix in Method III (EDFM) for the  $3 \times 3$  grid with a single fracture. The dotted lines show the limits of the connectivity matrix for the non-fractured reservoir model.

The matrix and fracture cells communications need to be quantified to determine the fluid transfer between cells and solve for pressure and transport equations. While EDFM gives a systematic approach to compute the connection between cells (through definition of modified transmissibility factors), Methods I & II fail to introduce such calculations. However, based on the methodology used in EDFM, a technique was proposed to calculate the transmissibility factors for Methods I and II as well (Eq. (4.16)).

To investigate the performance of fractured reservoirs, in-depth analysis of fluid flow in complex fracture domain is crucial. In order to develop a comprehensive reservoir simulator to model fractured reservoirs, the EDFM (method III of NNC approaches) has been specified as the most accurate and convenient approach to add to UTCOMP and UTGEL reservoir simulators. In the subsequent section, the methodology and the principal modifications of the formulation are presented to handle non-neighboring connections.

#### 4.5 MODIFIED RESERVOIR SIMULATORS FORMULATIONS

A novel methodology is proposed to employ EDFM in UTCOMP and UTGEL reservoir simulators, in which extra directions (rather than X-, Y-, and Z-directions) are added to account for non-neighboring connections. As it was shown in Figure 4.13, in a typical three-dimensional problem, each gridblock at maximum is connected to six other gridblocks. However, if the block is intersected by a fracture plane, an extra direction is required to calculate the fluid transfer between matrix and fracture cell. To illustrate a schematic of this concept, consider a matrix gridblock intersected by two different fracture planes; therefore, as explained previously for EDFM approach, two fracture cells are bounded inside this specific block (Figure 4.20a). At every time step in the simulation, mass transfer happens between this block and the two fracture cells as well as six neighboring matrix gridblocks. Thus, in mass balance equation, two extra directions must be included to capture matrix-fracture communications (Figure 4.20b). As a result, in this example, eight directions exist for this specific gridblock overall.

Likewise, for all the fracture cells, this method is applied to implement non-neighboring connections. The only difference is that for fracture cells there is no

neighboring cells and all the fluid transfer is through the NNC's. Even for neighboring fracture segments of the same fracture plane, the connections are treated as NNCs. Figure 4.21 shows a schematic of a fracture cell confined in a matrix block and the corresponding directions for mass balance calculations. One point to mention is that every fracture cell is only connected to one matrix block, while a matrix block can be connected to as many as fracture cells.

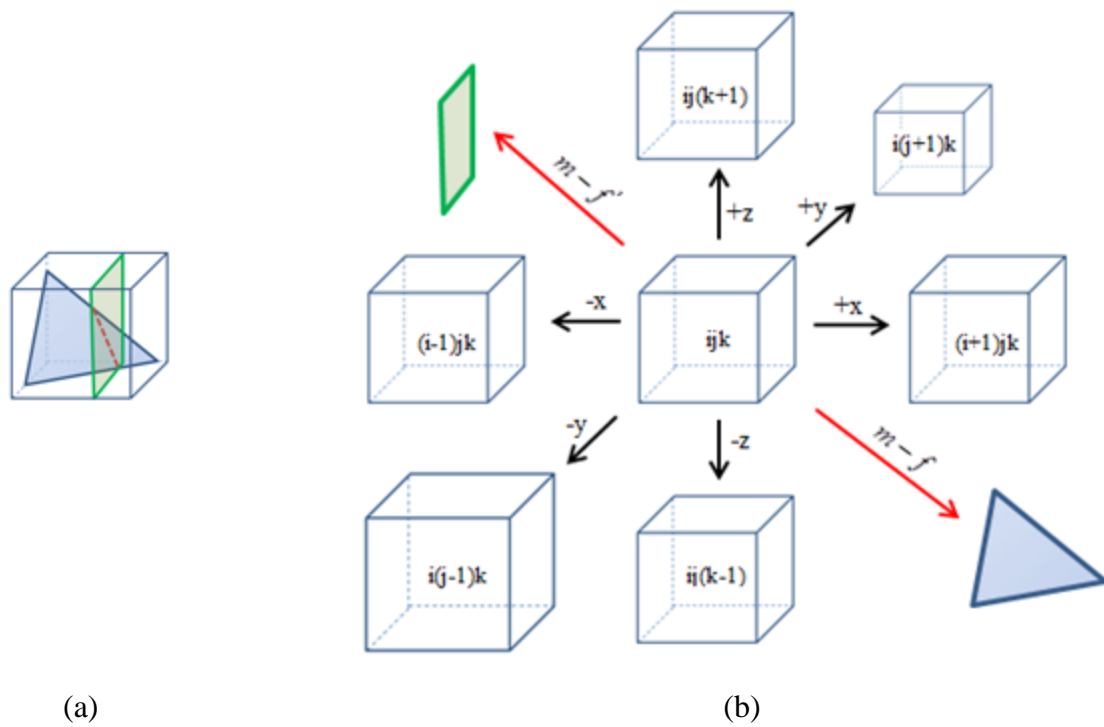


Figure 4.20: In EDFM approach (a) a gridblock that is intersected by two fracture planes has a total of (b) eight connections. The red arrows show the non-neighboring connections between the matrix block “ $ijk$ ” and the fracture segments confined inside the block.

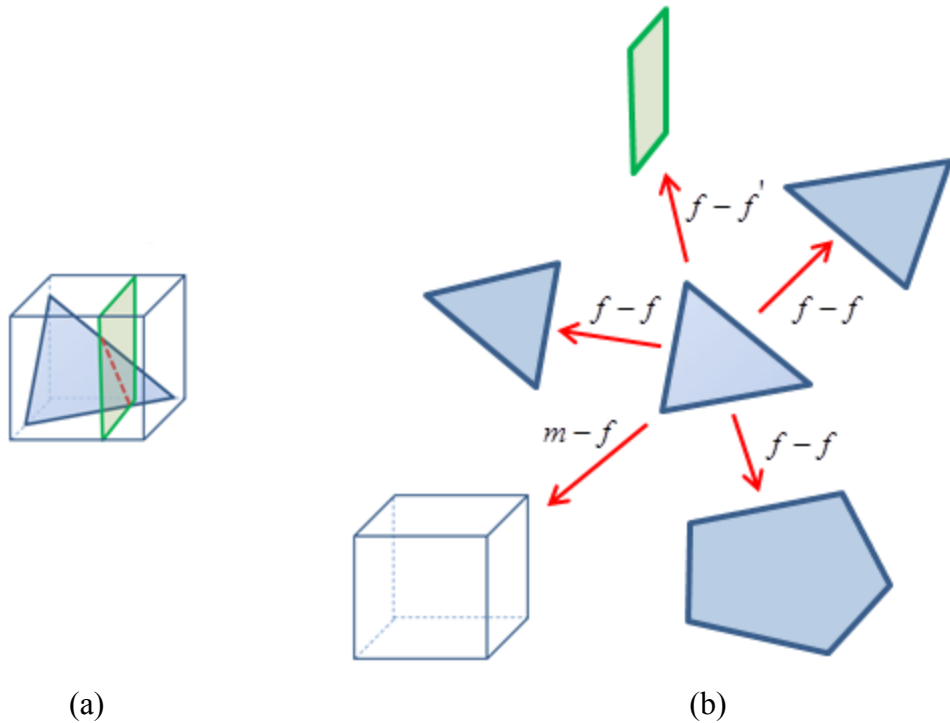


Figure 4.21: In EDFM approach, all the connections of a fracture cell are treated as non-neighboring connections. In this example, (a) a gridblock is intersected by two different fracture planes  $f$  and  $f'$ . (b) Hence, the blue fracture cell is connected to one matrix gridblock, one fracture cell from other plane (green plane), and three neighboring cells of the same fracture plane.

Since non-neighboring connections are modeled as the extra directions for fluid flow, all the parameters and operators that are somehow a function of direction must be modified. In general, operators such as divergence  $\bar{\nabla} \cdot$  and gradient  $\nabla$  calculate a form of derivative of a desired function with respect to each direction. If we assume that  $F$  is a three-dimensional vector function with components  $F_x$ ,  $F_y$ , and  $F_z$  in the corresponding directions, and  $g$  is a scalar function, then the definition of divergence and gradient are as follows, respectively.

$$\vec{\nabla} \bullet \mathbf{F} = \frac{\partial F_x}{\partial x} + \frac{\partial F_y}{\partial y} + \frac{\partial F_z}{\partial z}. \quad (4.17)$$

$$\nabla f = \frac{\partial f}{\partial x} i + \frac{\partial f}{\partial y} j + \frac{\partial f}{\partial z} k. \quad (4.18)$$

However, for the matrix gridblocks intersected by fracture planes, the above equations are not adequate anymore, because they do not include the fluid transfer between the matrix gridblocks and the corresponding fracture cells. To solve this issue for non-neighboring connections, extra terms are added to these equations. The number of these extra terms is equal to the number of non-neighboring connections for every cell (including both matrix and fracture cells). Eqs. (4.19) and (4.20) show the modifications made to the previous equations, where  $N_{nnc}$  is the number of non-neighboring connections for every control-volume in the computational domain and  $f_i$  is the  $i$ -th direction of NNCs.

$$\vec{\nabla} \bullet \mathbf{F} = \frac{\partial F_x}{\partial x} + \frac{\partial F_y}{\partial y} + \frac{\partial F_z}{\partial z} + \sum_{i=1}^{N_{nnc}} \frac{\partial F_{f_i}}{\partial f_i}. \quad (4.19)$$

$$\nabla f = \frac{\partial f}{\partial x} \vec{i} + \frac{\partial f}{\partial y} \vec{j} + \frac{\partial f}{\partial z} \vec{k} + \sum_{i=1}^{N_{nnc}} \frac{\partial f}{\partial f_i} \vec{f}_i. \quad (4.20)$$

For fracture cells, the same formulations are applied without the terms in X-, Y-, and Z-directions, because all of the connections for fracture cells are accounted as NNC.

In addition to the above operators, calculation of a number of parameters is a function of direction as well. When pressure and mass balance PDEs are discretized using

a numerical method, a number of properties are calculated at the interface between two adjacent gridblocks. These properties are called block-face or inter-block properties. To compute the value of the inter-block properties, several averaging techniques have been proposed which consist of values of that property in the neighboring cells with different weighting factors. However, to increase the stability of the numerical solution, an appropriate averaging method must be selected. Although, higher-order methods are available in UTCOMP and UTGEL, the one-point upstream weighting (upwind weighting) is considered for the approximation of inter-block properties for matrix-fracture or in general non-neighboring connections. To do so, Eqs. (4.21a) and (4.21b) are applied based on the phase potential in the adjacent cells. For example, suppose  $X$  is an inter-block property between a matrix block and a fracture cell, then the approximated value for  $X$  would be its value at the upstream cell. This process is repeated for all the other directions of NNCs. In pressure and mass conservation equations, the properties that are treated in this way are: molar density of phase  $j$  ( $\xi_j$ ), mole fraction of component  $i$  in phase  $j$  ( $x_{ij}$ ), and relative mobility of phase  $j$  ( $\lambda_{nj}$ ) for the UTCOMP simulator, and volume concentration of component  $\kappa$  in phase  $l$  ( $C_{\kappa l}$ ), and relative mobility of phase  $l$  ( $\lambda_{rl}$ ) for the UTGEL simulator.

$$X_{m-f} = X_m \quad \text{if} \quad \Phi_m > \Phi_f. \quad (4.21a)$$

$$X_{m-f} = X_f \quad \text{if} \quad \Phi_f > \Phi_m. \quad (4.21b)$$

To develop the final form of the governing equations, we neglect the dispersion term. Also, we assume that the process is isothermal and therefore there is no need to solve the energy balance equation. If we apply these simplifications, we obtain the

following pressure and mass balance equations for UTCOMP-EDFM and UTGEL-EDFM simulators (Eqs. (4.22) to (4.25)). Since index notations are used in these equations, no difference is observed compared to the original equations described in the previous chapter. However, as mentioned above, several modifications are necessary to derive the inter-block properties and also to expand the mathematical operators. To highlight these changes, the block-face properties and the operators are shown in blue and red, respectively, in the following equations.

UTCOMP-EDFM Simulator:

$$\frac{\partial \left( \phi \sum_{j=1}^{n_p} \zeta_j S_j x_{ij} \right)}{\partial t} - \vec{\nabla} \cdot \left[ \sum_{j=1}^{n_p} \zeta_j \lambda_j x_{ij} (\nabla P_j - \gamma_j \nabla D) \right] - \frac{q_i}{V_b} = 0 \quad (4.22)$$

*for  $i = 1, 2, \dots, n_c$ .*

$$\begin{aligned} & \left( V_P^0 c_f - \frac{\partial V_t}{\partial P} \right) \left( \frac{\partial P}{\partial t} \right) - V_b \sum_{i=1}^{n_c+1} \vec{V}_{ti} \vec{\nabla} \cdot \sum_{j=1}^{n_p} \vec{k} \lambda_{rj} \xi_j x_{ij} \\ &= V_b \sum_{i=1}^{n_c+1} \vec{V}_{ti} \vec{\nabla} \cdot \sum_{j=1}^{n_p} \vec{k} \lambda_{rj} \xi_j x_{ij} (\nabla P_{c2j} - \gamma_j \nabla D). \end{aligned} \quad (4.23)$$

UTGEL-EDFM Simulator:

$$\frac{\partial \left( \phi \left( \left( 1 - \sum_{\kappa=1}^{n_{CV}} \hat{C}_{\kappa} \right) \sum_{l=1}^{n_p} S_l \mathbf{C}_{kl} + \hat{C}_{\kappa} \right) \rho_{\kappa} \right)}{\partial t} - \vec{\nabla} \cdot \left[ \sum_{l=1}^{n_p} \rho_{\kappa} \mathbf{C}_{kl} \lambda_l (\nabla P_l - \gamma_l \nabla h) \right] = R_{\kappa}$$

for  $\kappa = 1 \dots n_c$ .

(4.24)

$$\phi C_t \frac{\partial P_1}{\partial t} - \vec{\nabla} \cdot \vec{k} \lambda_{rTc} \vec{\nabla} P_1 = - \vec{\nabla} \cdot \sum_{l=1}^{n_p} \vec{k} \lambda_{rlc} \nabla h + \vec{\nabla} \cdot \sum_{l=1}^{n_p} \vec{k} \lambda_{rlc} \nabla P_{cl1} + \sum_{\kappa=1}^{n_{CV}} Q_{\kappa}.$$

(4.25)

## Chapter 5: Model Verification

In every reservoir simulation development project, the step after modeling (or deriving the mathematical formulation) and implementation (or coding) is the verification. To examine the accuracy and robustness of new models or tools, verification against existing numerical or analytical solutions is an essential task. Although it is impossible to cross-check the model with all the available examples, testing against general and more technical problems is very important.

In this chapter, the implemented EDFM approach in UTCOMP and UTGEL reservoir simulators is compared against a few numerical simulation problems as well as one semi-analytical solution. To start with, the EDFM result is compared against a fine-grid simulation problem with simple fractures. For cases with more complex fracture geometries and configurations, two examples from Moinfar (2013) are selected. Finally, to check the accuracy of model in well-fracture intersection, with application in studying hydraulic fractures, the results are compared against a semi-analytical solution of the diffusion equation, developed by Zhou *et al.* (2014) and Wei *et al.* (2014).

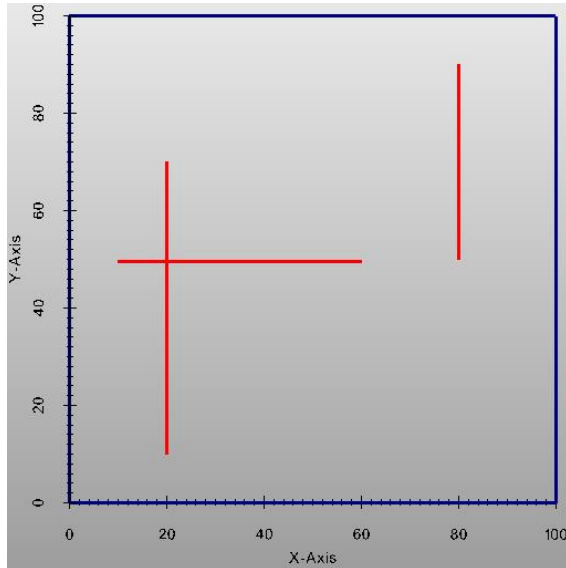
### 5.1 FINE-GRID SIMULATION

As the first case for verification, a 2D reservoir model is specified with simple fracture planes. The EDFM results in UTCOMP and UTGEL are tested against the fine-grid simulation. To simply setup the reservoir model and to generate the fractures explicitly, a single size gridblock is used to construct the fine-grid model. Also, all the three fractures are set to be vertical and placed parallel to the reservoir boundaries to make gridding more straightforward. The reservoir model and the location of fractures

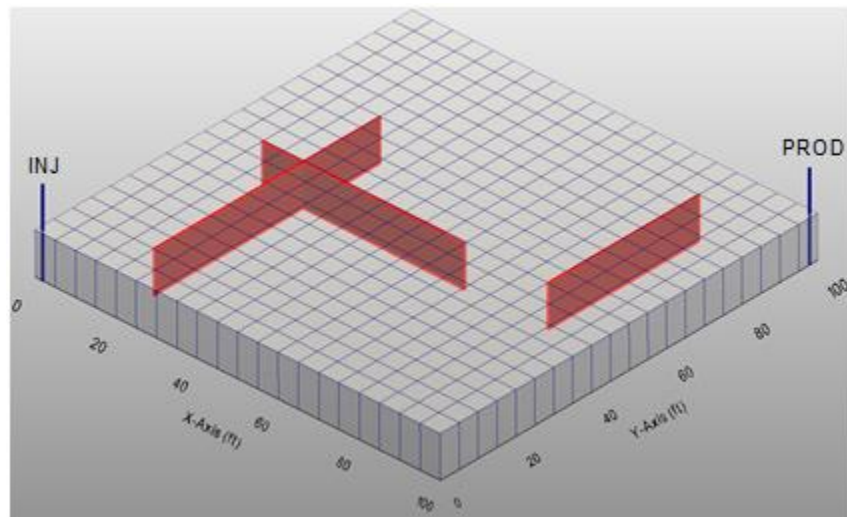
are shown in Figure 5.1(a). In this example, two of the fractures are intersected, whereas the other one is isolated. To study the grid sensitivity in EDFM approach, four cases with different gridblock sizes are constructed. The grid size and the dimensions of the gridblocks for all the cases are summarized in Table 5.1. As an illustration of EDFM setup, the reservoir model for the  $20 \times 20$  grid with the three fractures is shown in Figure 5.1(b). As a reminder, the fractures are embedded inside the matrix grid, and no grid refinement is performed close to the fractures. The injector is located at one corner injecting water at the rate of 0.5 STB/D, and the producer is at the opposite corner operating at constant BHP of 3000 psi. The hydrocarbon is single component ( $C_{10}H_{22}$ ) and the reservoir pressure is above the bubble point. Also, the capillary pressure effect is neglected in this example. The other reservoir rock and fluid properties are summarized in Table 5.2.

Figures 5.2 and 5.3 show the oil and water production rates for the reservoir model after 400 days. The EDFM approach is tested with different grid sizes:  $10 \times 10$ ,  $20 \times 20$ ,  $50 \times 50$ , and  $100 \times 100$ . As observed from the figures, the  $50 \times 50$  case achieves very similar results compared to the fine-grid simulation. However, if we compare the simulation run times, presented in Table 5.3, the EDFM- $50 \times 50$  case is faster than fine-grid model 113 and 123 times in UTCOMP and UTGEL simulators, respectively. This improvement would be even more significant for more complicated fracture networks. All of the simulation runs were performed using one processor of Petros cluster, which has 16 GB of memory on each computing node. This Linux cluster is owned by The Center for Petroleum and Geosystems Engineering (CPGE) at The University of Texas at Austin. Finally, to compare the water saturation profiles, Figure 5.4 indicates the water invasion maps after 96 and 168 days for the fine-grid and the EDFM approach in UTCOMP and UTGEL for the  $50 \times 50$  grid. Again, very good agreement is observed

between all the three models.



(a)



(b)

Figure 5.1: A reservoir model with 3 vertical fractures: (a) Map view of the reservoir and the location of fractures. (b) The  $20 \times 20$  grid used in the EDFM approach. The reservoir thickness has magnified 20 times for a better illustration.

	Fine-Grid	EDFM			
		Case 1	Case 2	Case 3	Case 4
Grid Size (x × y × z)	200×200×1	10×10×1	20×20×1	50×50×1	100×100×1
Gridblock Dimensions ( $\Delta x$ (ft) × $\Delta y$ (ft) × $\Delta z$ (ft))	0.5×0.5×0.5	10×10×0.5	5×5×0.5	2×2×0.5	1×1×0.5
Number of Fracture Cells	300	15	30	75	150

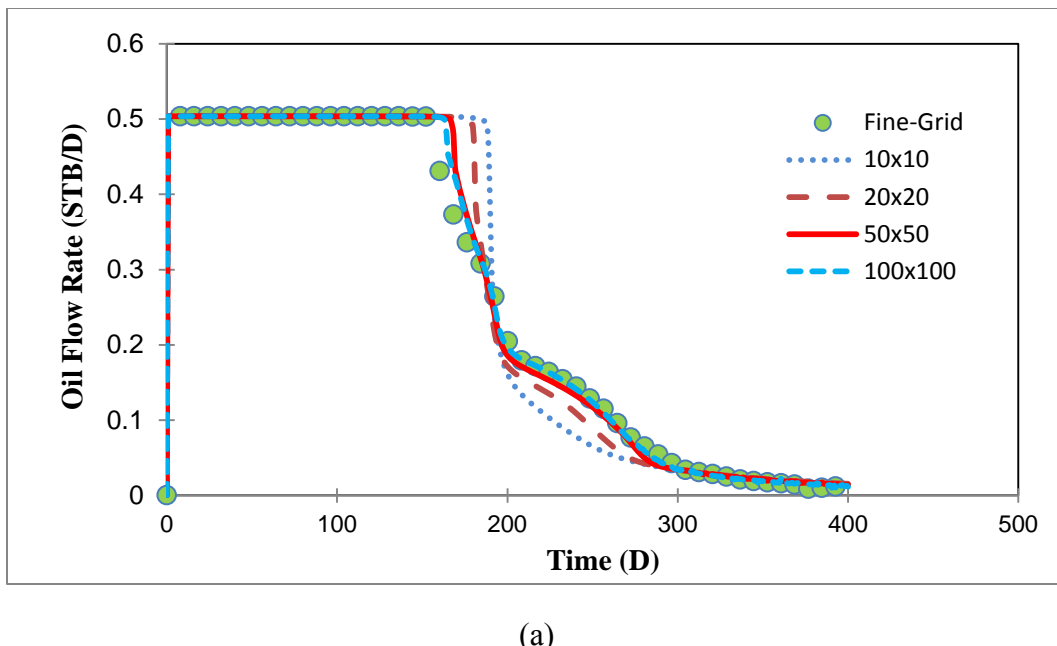
Table 5.1: Gridding information for the Fine-grid and EDFM simulations is presented in this table. Four different cases are considered for grid sensitivity.

Overall Properties		Relative Permeability Curves	
Matrix Porosity (fraction)	0.2	Irreducible Water Saturation	0.2
Matrix Permeability (md)	20	Water Rel. Perm. End Point	0.8
Fracture Permeability (md)	10000	Water Rel. Perm. Exponent	4
Fracture Aperture (ft)	0.5	Residual Oil Saturation	0.2
Initial Reservoir Pressure (psi)	3000	Oil Rel. Perm. End Point	0.7
Initial Water Saturation	0.2	Oil Rel. Perm. Exponent	2
Initial Oil Saturation	0.8	C <sub>10</sub> H <sub>22</sub> Properties	
Reservoir Temperature (°F)	60	Critical Pressure (psia)	350
Rock Compressibility (psi <sup>-1</sup> )	5.00E-06	Critical Temperature (°R)	1500
Fluid Compressibility (psi <sup>-1</sup> )	0	Molecular Weight (lb/lb-mole)	142.23
Well Properties		Parachor	
Well Radius (ft)	0.35	Acentric Factor	0.488
Producer BHP (psi)	3000	Water Viscosity (cp)	0.8
Injector Rate (STB/D)	0.5	Oil Viscosity (cp)	0.19

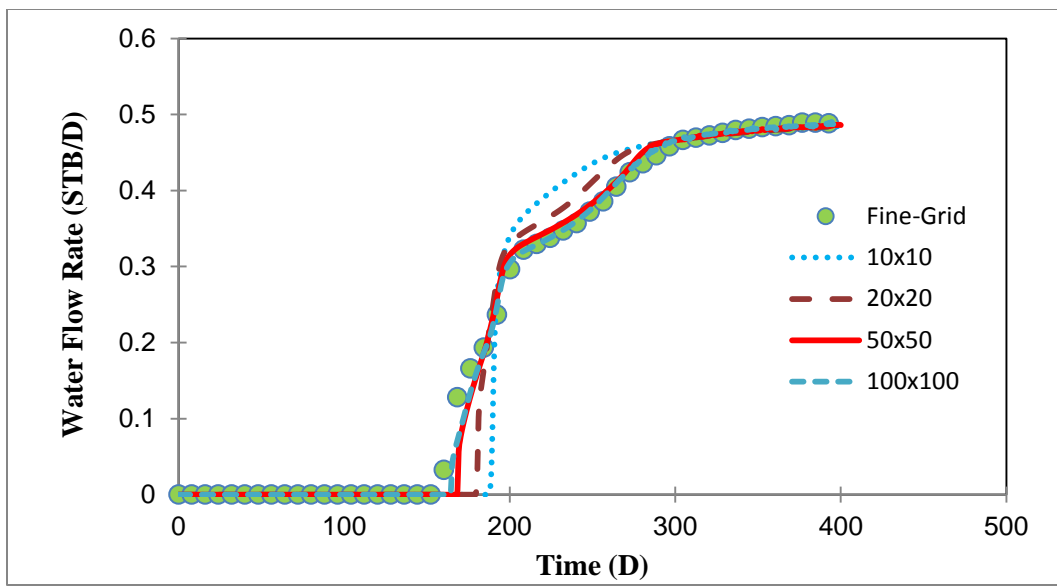
Table 5.2: Rock and fluid properties for the reservoir model in section 5.1

	Fine-Grid	UTCOMP-EDFM				UTGEL-EDFM			
		10×10	20×20	50×50	100×100	10×10	20×20	50×50	100×100
Simulation Time (minutes)	1071	0.08	0.47	9.48	108	0.05	0.42	8.7	110

Table 5.3: Simulation run times for the examples presented in section 5.1

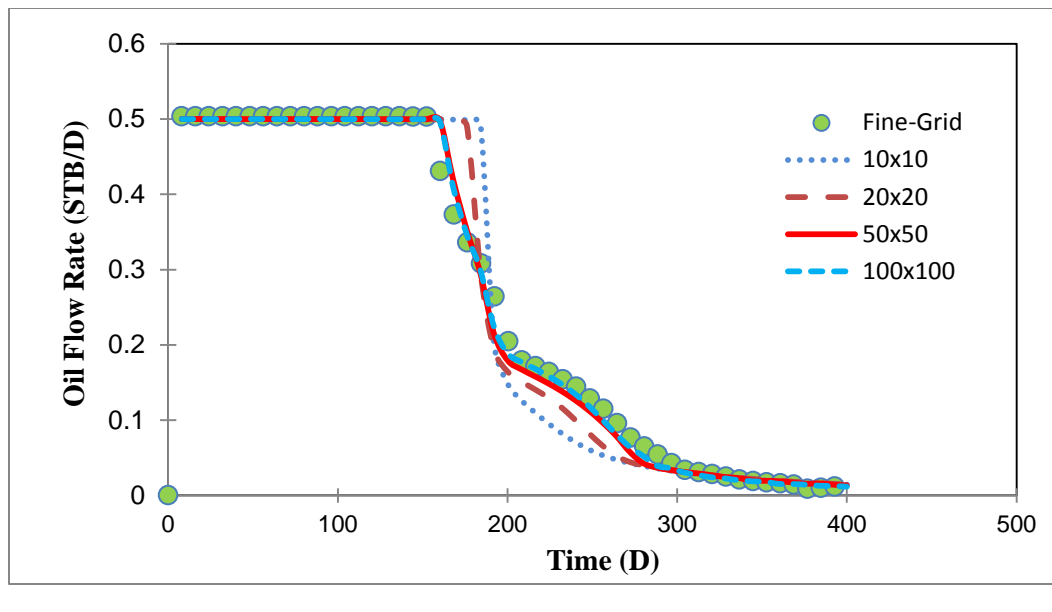


(a)

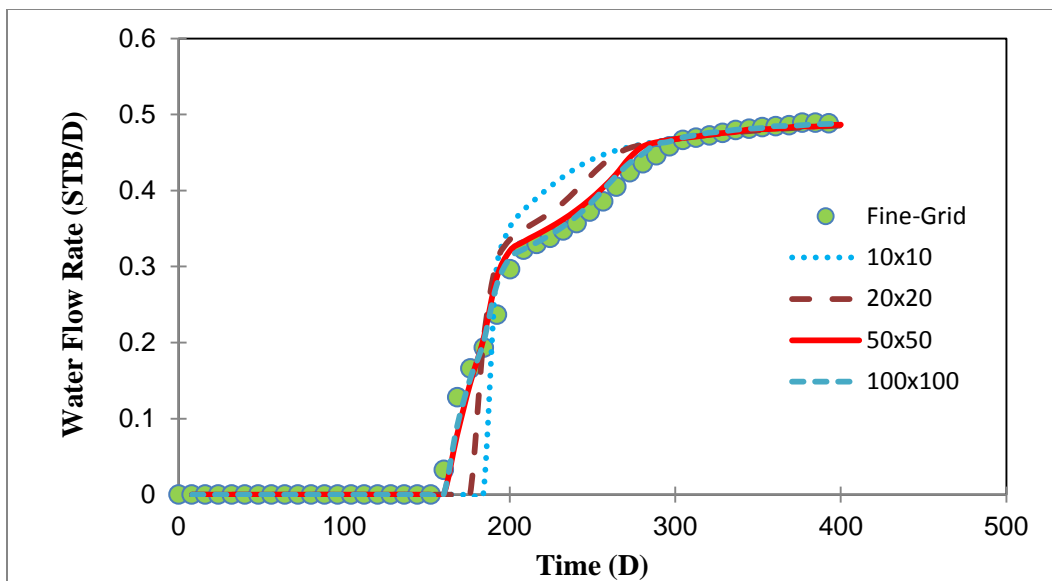


(b)

Figure 5.2: (a) Oil and (b) water production rates for UTCOMP-EDFM and the fine-grid models. Four cases with different gridblock sizes are considered for EDFM. The  $50 \times 50$  case is the optimum one.



(a)



(b)

Figure 5.3: (a) Oil and (b) water production rates for UTGEL-EDFM and the fine-grid models. Four cases with different gridblock sizes are considered for EDFM. The  $50 \times 50$  case is the optimum one.

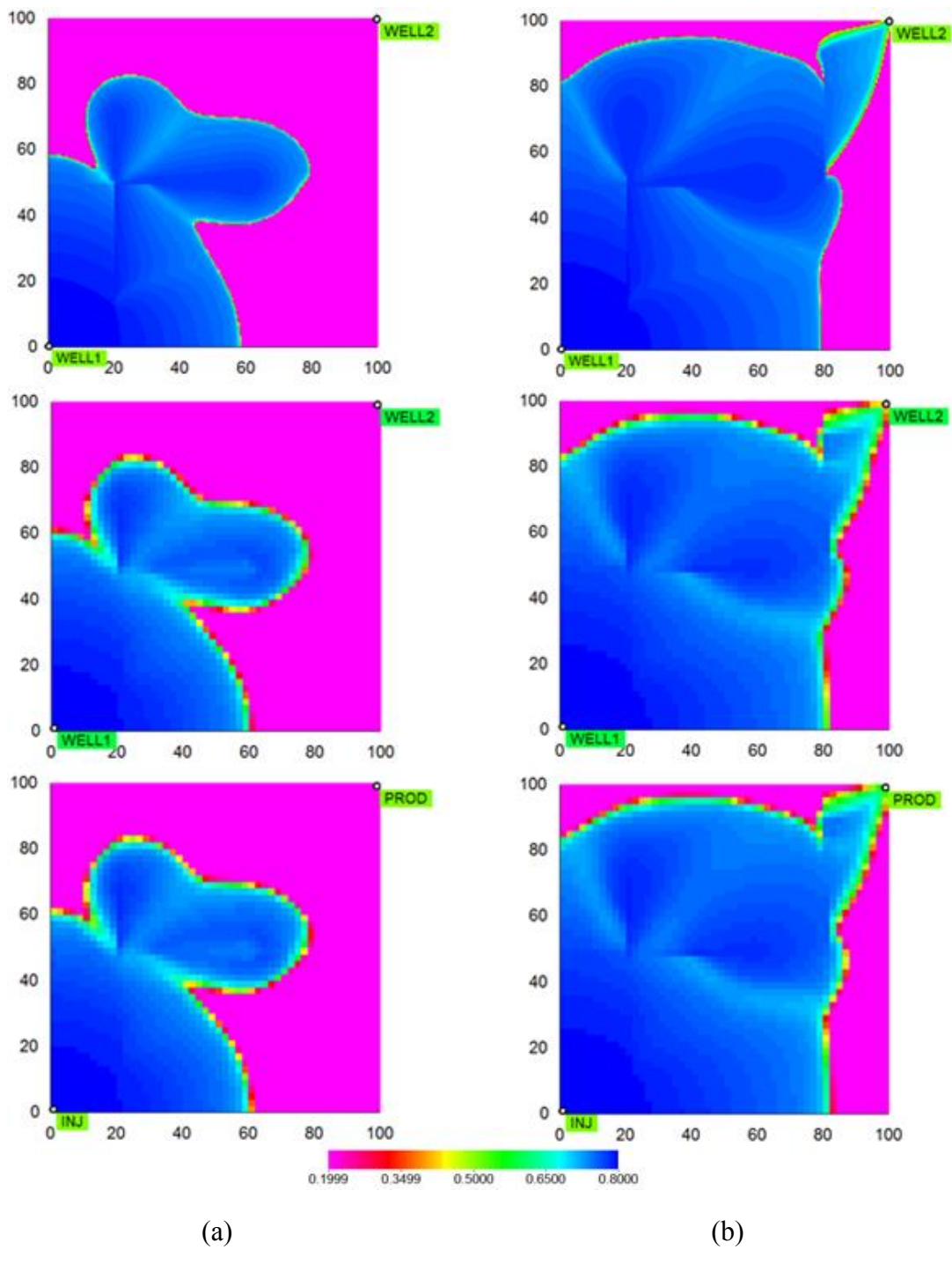
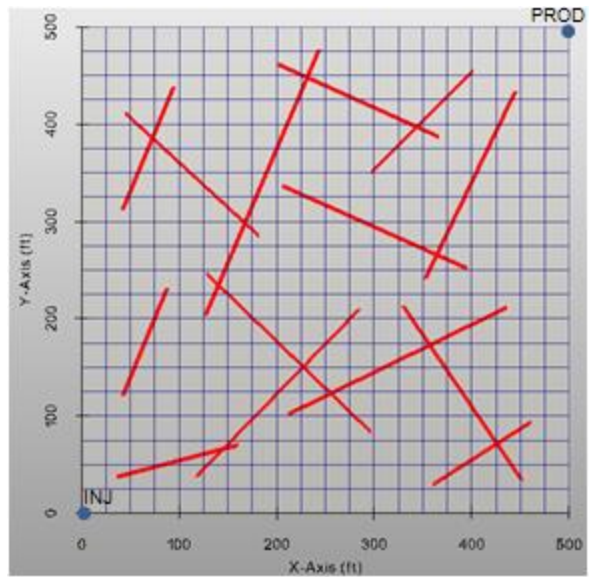


Figure 5.4: Water saturation profiles for the reservoir model after (a) 96 days (left column) and (b) 168 days (right column). The rows from top to bottom show the water saturation profiles for the fine-grid, UTCOMP-EDFM, and UTGEL-EDFM, respectively.

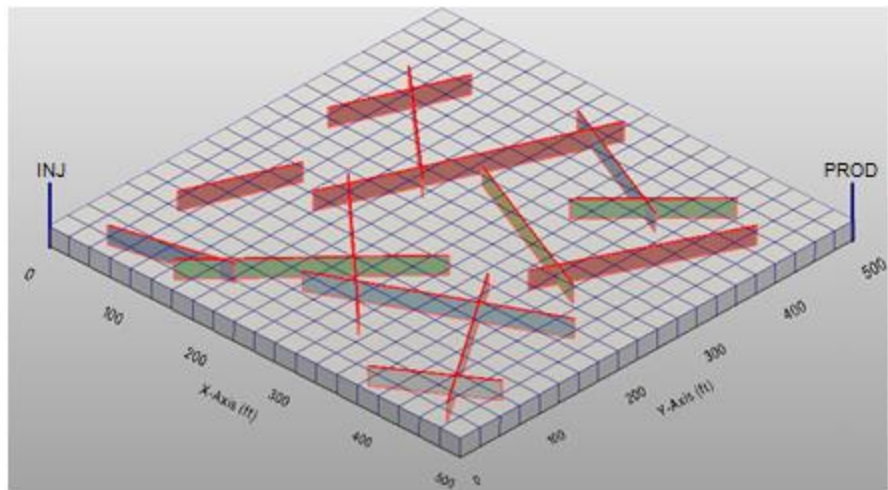
## 5.2 ARBITRARY ORIENTED FRACTURES

One of the main capabilities of EDFM approach is modeling fractures with arbitrary orientations and dip angles, which provides more degree of freedom in defining realistic and complex fracture networks. However, to verify these capabilities, the fine grid simulation is not applicable anymore. If not impossible, it would be very tedious to setup the fine-grid simulation for non-aligned dip-angled fractures, while it would be very simple for EDFM to do so. Thus, to validate the further applications of the implemented model in UTCOMP and UTGEL, the earlier development of EDFM in GPAS reservoir simulator is used. Moinfar (2013) carried out the similar project as part of his PhD work, and presented several examples of these kinds in his dissertation. In the current and the following section, UTCOMP-EDFM and UTGEL-EDFM are compared with two of the examples from Moinfar (2013).

Figure 5.5 illustrates a 2D reservoir model with 14 randomly oriented vertical fractures. These fractures or channels represent the naturally occurred fissures and openings in fractured reservoirs. In this example, the grid is  $20 \times 20 \times 1$  and the gridblock dimensions are 25, 25, and 20 ft in X-, Y-, and Z-directions, respectively. Due to discretization of the fracture planes with gridblock boundaries, an overall 156 fracture cells are created and added to the computational domain. Table 5.4 describes the matrix, fracture, and the fluid properties. In this case study, the water is injected at one corner at the rate of 100 STB/D and oil is produced at the opposite corner through the production well. One feature examined in this example is the variation of relative permeability curves between fracture and matrix domains. While the straight line curves are used for fracture cells, the relative permeability in matrix domain is computed with the Corey model based on the parameters given in Table 5.4. However, it is possible to choose other permeability curves for fractures as well.



(a)



(b)

Figure 5.5: A reservoir model with 14 vertical fractures with various orientations (from Moinfar (2013)). (a) Map view of the reservoir and the location of fractures (b) The  $20 \times 20$  grid used in the EDFM approach.

Overall Properties		Relative Permeability Curves for Matrix	
Matrix Porosity (fraction)	0.1	Irreducible Water Saturation	0.2
Matrix Permeability (md)	20	Water Rel. Perm. End Point	0.8
Fracture Permeability (md)	700000	Water Rel. Perm. Exponent	4
Fracture Aperture (ft)	0.025	Residual Oil Saturation	0.2
Initial Reservoir Pressure (psi)	3000	Oil Rel. Perm. End Point	0.7
Initial Water Saturation	0.2	Oil Rel. Perm. Exponent	2
Initial Oil Saturation	0.8	$C_{10}H_{22}$ Properties	
Reservoir Temperature ( $^{\circ}$ F)	60	Critical Pressure (psia)	350
Rock Compressibility ( $\text{psi}^{-1}$ )	0	Critical Temperature ( $^{\circ}$ R)	1500
Fluid Compressibility ( $\text{psi}^{-1}$ )	0	Molecular Weight (lb/lb-mole)	142.23
Well Properties		Parachor	431
Well Radius (ft)	0.5	Acentric Factor	0.488
Producer BHP (psi)	3000	Water Viscosity (cp)	0.8
Injector Rate (STB/D)	100	Oil Viscosity (cp)	0.19

Table 5.4: Rock and fluid properties for the reservoir model in section 5.2. The relative permeability curves are straight lines for the fractures.

Figure 5.6 compares the oil production rates of UTCOM-EDFM and UTGEL-EDFM simulations with the simulation data obtained from GPAS (Moinfar (2013)). As can be seen, there is an excellent agreement between the results which verifies the accuracy of the implementation for fractures with various orientations. Also, Figure 5.7 illustrates the water saturation profiles (invasion profiles) for all the three simulation cases after 150 and 250 days. Since the color bar distribution of the results shown from Moinfar (2013) is not identical with the one used for UTGEL outputs, the gridblocks with same saturations do not have matching colors. However, if you consider the saturation values for corresponding gridblocks, they are almost equal. Also, as observed from the figure, the invasion patterns are almost identical.

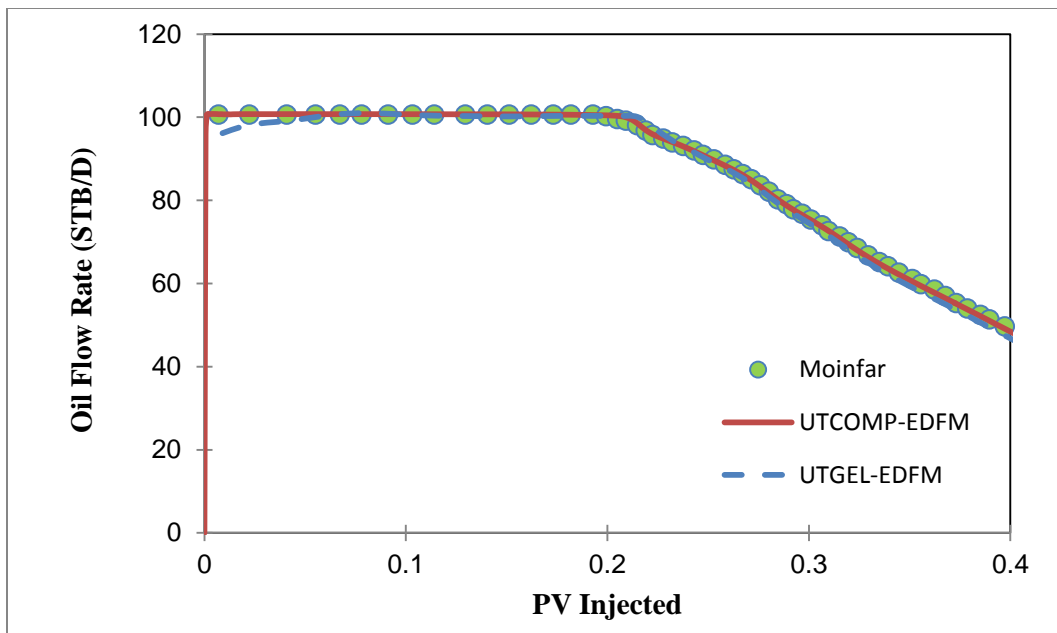


Figure 5.6: Comparison of oil production rates obtained from UTGEL-EDFM and UTCOMP-EDFM with Moinfar (2013) results for a 2D reservoir model with 14 fractures with various orientations.

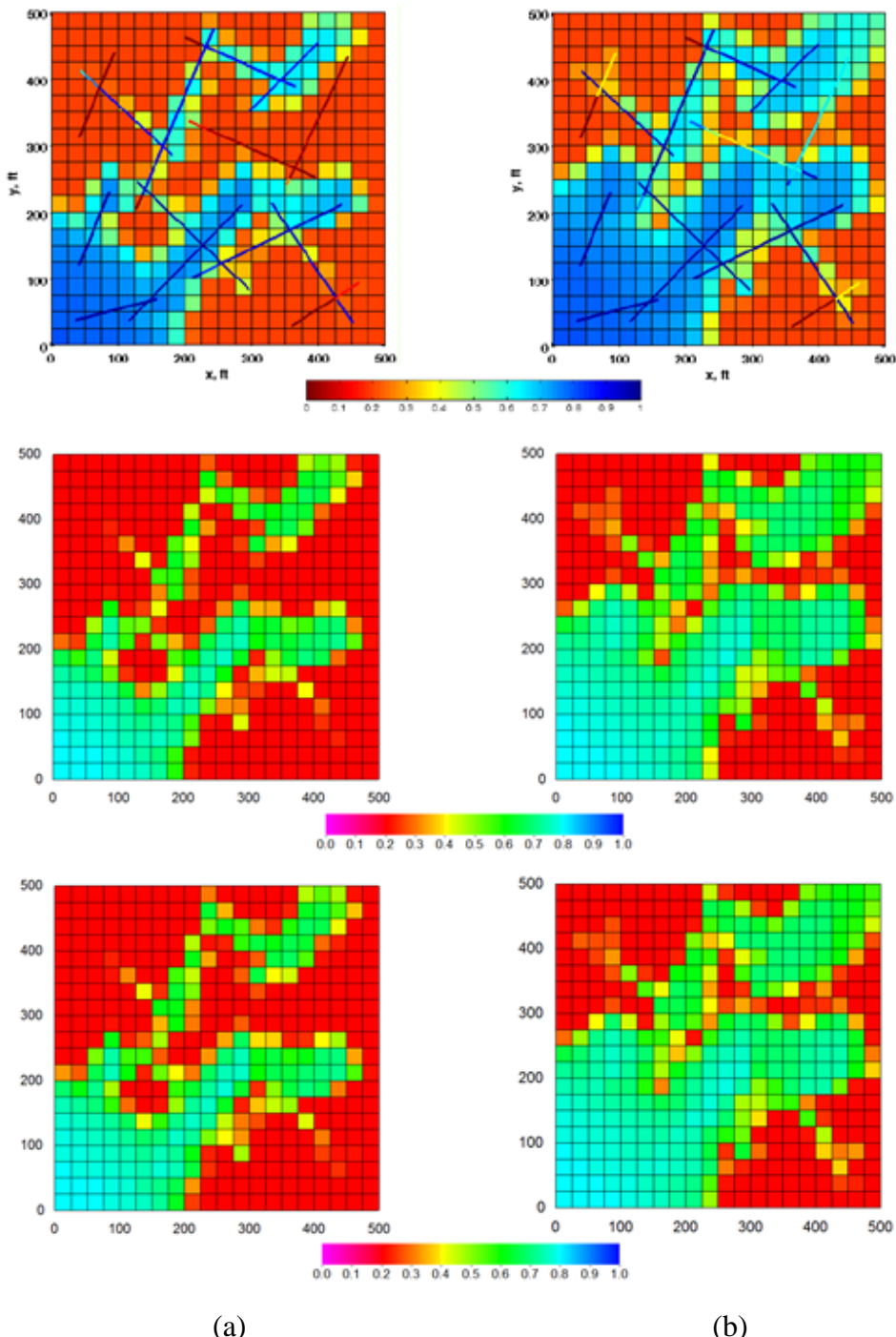


Figure 5.7: Water saturation profiles for the model reservoir after (a) 150 days (left column) and (b) 250 days (right column). The rows from top to bottom show the water saturation profiles for Moinfar (2013), UTCOMP-EDFM, and UTGEL-EDFM, respectively.

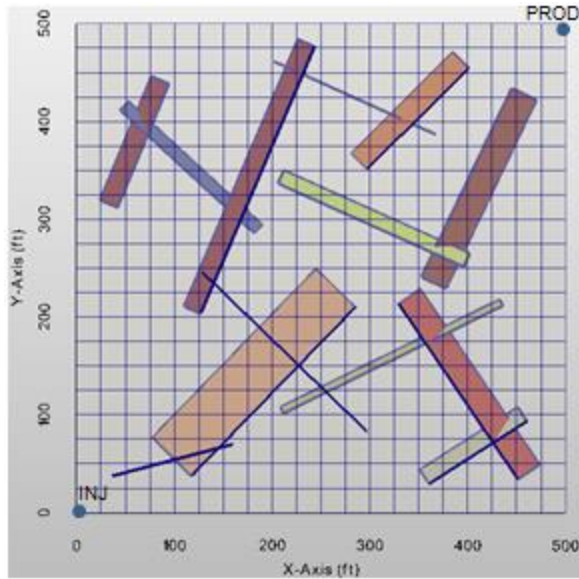
### **5.3 INCLINED FRACTURES**

After verification of fractures with various orientations, in this section we investigate the model accuracy for dip-angled fractures in a 3D reservoir model. Due to alteration of stress regimes with respect to depth, and tectonic movements, there is a high possibility for natural and induced fractures to propagate obliquely with respect to vertical direction. Although in most of the commercial simulators the study of inclined fractures is not allowed, EDFM approach provides this capability.

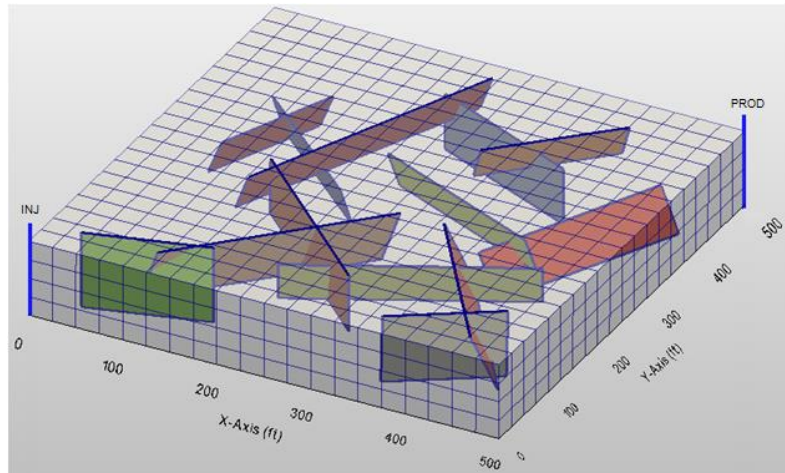
We use a 3D case study with 4 layers, from Moinfar (2013), to validate the simulators for inclined fractures. The reservoir model has 13 fractures with different dip angles ranging from 55 to 90 degrees. Figure 5.8 depicts the map and the slanted views of the reservoir and the location of the fractures. A number of the fractures have partially penetrated the reservoir and intersect only one or two layers. The matrix grid is  $20 \times 20 \times 4$  and 450 fracture cells are added to the computational domain due to fractures discretization. The water is injected at the rate of 1000 STB/D through the perforations in all the layers. The reservoir pressure as well as producer BHP is 5000 psi. Fractures permeability is 300,000 md, and matrix permeability is 15, 15, and 2 md in X-, Y-, and Z-directions, respectively. Straight line relative permeability curves with zero residual saturations are used for fractures, while Corey relative permeability model is applied for rock matrix. The rest of the rock and fluid properties are similar to those in Table 5.2.

Figure 5.9 compares the oil production rates obtained from UTCOMP-EDFM and UTGEL-EDFM with the same simulation result from Moinfar (2013). Based on the figure, a perfect agreement is observed between the results. Moreover, if we compare the water saturation profiles after 80 days for all the layers in Figure 5.10, again we can observe good agreement. Due to partial penetration and the effect of fractures in magnifying the gravity effects, the sweep patterns are different between the layers.

Although different color bars are reported for Moinfar results and our post processor, the invasion patterns and the saturation values of the corresponding gridblocks are identical.



(a)



(b)

Figure 5.8: A 3D reservoir model with 13 inclined fractures (from Moinfar (2013)). (a) Map view of the reservoir and the location of fractures. (b) The  $20 \times 20 \times 4$  grid used in the EDFM approach.

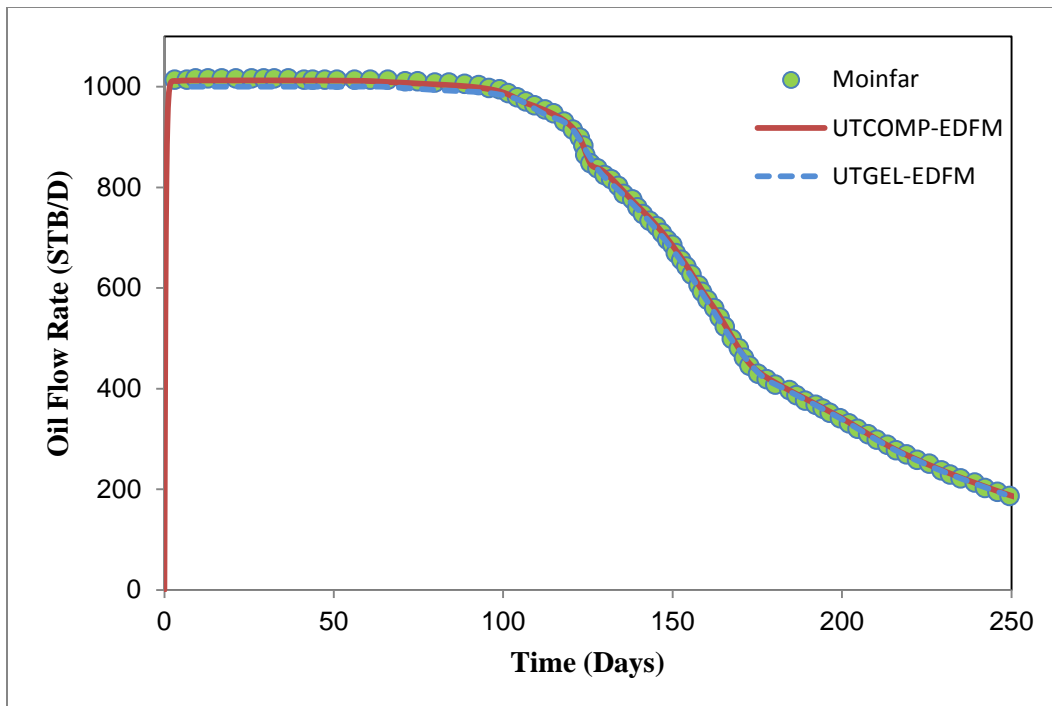


Figure 5.9: Comparison of oil production rates obtained from UTGEL-EDFM and UTCOMP-EDFM with Moinfar (2013) results for a 3D reservoir model with 13 inclined fractures.

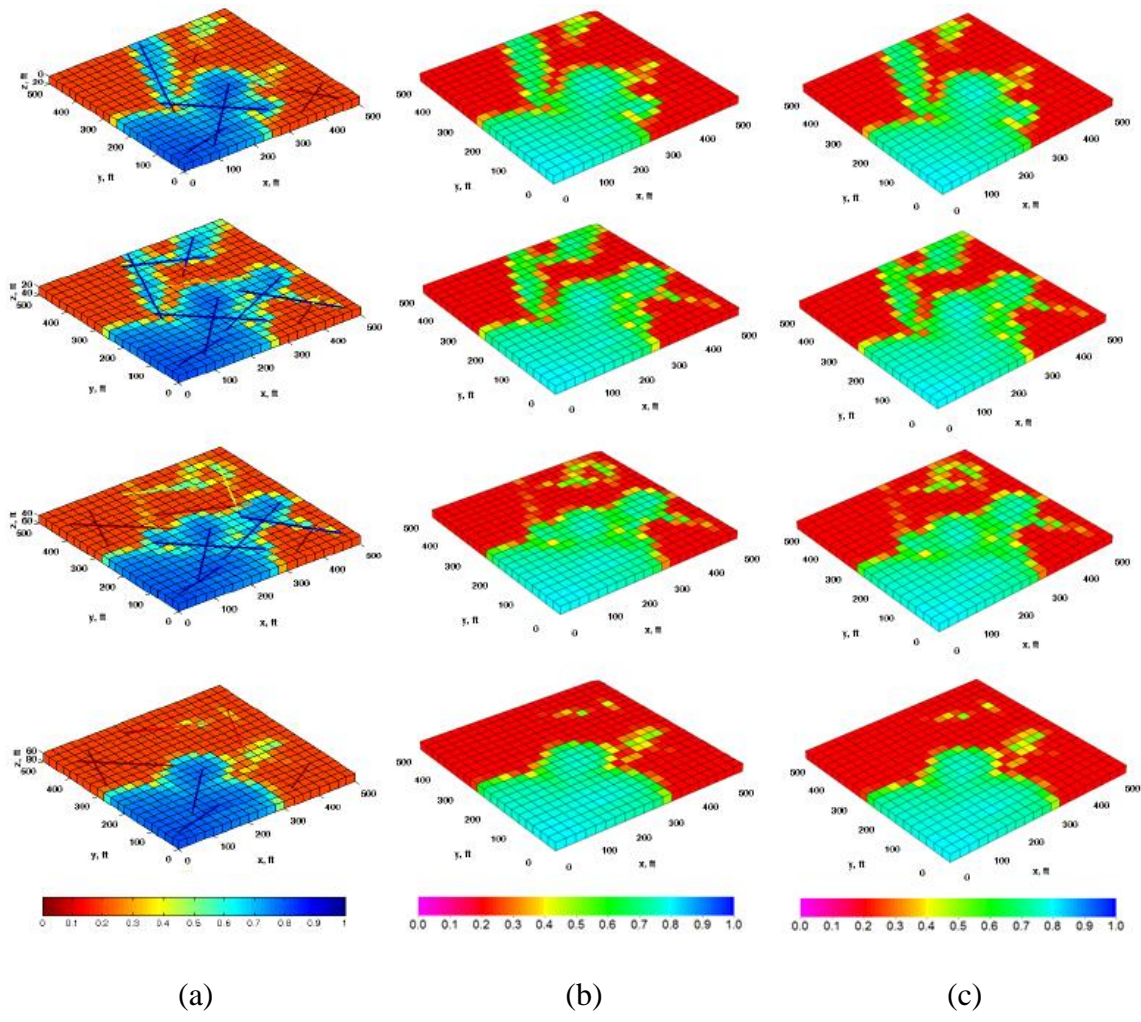


Figure 5.10: Water saturation profiles for (a) Moinfar (2013), (b) UTGEL-EDFM, and (c) UTGEL-EDFM after 80 days. In each column, saturation profiles are shown for the 4 layers, starting from the top layer at the top to the bottom layer at the bottom.

## 5.4 WELL-FRACTURE INTERSECTION (SEMI-ANALYTICAL SOLUTION)

Several analytical and semi-analytical solutions have been proposed in the petroleum literature (Chen and Raghavn (1997), Cinco-Ley *et al.* (1978)) to study the transient gas flow behavior in hydraulically fractured reservoirs. To develop such solutions, often simple geometries, such as bi-wing vertical fractures, are assumed for hydraulic fractures. However, a semi-analytical method has been developed recently by Zhou *et al.* (2014) to simulate more complex fracture networks. Based on this approach, pressure in every point in the reservoir is calculated based on an analytical solution of the diffusion equation and the superposition of pressure drawdowns with respect to each fracture panel. Fracture panels are considered as plane-sources. Consequently, Eq. (5.1) is derived for pressure at every point in the reservoir, where  $p(x, y, z, t)$  is pressure at point  $(x, y, z)$  and time  $t$ ,  $U(t - t_0)$  is Heaviside's unit step function,  $\phi$  is porosity,  $c_t$  is total compressibility,  $a$  is reservoir length,  $b$  is reservoir width,  $q_j$  is flux to fracture panel  $j$ ,  $N_p$  is the number of fracture panels, and  $G(x, y, z, t)$  is the instantaneous plane-source solution of the  $j$ -th fracture panel which is presented in the Appendix. The fractures are discretized into panels (Figure 5.11) and the mass balance equation combined with Darcy's law is numerically solved to find the rate in the fracture network. Eq. (5.2) represents the pressure at each fracture panel center where  $p_{j1}$  is pressure at the panels intersection,  $\mu$  is viscosity,  $k_f$  is fracture permeability,  $\rho$  is fluid density,  $b_f$  is fracture width,  $d$  is fracture thickness,  $q_{fj}$  is flux from matrix to fracture,  $q_{j1}$  is 1D flux along the fracture, and  $\beta$  is non-Darcy Forchheimer coefficient. In general, the reservoir is homogenous and the fluid is slightly compressible. The detailed information is found in Zhou *et al.* (2014) and Thambbynayagam (2011).

$$p(x, y, z, t) = \frac{U(t-t_0)}{4\phi c_t ab} \sum_{j=1}^{N_p} \int_0^t q_j(t-t_0-\tau) G_j(x, y, z, \tau) d\tau. \quad (5.1)$$

$$p_{jc} = p_{j1} - \int_{x_{j1}}^{x_{j2}} \left( \frac{\mu}{\rho k_f b_f d} \right)_j \left[ q_{j1} + q_{fj} (x - x_{j1}) \right] dx + \beta \rho \int_{x_{j1}}^{x_{j2}} \left\{ \frac{\left[ q_{j1} + q_{fj} (x - x_{j1}) \right]^2}{\left( \rho b_f d \right)^2} \right\} dx$$

$j = 1 \dots N_p.$

(5.2)

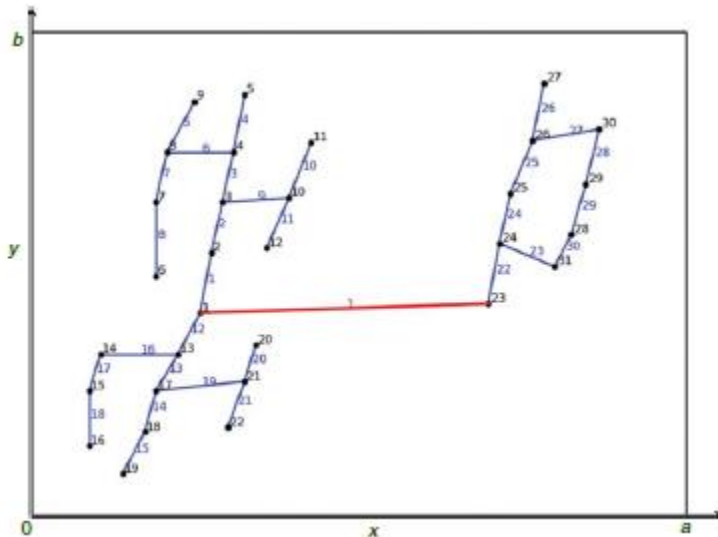


Figure 5.11: Schematic of fracture network discretization used in the semi-analytic solution of unsteady state gas flow in unconventional reservoirs, developed by Zhou *et al.* (2014).

Later, Wei *et al.* (2014) applied the same formulation to study gas production from complex fracture networks considering gas desorption. In their work, they investigated several hydraulic fracture network configurations, such as multiple vertical fractures, varying half-length fractures, and inclined hydraulic fractures. To validate the

well-fracture intersection in our model, one of the presented case studies in Wei *et al.* (2014) is selected. This example includes a horizontal well with 4 hydraulic fractures intersecting the well at 60 degree as shown in Figure 5.12. The fractures half-length is 305 ft and the spacing is 100 ft. Since the non-Darcy flow and gas desorption are not available in UTCOMP-EDFM, we compare the results with a case where  $\beta = 0$  and gas desorption is neglected. Moreover, this validation is only presented for UTCOMP-EDFM since modeling of gas phase is not allowed in UTGEL. However, the same methodology and formulation are applied in implementing well-fracture intersection in UTGEL-EDFM as well. In this simulation, in order to get more accurate results, the matrix grid is set to be  $101 \times 101 \times 1$  with gridblock dimensions of 19.8, 19.8, and 80 ft in X-, Y-, and Z-directions, respectively. Due to fractures discretization, 168 fracture cells are created in total. Additional reservoir and fluid properties are given in Table 5.5.

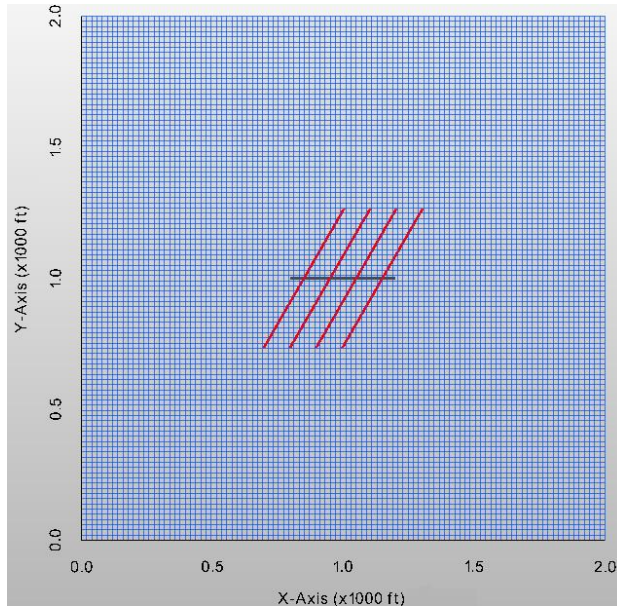


Figure 5.12: A reservoir model with 4 hydraulic fractures. The hydraulic fractures (red lines) intersect the horizontal well (black line) at 60 degree.

Overall Properties		CH <sub>4</sub> Properties	
Matrix Porosity (fraction)	0.15	Critical Pressure (psia)	667.38
Matrix Permeability (md)	0.0005	Critical Temperature (°R)	343.68
Fracture Permeability (md)	10000	Molecular Weight (lb/lb-mole)	16
Fracture Aperture (ft)	0.01	Parachor	71
Initial Reservoir Pressure (psi)	4500	Acentric Factor	0.008
Initial Water Saturation	0.1	Gas Viscosity (cp)	0.023536
Initial Gas Saturation	0.9	Gas Specific Gravity	0.58
Reservoir Temperature (°F)	130	Well Properties	
Rock Compressibility (psi <sup>-1</sup> )	0.000001	Well Radius (ft)	0.5
Fluid Compressibility (psi <sup>-1</sup> )	0.00014	Well BHP (psi)	1000

Table 5.5: Rock and fluid properties for the reservoir model in section 5.4.

Figure 5.13 shows the gas flow rate comparison between the semi-analytical solution and UTCOMP-EDFM. As observed, there is good agreement between the results, corroborating the accuracy of the implementation of well-fracture intersection. Moreover, the pressure profiles after 350 and 1500 days of gas production is illustrated in Figure 5.14. Fractures interference starts almost at 350 days, resulting in a production decrease compared to the simulation of 4 distinct hydraulic fractures. If we keep the fracture spacing constant, as the intersection angle decreases from 90 to 0 degree, fractures interference increases. Thus, the best practice is to drill horizontal wells parallel to the direction of minimum horizontal stress so that the hydraulic fractures propagate at 90 degree with respect to the well. However, due to heterogeneity of the reservoir and the uncertainty in the direction of stresses, often fractures develop at inclined angles and in the form of complex networks. Thus, modeling such features using bi-wing fracture models might not be accurate.

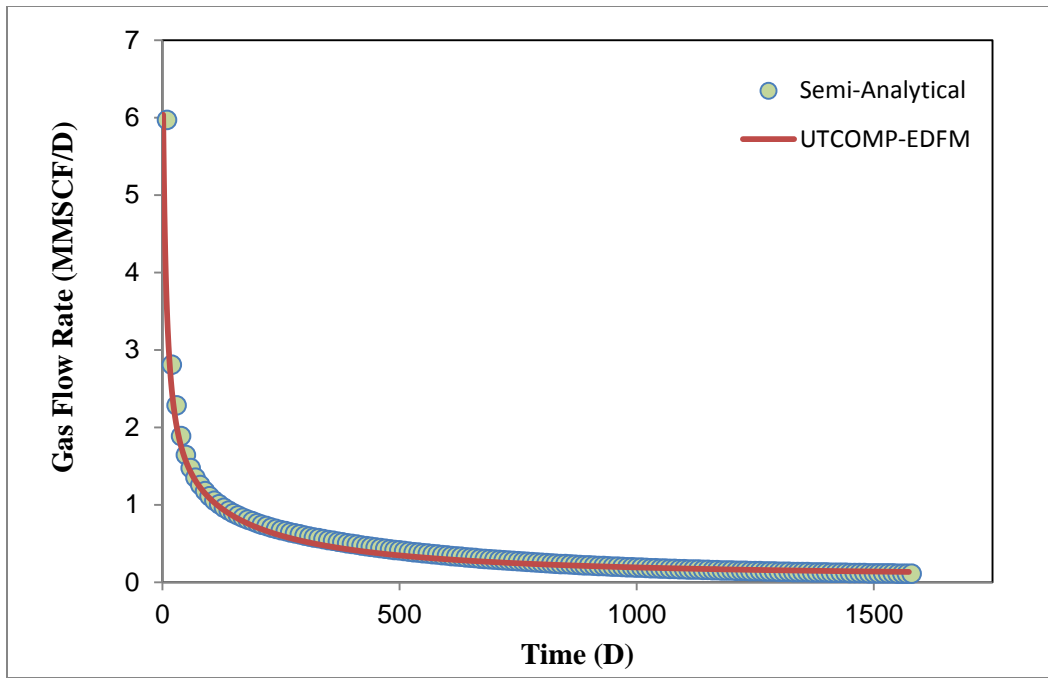


Figure 5.13: Comparison of gas flow rate obtained from UTCOMP-EDFM with the semi-analytical solution for a 2D reservoir model with 4 hydraulic fractures intersecting well at 60 degree.

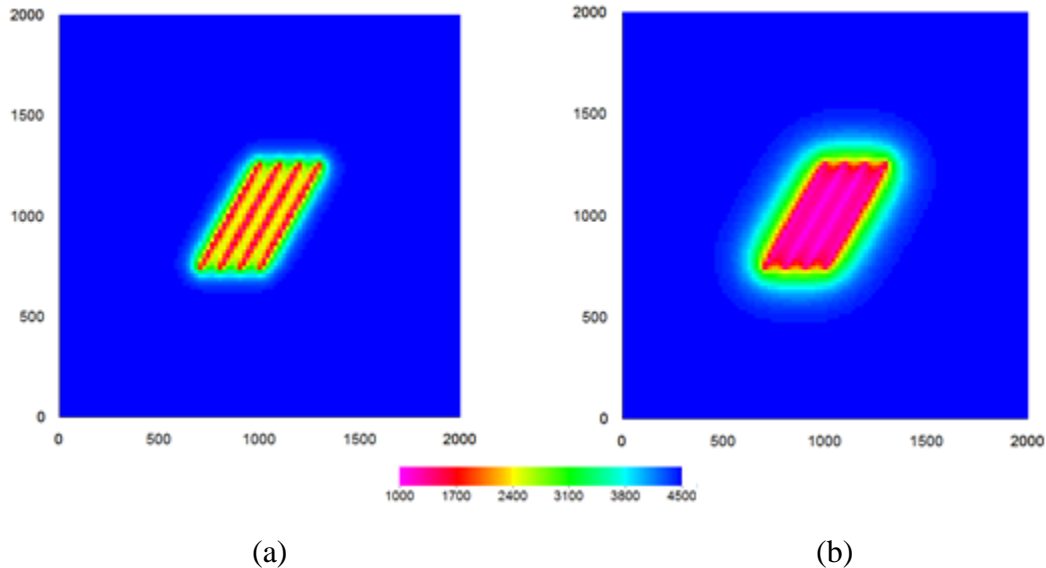


Figure 5.14: Pressure profiles after (a) 350 and (b) 1500 days for the reservoir model in section 5.4. The fractures interference starts almost at 350 days.

## **Chapter 6: Applications of UTCOMP-EDFM and UTGEL-EDFM**

This chapter presents several simulation case studies with the implemented EDFM approach in UTCOMP and UTGEL reservoir simulators. These examples are specified and presented to highlight the capabilities of these simulators in modeling more complex problems compared to those modeled with available commercial reservoir simulators. In the first two sections, UTCOMP-EDFM is applied to study the behavior of natural and induced fracture networks. First, we investigate the effect of well placement and the background fracture networks on the efficiency of water flooding. The same simulation runs are then performed with inclusion of the capillary imbibition effects. The results confirm the significance of capillary effects on hydrocarbon production, although these effects are neglected in most of simulation practices. In the last part of this chapter, two examples of conformance control techniques are presented in which UTGEL-EDFM is employed to model such processes. It is indicated that injecting high viscosity polymer gels into channels and conduits can significantly increase sweep efficiency, which in turn can further improve recovery factor.

### **6.1 WATER FLOODING IN FRACTURED RESERVOIRS**

Naturally fractured reservoirs are characterized by one or more sets of fracture networks. These networks are accounted as highly conductive pathways for oil and water transfer in the formation. The performance of such reservoirs is governed mainly by the configuration of the fracture networks. Thus, modeling and simulation of fractured reservoirs leads to erroneous results without accurate characterization of fracture networks. Moreover, the wettability condition of the reservoir rock itself plays an

important role in the success of a water flooding job as well. Favorable rock wettability can introduce capillary pressure contrast between fracture and matrix, which improves sweep efficiency and oil recovery. However, in the absence of capillary pressure effects, water flows mostly in a network of high permeability fractures and reaches production wells without displacing considerable amount of oil. Although numerous laboratory core flood experiments have been performed to understand the behavior of natural fractured reservoirs, the accurate prediction of reservoir performance still remains a challenge. In the following section, we investigate the effect of fracture networks complexity and capillary pressures using simulation case studies. First, the effect of well placement with respect to the background fracture network on reservoir performance is investigated. Capillary pressures are then added to the simulations to observe their significance. For all the simulations in this section, we use UTCOMP-EDFM simulator.

### 6.1.1 Well Placement

When a water flooding plan is designed for a naturally fractured reservoir, it is vital to determine the configuration of the background fracture network using geologic and geomechanics studies. This information further assists in well placement and completion design. To show the importance of such information, a series of simulation case studies is presented where several fracture networks are considered.

First, we investigate the effect of well placement in a 2D reservoir containing a network of 22 fractures. The fractures have a preferential orientation as shown in Figure 6.1. The matrix grid is  $50 \times 50 \times 1$  and the dimensions of each gridblock are 40 ft in all the directions. Due to discretization of the fracture planes, a total of 420 cells are added to the computational domain. Water is injected at a rate of 7000 STB/D. The BHP for producer

as well as the reservoir pressure is 3000 psi. The other rock and fluid properties are summarized in Table 6.1. To study the effect of network orientation, two different sets of well placements are considered for the injector and the producer. In the first case, the injector is located at the bottom left corner and the producer at the top right corner. We refer to this configuration as SW-NE, where the line connecting injector and producer is parallel to the fractures orientation. In the second case, we use the SE-NW configuration in which the line connecting these two wells is perpendicular to the fractures orientation. The locations of wells in these two cases are shown in Figure 6.1. The first and second sets of wells are shown with blue and red circles, respectively.

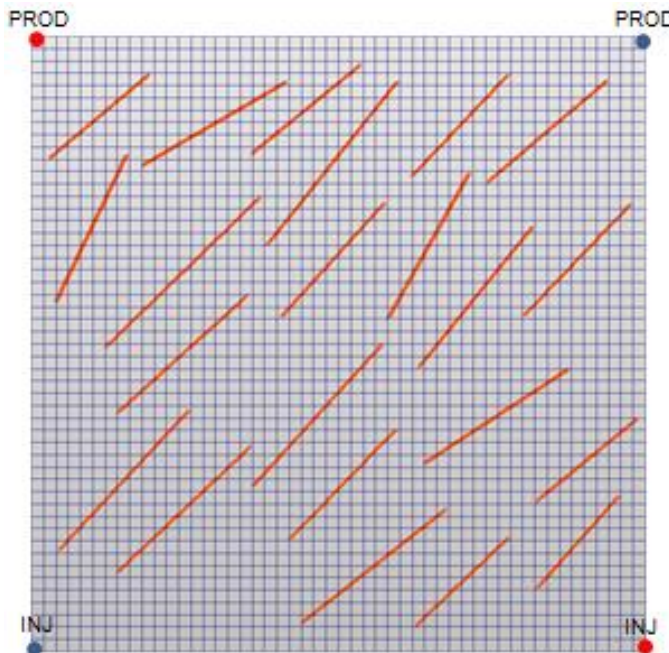


Figure 6.1: A reservoir model with a network of 22 fractures with preferential orientation. The effect of well placement is considered in this example. In the first case, injector-producer line is parallel to the SW-NE direction (blue circles), while for the second case, the line is in the SE-NW direction (red circles).

Overall Properties		Relative Permeability Curves for Matrix	
Matrix Porosity (fraction)	0.2	Irreducible Water Saturation	0.2
Matrix Permeability (md)	15	Water Rel. Perm. End Point	0.8
Fracture Permeability (md)	100000	Water Rel. Perm. Exponent	4
Fracture Aperture (ft)	0.025	Residual Oil Saturation	0.2
Initial Reservoir Pressure (psi)	3000	Oil Rel. Perm. End Point	0.7
Initial Water Saturation	0.2	Oil Rel. Perm. Exponent	2
Initial Oil Saturation	0.8	C <sub>10</sub> H <sub>22</sub> Properties	
Reservoir Temperature (°F)	60	Critical Pressure (psia)	350
Rock Compressibility (psi <sup>-1</sup> )	0.000001	Critical Temperature (°R)	1500
Fluid Compressibility (psi <sup>-1</sup> )	0.000005	Molecular Weight (lb/lb-mole)	142.23
Well Properties		Parachor	431
Well Radius (ft)	0.5	Acentric Factor	0.488
Producer BHP (psi)	3000	Water Viscosity (cp)	0.8
Injector Rate (STB/D)	7000	Oil Viscosity (cp)	0.19

Table 6.1: Rock and fluid properties of the reservoir model in section 6.1. The relative permeability curves are straight lines for fractures.

Figures 6.2 to 6.4 illustrate the simulation results for the reservoir model with two different well placements. As observed from the plots, although the reservoir properties remain constant, by merely changing the location of injector and producer, a completely different behavior is displayed by the reservoir. As expected, when water is injected parallel to fractures direction, breakthrough occurs much faster resulting in poor sweep efficiency and lower oil recovery. In this example, for the SW-NE case, water reaches the producer 200 days earlier compared to the other case, and recovery decreases more than 10 percent. Moreover, if we compare the water saturation profiles for both cases at 150 and 350 days, as shown in Figure 6.5, it is evident that when the water front moves perpendicular to the fractures direction, the effect of fracture network is almost negligible and saturation profile is similar to that of a homogenous reservoir without fractures. This clearly indicates the significance of background fracture network on the performance of reservoir.

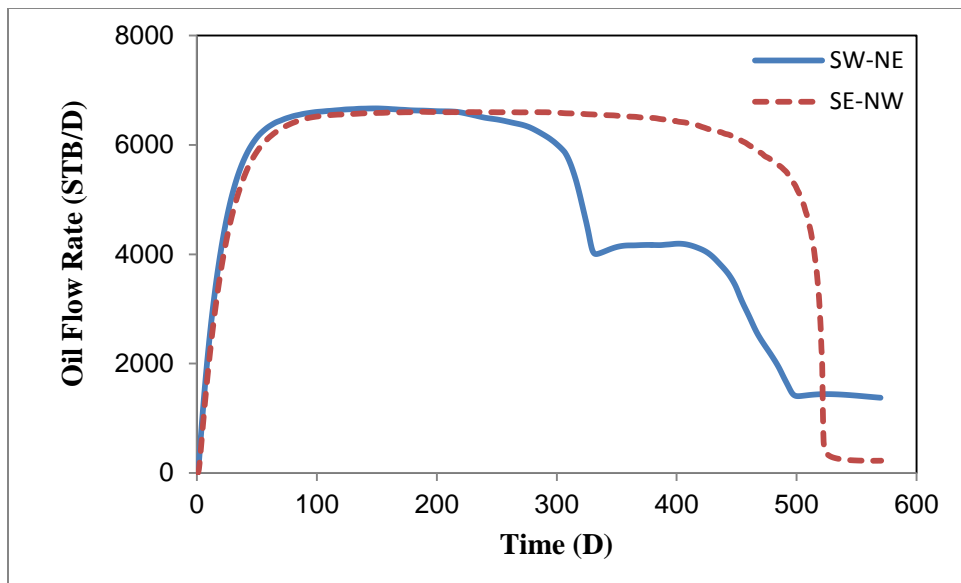


Figure 6.2: Oil production rates for the reservoir model with a network of 22 fractures. Results are shown for two different well placements.

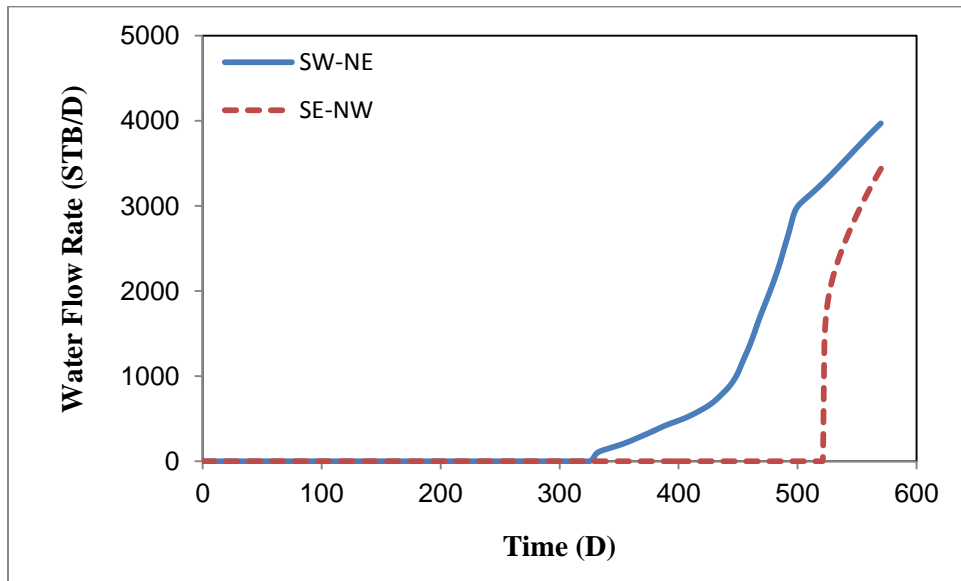


Figure 6.3: Water production rates for the reservoir model with a network of 22 fractures. Results are shown for two different well placements.

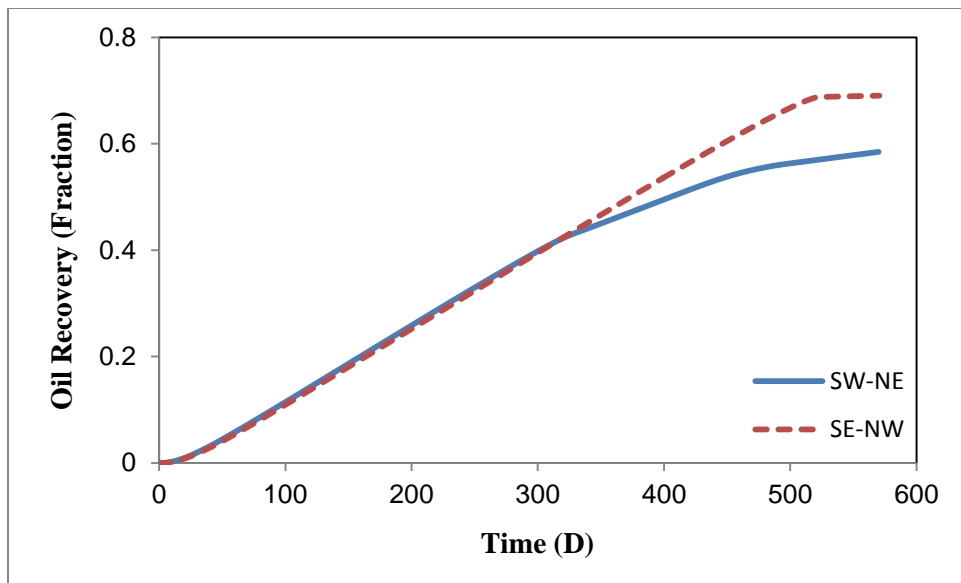


Figure 6.4: Oil recovery for the reservoir model with a network of 22 fractures. Results are shown for two different well placements.

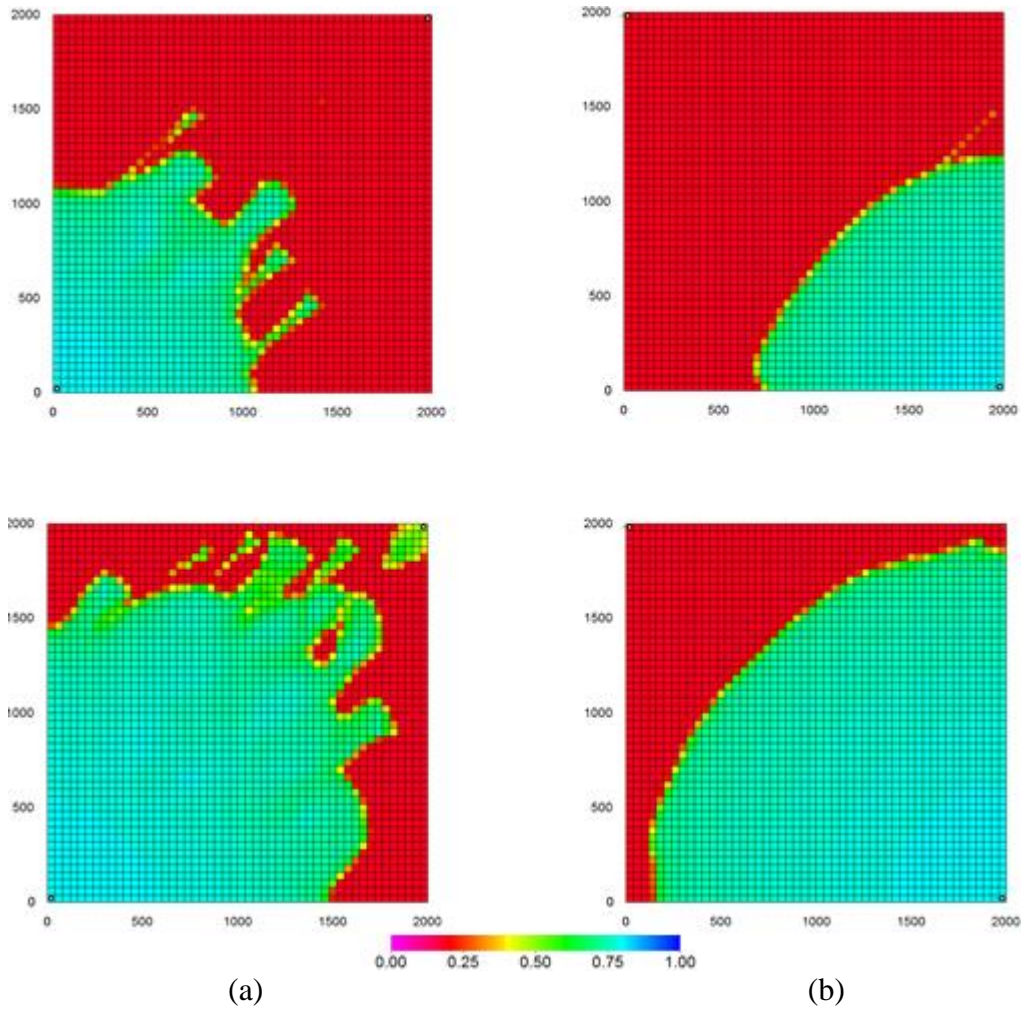


Figure 6.5: Water saturation profiles for the reservoir model with a network of 22 fractures after 150 days (top row) and 350 days (bottom row). Results are shown for two different well placements, (a) SW-NE and (b) SE-NW.

In fractured reservoirs, mostly there are more than one set of fracture network. Depending on the geomechanical condition and tectonic movements, these networks may have different orientations and dip angles. In such reservoirs, the accurate characterization of individual fracture networks becomes very troublesome. However, if the number of networks increases, due to high density of fractures and variation of their

orientations, it is difficult to find a specific direction as the outcome of all the sets. Thus, reservoir performance becomes less sensitive to the well placement. To evaluate this conjecture, another fracture network is added to the previous reservoir model as shown in Figure 6.6. Including the new network, a total of 39 fracture planes and 747 fracture cells are modeled in this problem. The fractures in the new network (green lines) are almost perpendicular to the former fractures (red lines). Similar to the previous section, two scenarios for well placement are investigated. First, injector is inserted at the bottom left corner while the producer is at the opposite corner. This set of injector and producer is shown with blue circles in Figure 6.6 and are referred to as SW-NE configuration. The locations of injector and producer are then changed to SE-NW direction as shown by red circles. The other reservoir and fluid properties are the same as those of the previous reservoir model.

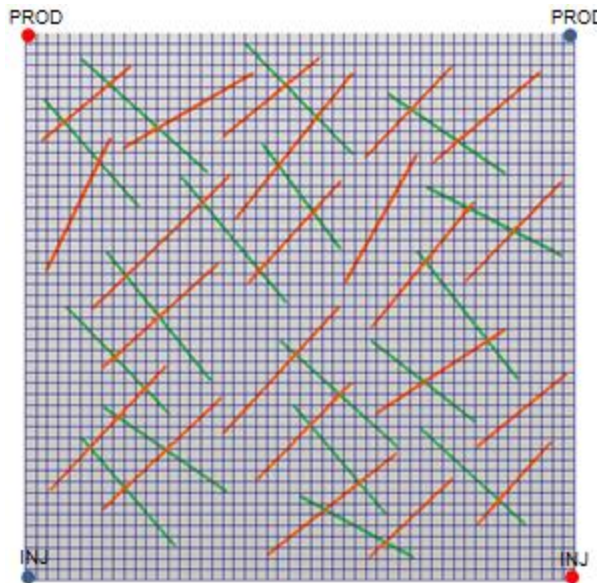


Figure 6.6: A reservoir model with 2 networks of 39 fractures. The effect of well placement is considered in this example. In the first case, injector-producer line is parallel to the SW-NE direction (blue circles), while for the second case, the line is in the SE-NW direction (red circles).

Figures 6.7 to 6.9 depict the simulation results for the reservoir model with two fracture networks. As observed from the plots, the difference between the curves for the two well placement scenarios has decreased significantly compared to the case of the reservoir model with one fracture network, although still some discrepancy is evident in later times. Figure 6.7 indicates that water breakthrough has occurred 30 days earlier in SW-NE configuration compared to the other well placement, while this gap was about 200 days in the previous example. Also, the oil recovery factors are close to each other for the two-networks example, confirming the fact that multiple fracture networks tend to make reservoir more isotropic compared to the case of one fracture network with preferential direction. In fact, although the connectivity and proximity (spacing) of individual fractures differ from one network to another, their combination behaves almost similarly in various directions. This effect becomes more evident as the number of fracture networks increases. This is why the dual continuum approaches are sufficiently accurate for modeling dense fractured reservoirs.

Moreover, based on the water saturation profiles shown after 130 and 360 days for both scenarios (Figure 6.10), we can observe that water invasion patterns are closely matched compared to Figure 6.5. Although the front movement is mainly controlled by the network parallel to the direction of flow, still the same behavior is observed for both cases, which is completely distinct from the one shown in Figure 6.5b.

According to the above discussions, we can conclude that not only the properties of individual fracture networks must be studied for well placement and further reservoir development, fracture networks interaction must also be taken into account as well. Although the existence of multiple fracture networks might seem to complicate the problem, their combination can eliminate the directionality associated with individual fractures, as long as they possess similar properties, such as fractures permeability.

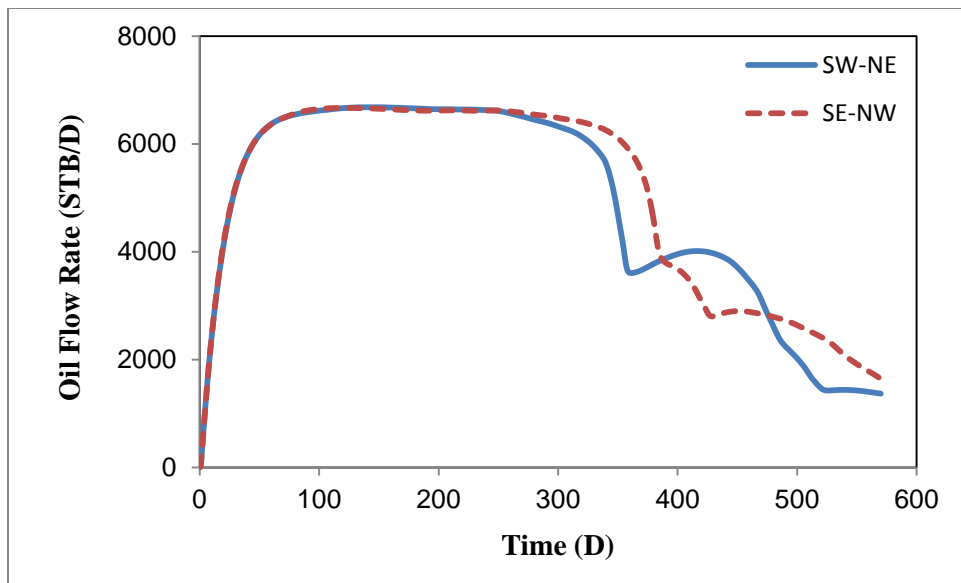


Figure 6.7: Oil production rates for the reservoir model with two sets of fracture networks. Results are shown for two different well placements.

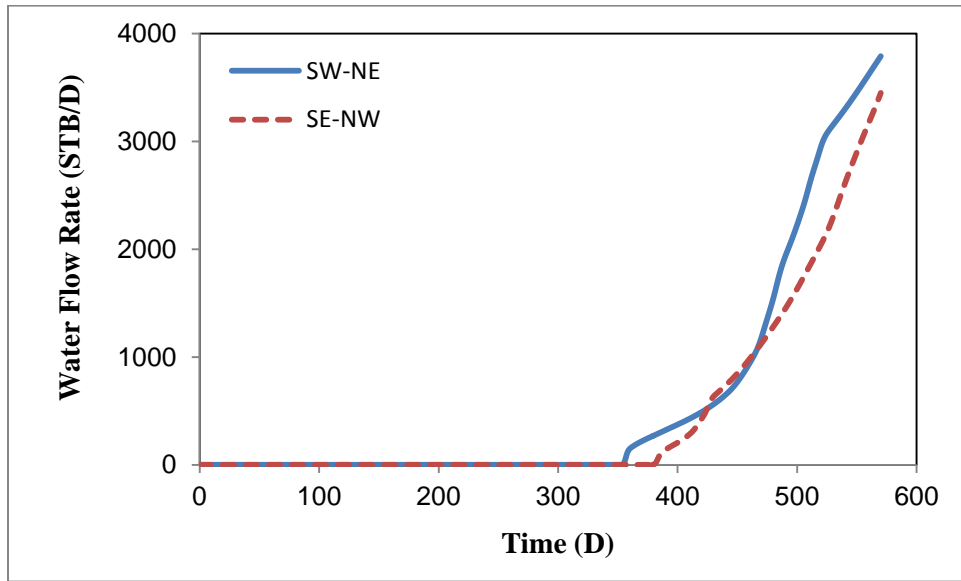


Figure 6.8: Water production rates for the reservoir model with two sets of fracture networks. Results are shown for two different well placements.

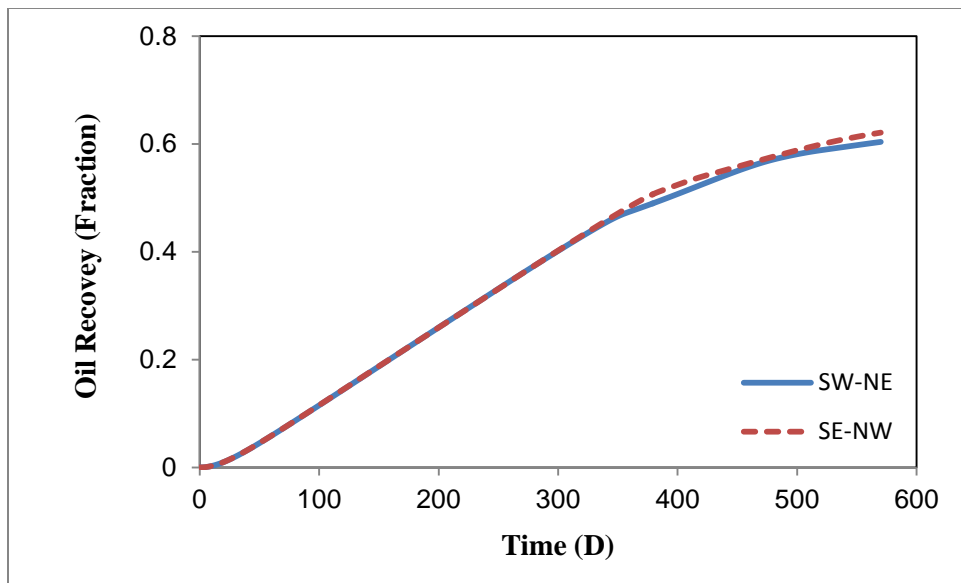


Figure 6.9: Oil recovery for the reservoir model with two sets of fracture networks. Results are shown for two different well placements.

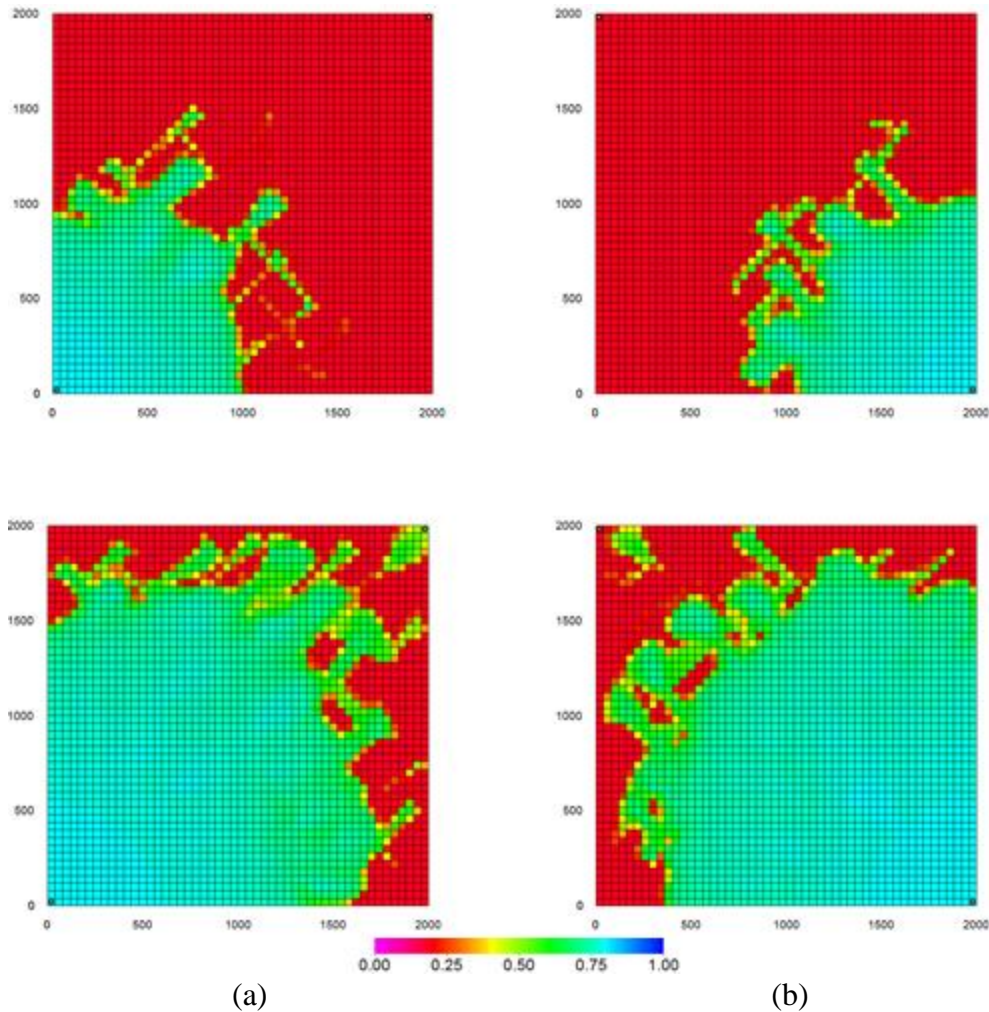


Figure 6.10: Water saturation profiles for the reservoir model with two fracture networks after 130 days (top row) and 360 days (bottom row). The results are shown for two different well placements, (a) SW-NE and (b) SE-NW.

### 6.1.2 Capillary Pressure Effect

In water-wet fractured reservoirs, capillary imbibition appears to be one of the most important mechanisms for oil production, compared to viscous displacement. Due to distribution of highly conductive fractures throughout the reservoir, the injected fluid travels between injectors and producers without displacing considerable amount of oil,

bypassing significant portions of a reservoir. Thus, viscous displacement alone is not an efficient mechanism for oil production in fractured reservoirs. However, the presence of capillary imbibition effects, mostly in water-wet rocks, improves the sweep efficiency and therefore results in higher recovery factors. Water is spontaneously imbibed into the rock matrix, the main storage domain, and pushes oil out to the fracture system, the main conductive path. It has been shown that fracture system provides a path for the injected fluid to access larger un-swept regions. In fact, fracture network increases the contact area of the wetting phase and the rock matrix which in turn maximizes the capillary imbibition effects. However, the impact of various fracture network configurations on capillary pressure effects has not been well studied. In this section, the presented examples in the preceding part are investigated again under capillary imbibition effects to determine the importance of the network configuration on such processes. Moreover, different values for capillary pressure parameters are considered to evaluate their impact on ultimate oil recovery.

In UTCOMP, the capillary pressure between water and oil phases is calculated based on Eq. (6.1) where  $P_{wo}^c$  is capillary pressure,  $C_{pc}$  and  $E_{pc}$  are matching parameters,  $\sigma_{wo}$  is oil-water interfacial tension,  $\phi$  is porosity,  $k$  is permeability, and  $\bar{S}_w$  is normalized water saturation. In the following case studies, two sets of parameters are considered, as given in Table 6.2, and are referred to as  $P_c^1$  and  $P_c^2$ . The capillary pressure effect is more significant in  $P_c^2$  compared to  $P_c^1$ . For a medium water-wet rock, we use  $P_c^1$ , while  $P_c^2$  is applied for a strongly water-wet rock matrix.

$$P_{wo}^c = -C_{pc}\sigma_{wo}\sqrt{\frac{\phi}{k}}(1-\bar{S}_w)^E_{pc}. \quad (6.1)$$

	$C_{pc}$	$E_{pc}$	$\sigma_{wo}$ (dynes/cm)
$P_c^1$	10	1	50
$P_c^2$	60	1.5	60

Table 6.2: Two sets of parameters for capillary pressure calculations. The second set results in strong capillary pressure effects.

To determine the impact of capillary pressure on oil production, the reservoir model in Figure 6.1 (with a network of 22 fractures) is selected. Two simulation runs are performed with different sets of capillary pressure parameters as given in Table 6.2, and the results are compared to the case where capillary pressure is neglected. Figures 6.11 to 6.13 show the results for the SW-NE well placement. For this well configuration, since injection is made parallel to the direction of fractures, water is transferred faster by the fracture network. As a result, water contacts a larger portion of the reservoir and imbibes into the rock matrix more efficiently, which in turn increases the sweep efficiency and the oil recovery. Moreover, if we compare the water production plots (Figure 6.12), it is evident that by increasing the capillary pressure effects, the water breakthrough time is delayed, because the imbibition takes some water out of high permeability fractures and therefore limits the front movement in the fracture system toward the producer. Figure 6.14 shows this concept with the water saturation profiles for all the cases at 300 days. In overall, for the SW-NE well configuration capillary pressure has positive effects.

However, for the SE-NW well placement, the capillary imbibition has almost no effect on reservoir performance (Figures 6.15 to 6.17). Due to the direction of water front movement and the orientation of fractures, the network has no influence on fluid flow, and thus water invasion follows a simple pattern (Figure 6.5b). As mentioned above, capillary imbibition process is controlled by the fracture network. Hence, since the background fracture network is neutral in this case, capillary effects are negligible too.

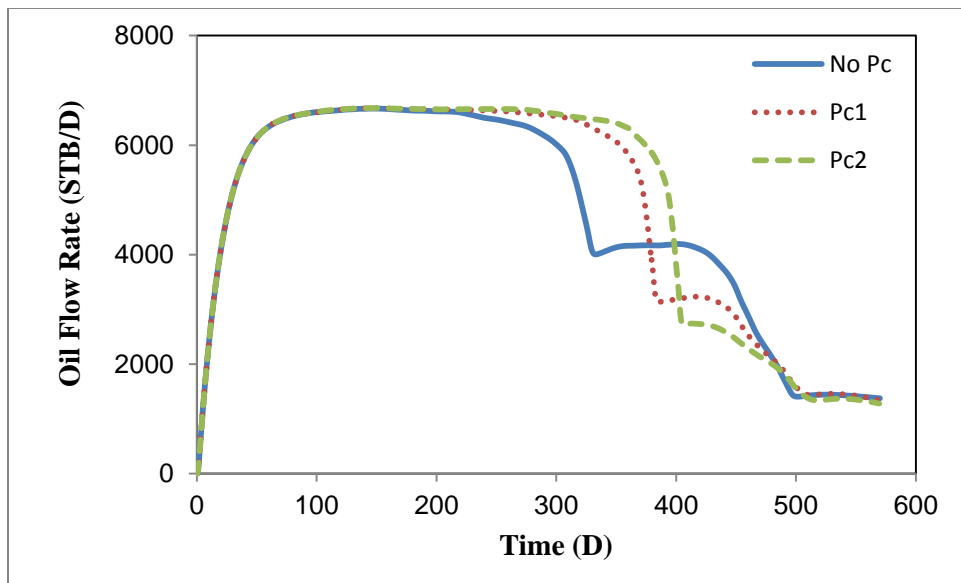


Figure 6.11: Oil production rates for the reservoir model with one set of fracture network and the SW-NE well placement. Results are shown for two cases with different capillary pressure values as well as one case with no capillary pressure.

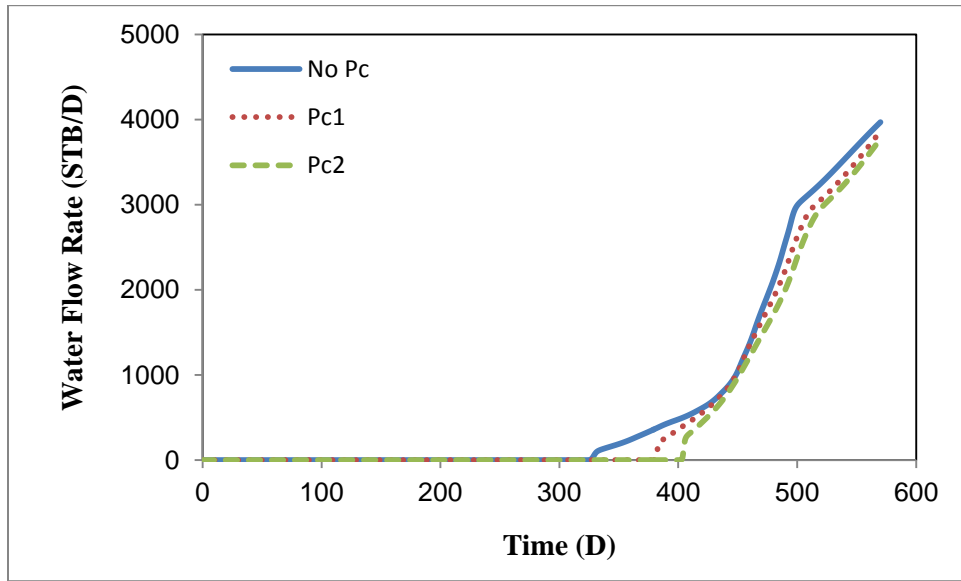


Figure 6.12: Water production rates for the reservoir model with one set of fracture network and the SW-NE well placement. Results are shown for two cases with different capillary pressure values as well as one case with no capillary pressure.

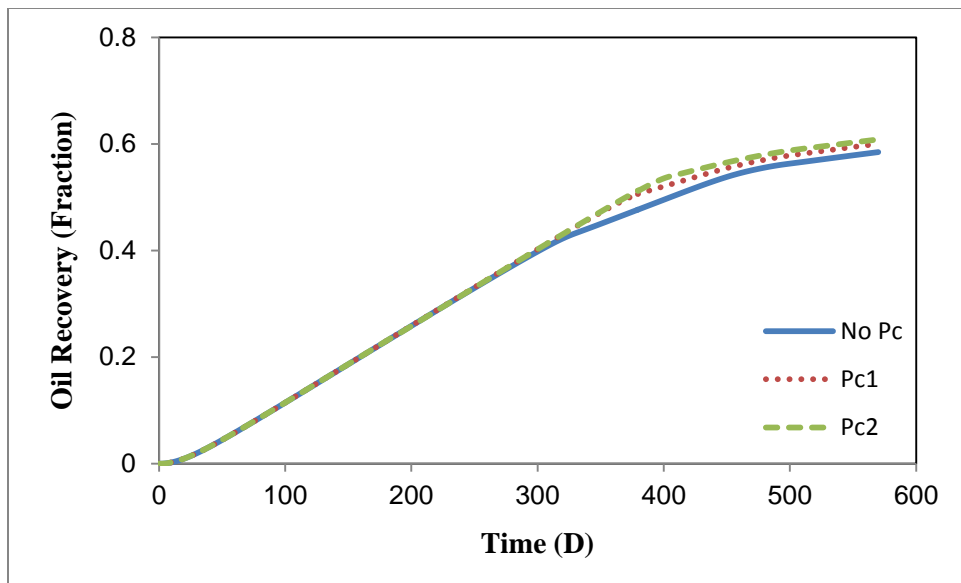


Figure 6.13: Oil recovery for the reservoir model with one set of fracture network and the SW-NE well placement. Results are shown for two cases with different capillary pressure values as well as one case with no capillary pressure.

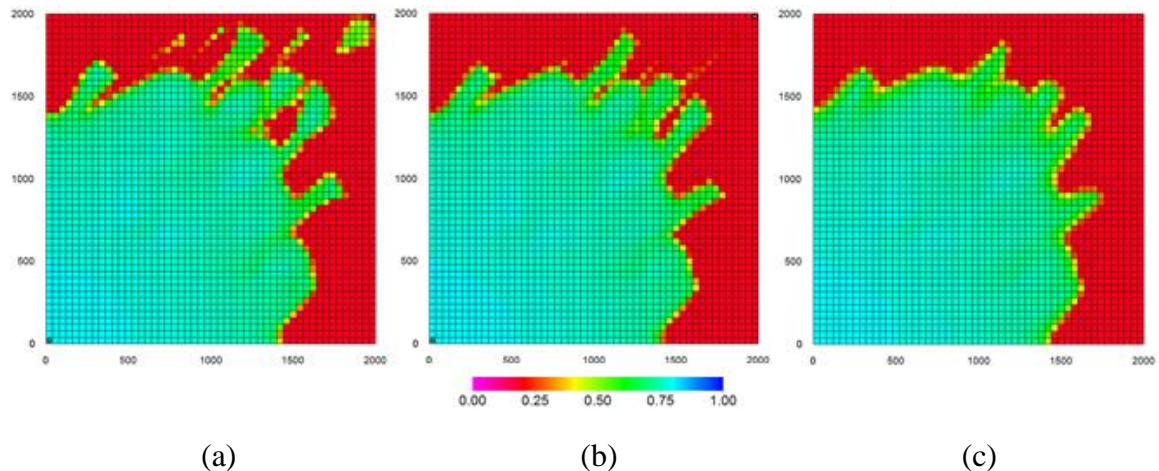


Figure 6.14: Water saturation profiles at 300 days for the reservoir model with one set of fracture network. Profiles are shown for (a) no capillary pressure, (b)  $P_c^1$ , and (c)  $P_c^2$  cases.

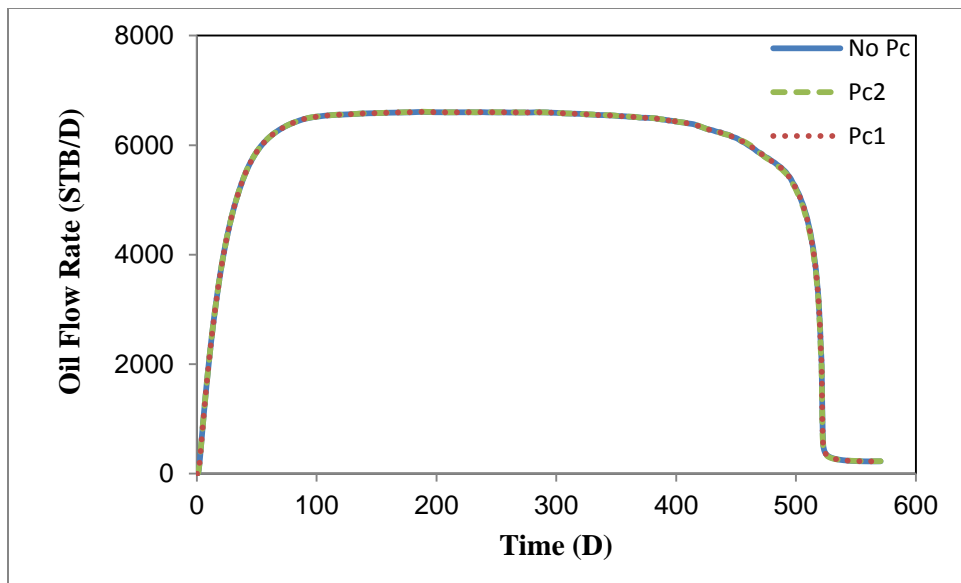


Figure 6.15: Oil production rates for the reservoir model with one set of fracture network and the SE-NW well placement. Results are shown for two cases with different capillary pressure values as well as one case with no capillary pressure.

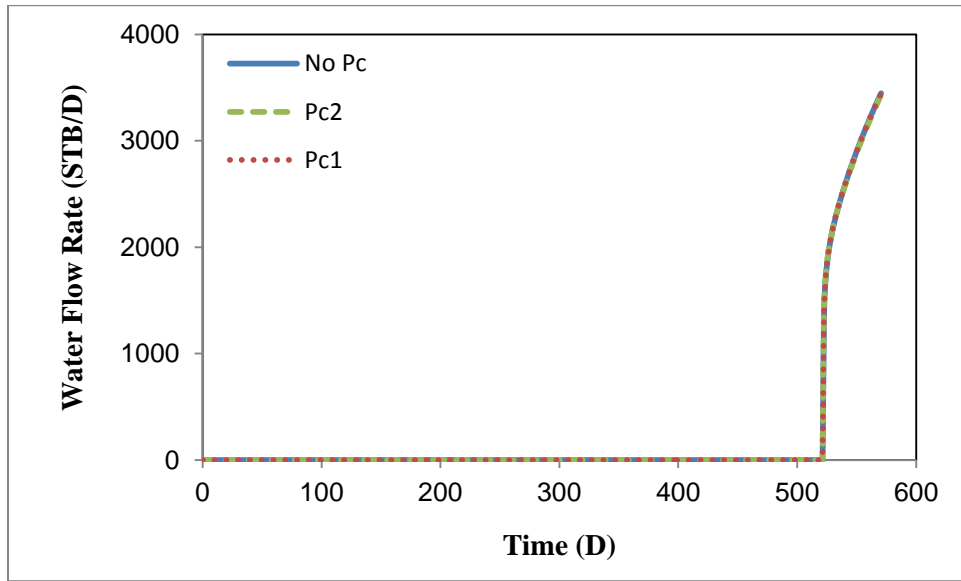


Figure 6.16: Water production rates for the reservoir model with one set of fracture network and the SE-NW well placement. Results are shown for two cases with different capillary pressure values as well as one case with no capillary pressure.

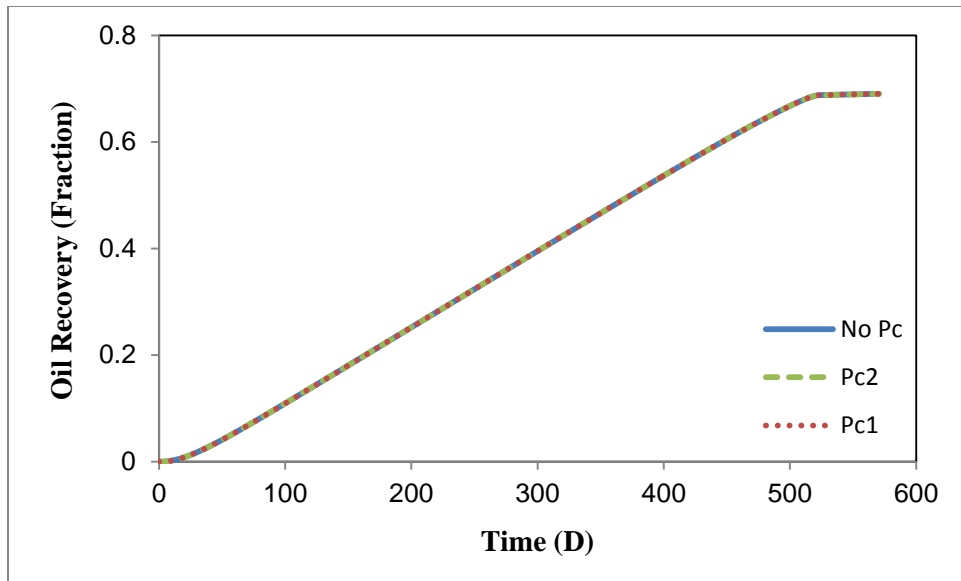


Figure 6.17: Oil recovery for the reservoir model with one set of fracture network and the SE-NW well placement. Results are shown for two cases with different capillary pressure values as well as one case with no capillary pressure.

As mentioned before, when there are more than one active fracture set available in the reservoir, due to variation of the orientation angles and the geometry of fractures between sets, the reservoir behavior appears to be less sensitive to the well placement. Moreover, when capillary imbibition effect is significant in reservoir, the injected water gradually leaves the fracture system and flows in the rock matrix. Therefore, the effect of fracture network on water flow decreases. In fact, capillary imbibition diminishes further the variability of fracture networks, and in strongly water-wet reservoirs it eliminates the effect of well placement. To elicit this concept, we consider again the reservoir model of Figure 6.6 with two sets of fracture networks. Earlier, we compared the simulation results of water flooding in this reservoir for two different well placement scenarios without the capillary pressure consideration and the graphs were shown in Figures 6.7 to 6.9. Now, we investigate the same water flooding process in the presence of high capillary

imbibition effects. To do so, capillary pressure parameters of  $P_c^2$  are applied. Figures 6.18 to 6.20 illustrate the simulation results for the two well configurations. As we can see, the difference between two curves has decreased considerably with respect to the comparison made under no capillary pressure condition (Figures 6.7 to 6.9). Thus, it implies that capillary imbibition effects flatten the drastic changes in the water front due to the existence of highly conductive pathways, such as fractures or channels. The concept is somehow similar to the effect of capillary pressure on viscosity fingering in which high imbibition effects tend to stabilize the front and therefore reduce the corresponding effect of heterogeneities. Accordingly, Figure 6.21 presents the water saturation profiles for the two well placement scenarios with and without capillary pressure considerations. The profiles are shown at 220 days. As can be seen, at high capillary pressure effects, the water channelings vanish.

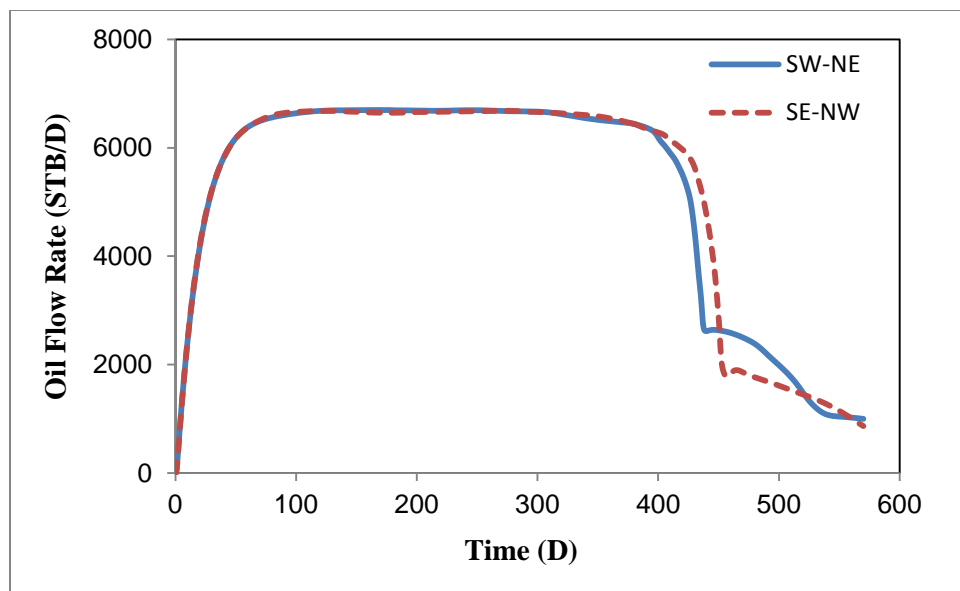


Figure 6.18: Oil production rates for the reservoir model with two sets of fracture networks under high capillary pressure effects ( $P_c^2$ ). Results are shown for two different well placements.

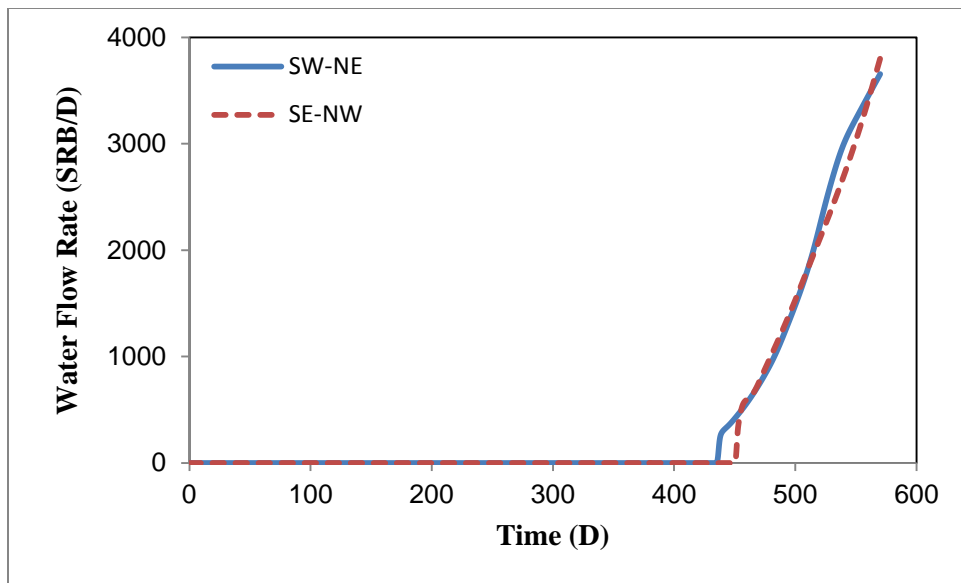


Figure 6.19: Water production rates for the reservoir model with two sets of fracture networks under high capillary pressure effects ( $P_c^2$ ). Results are shown for two different well placements.

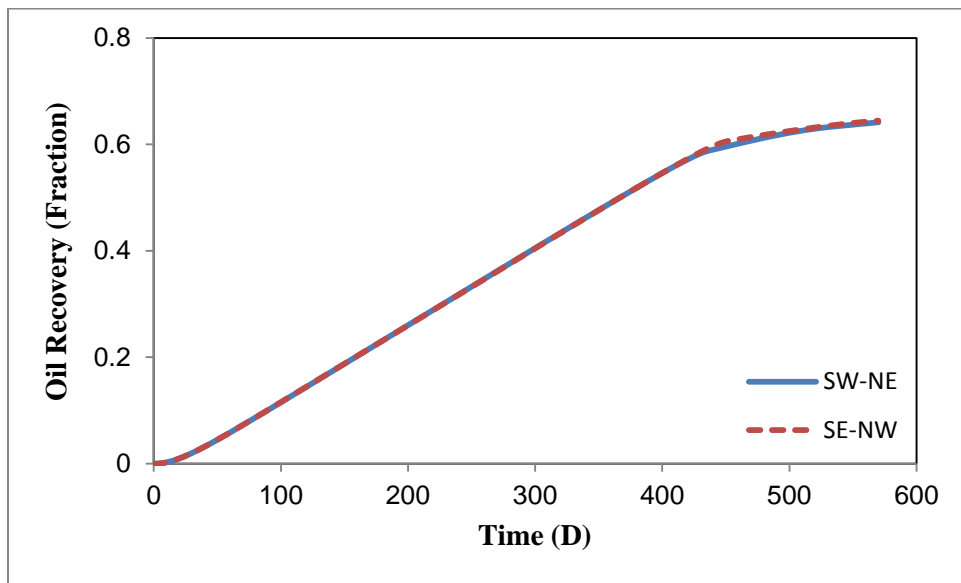


Figure 6.20: Oil recovery for the reservoir model with two sets of fracture networks under high capillary pressure effects ( $P_c^2$ ). Results are shown for two different well placements.

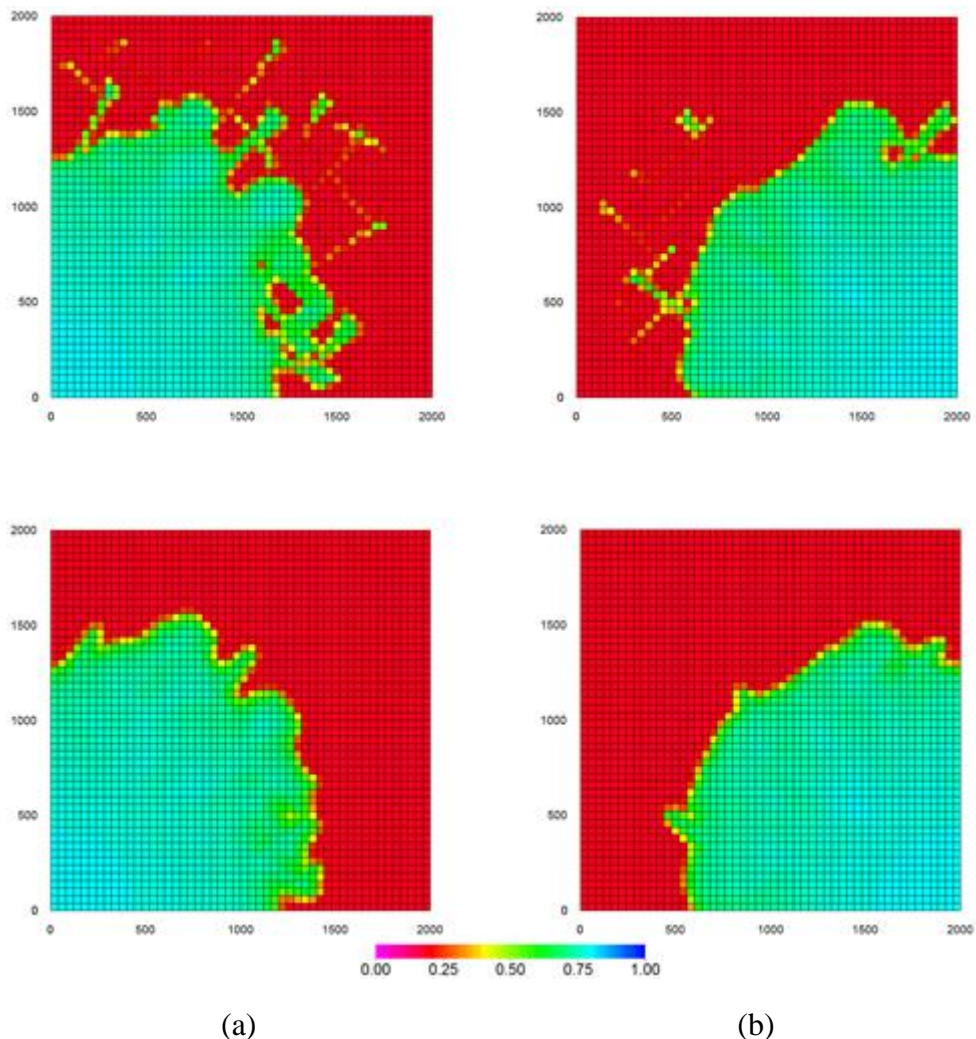


Figure 6.21: Water saturation profiles at 220 days for the reservoir model with two sets of fracture networks for (a) the SW-NE and (b) the SE-NW well placements. The top row shows the results without capillary pressure consideration while the bottom row shows the results with capillary pressure consideration ( $P_c^2$ ).

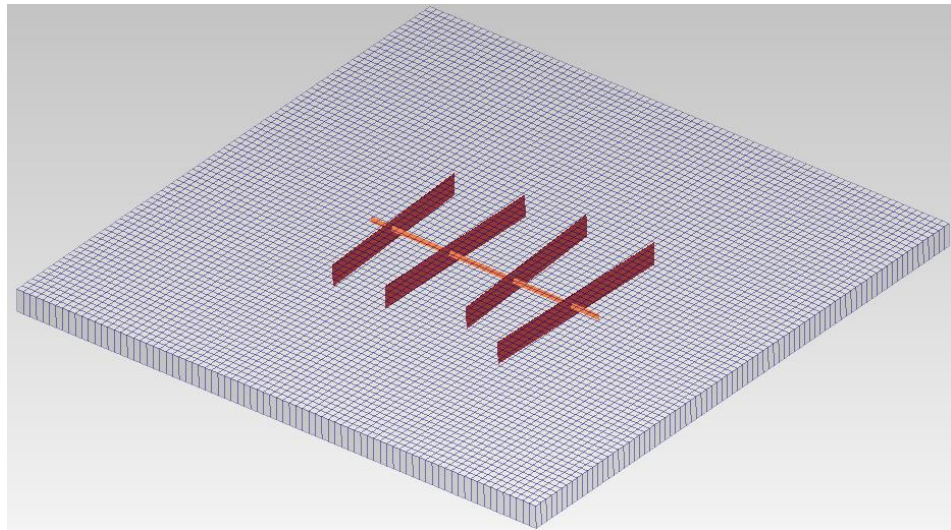
## **6.2 HYDRAULIC FRACTURING DESIGN AND TREATMENT**

After almost one decade of development and exploitation of unconventional and tight formations, there is no doubt that hydraulic fracturing is the most viable technology for hydrocarbon production from such reservoirs. However, it still remains a challenge how to operate and design such stimulation processes and subsequently how to characterize the created networks of fractures. Due to the heterogeneity of the reservoir rock, the existence of natural fracture system, and the variation of stress regime in near wellbore regions, the hydraulic fracturing may develop complex networks. On the other hand, there are other parameters in terms of operation that control the associated degree of complexity as well. The injected fluid viscosity, injection pressure, and spacing between fracture stages are such parameters. To maximize the well productivity and improve the reservoir performance, it is essential to carefully investigate the effect of these parameters. In fact, comprehensive models are required to enable reservoir and production engineers to tackle such problems. In this section, to illustrate another application of the UTCOMP-EDFM, we use this reservoir simulator to study the effect of fracture network complexity on the performance of reservoirs with various ranges of matrix permeabilities.

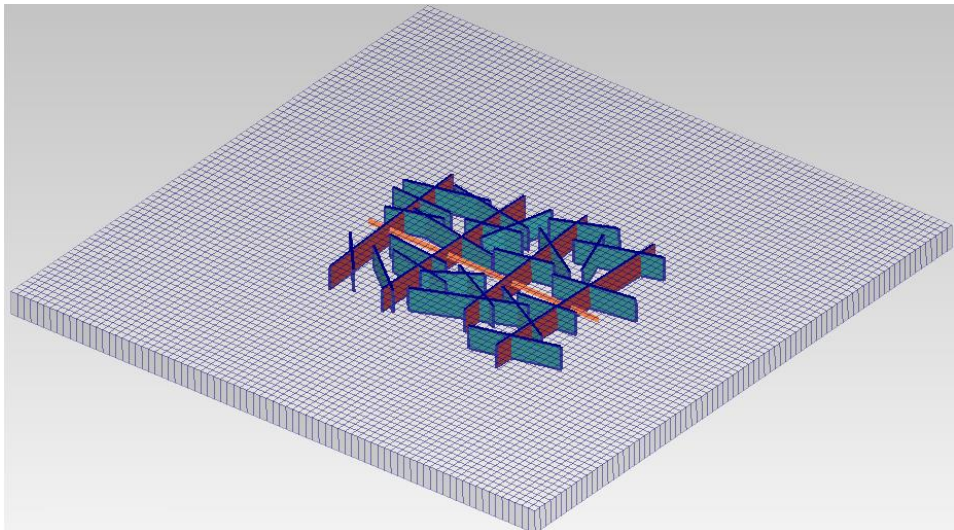
Fracture network complexity is one of the key parameters that influence the well productivity and reservoir performance. When a low viscosity fluid is used, the fracture network growth is mostly complex with branches of fissures and cracks, while high viscosity fluid tends to form mostly planar fractures. The main advantage of creating a complex network is increasing the stimulated region and also the surface area of the fracture system. In very low permeability reservoirs, this can substantially enhance the hydrocarbon production. However, these types of fracture networks, depending on the properties of reservoir rock, may require a larger volume of fracture fluid and also a

careful design of the proppant distribution. When permeability of the reservoir rock is moderate to high, fluid leak-off increases significantly and affects the cost of stimulation job. Moreover, proppant distribution is another challenge that influences the ultimate conductivity of the fracture system. Thus, whether a complex network needs to be created or not must be an operational decision. In the following section, to study this concept, we compare the performance of a complex fracture network versus a simple fracture configuration by evaluating the gas production. To do so, three types of reservoirs are considered: a shale gas reservoir model with 50 nd permeability, a tight gas reservoir model with 50  $\mu$ d permeability, and a conventional gas reservoir model with 5 md permeability. The  $80 \times 80 \times 1$  reservoir grid and the position of the fractures are shown in Figure 6.22. For the simple configuration, there are only 4 long planar fractures (shown in red) created at about 250 ft spacing (Figure 6.22a). These fractures are called primary fractures and are created in practice using high viscosity fluids made with cross-linked gels. For the complex network, 27 fracture planes are used in which the short fracture planes (shown in blue) are distributed around the primary fractures. The aperture of all the fractures is 0.0362 and 0.01 ft in simple and complex networks, respectively, to make the pore volume of the fracture systems equal in both cases. The assumption is that the same volume of the injected fluid has been used in both cases to create the fractures, and the fluid leak-off is constant as well. However, in reality, if we keep the matrix permeability constant, the leak-off is higher in the complex network because of the higher fracture surface area. The fractures permeability is proportional to the aperture squared. Thus, for the simple configuration, the fractures permeability is 120000 md, while for the complex network, the fractures permeability is 10000 md. The other rock and fluid properties are identical in both cases and are summarized in Table 5.5. In these case studies, we consider only the effect of fracture network complexity on gas production and

we neglect the gas desorption and the non-Darcy effects. For more detail characterization of fracture networks, one can refer to Cipolla *et al* (2010) and Mayerhofer *et al* (2006).



(a)



(b)

Figure 6.22: Reservoir models for (a) the simple and (b) complex hydraulic fracture networks. The well, the primary fractures, and the small branched fractures are shown in orange, red, and blue, respectively.

If we look at the simulation results for the simple and complex fracture networks in the reservoir with 50 nd permeability (Figure 6.23), we can observe that there is a huge difference in cumulative gas productions between the two cases. The production for the complex network is almost four times greater than the production for the simple planar fractures after 1750 days. This fact is clear in the drawdown curve as well (Figure 6.24). Also, if we compare the pressure map for both cases after 3000 days as shown in Figure 6.25, it is evident that pressure depletion is higher in the case of complex network and a greater portion of the reservoir is affected by the fracture system. However, for the tight reservoir with matrix permeability of 50  $\mu$ d, almost no difference is observed in the simulation results. The cumulative gas production and pressure drawdown curves almost overlap as shown in Figure 6.26 and 6.27. Also, if we compare the pressure profiles after 400 days, again we can observe that both networks have depleted similar regions and pressure depletion has then propagated almost symmetrically in the reservoir (Figure 6.28). For the 5 md matrix permeability case, the cumulative gas production and average reservoir pressure are shown in Figures 6.29 and 6.30. For the conventional type of gas reservoirs, it is shown that primary fractures with higher permeabilities result in better gas productions. The pressure profile is also presented for both cases at 20 days in Figure 6.31. Since the same size of reservoir has been used in all the examples, the pressure depletion occurs too fast in the case of 5 md matrix permeability. Hence, the pressure profiles are shown at 20 days. Note that the color bars are different for the pressure profiles shown in each section.

According to the results presented above, for nano-Darcy reservoirs, such as shale gas formations, a complex hydraulic fracture network is preferred. In fact, a complex network increases the stimulated region and a greater part of the reservoir is brought in contact with the fracture system. In such reservoirs, creating complex hydraulic fracture

networks enhances the conductivity of near wellbore regions and therefore improves gas production significantly. To achieve these large networks, a low viscosity fluid is injected. On the other hand, when the permeability of the reservoir is moderate, such as in conventional reservoirs (in the order of milli-Darcy), a dense fracture network is not an optimum design anymore. Since the rock matrix has enough flow capacity, the fluid delivery to the fracture system happens much faster. Thus, instead of a complex network, simple planar fractures with higher permeabilities can exploit the reservoir more efficiently. Also, since the permeability of these formations is high, fluid loss must be minimized as well using high viscosity fluids with gel or polymer additives. Finally, for tight reservoirs with permeability of micro-Darcy, although the difference between the results was not as significant as the other two cases, still a complex fracture network is preferred in the industry because of low permeability of the formation rock.

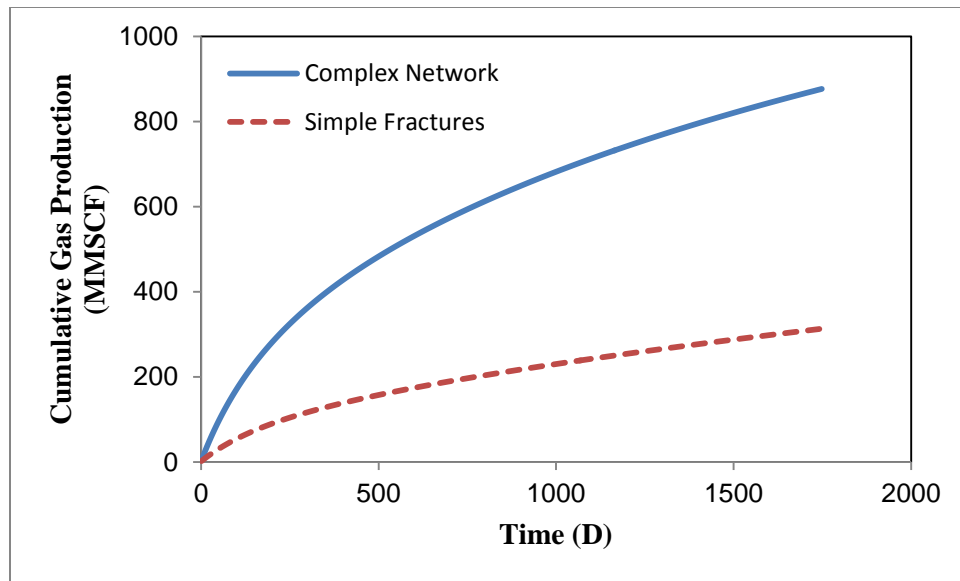


Figure 6.23: Cumulative gas production for the simple and complex fracture networks. In this case, the rock matrix permeability is 50 nd.

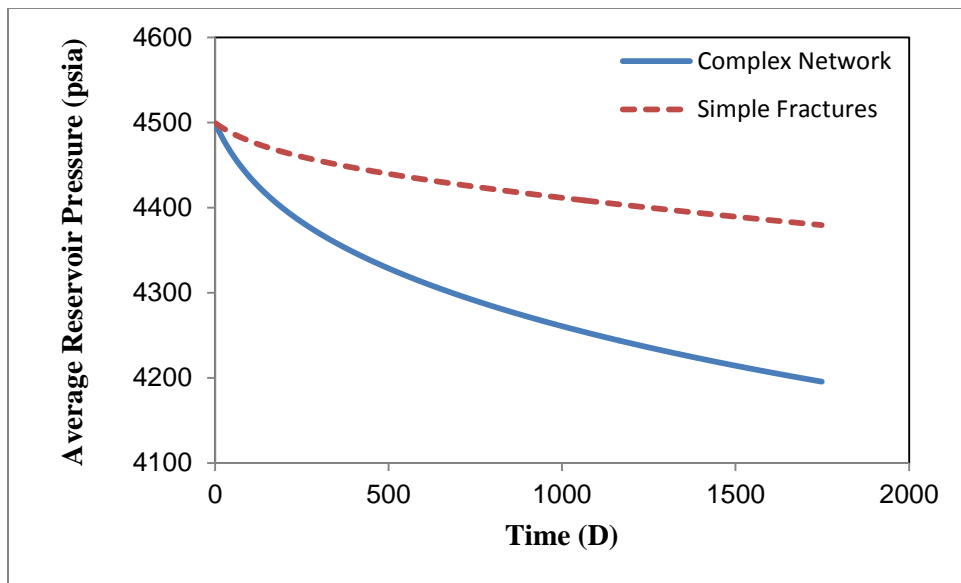


Figure 6.24: Average reservoir pressure versus time for the simple and complex fracture networks. In this case, the rock matrix permeability is 50 nd.

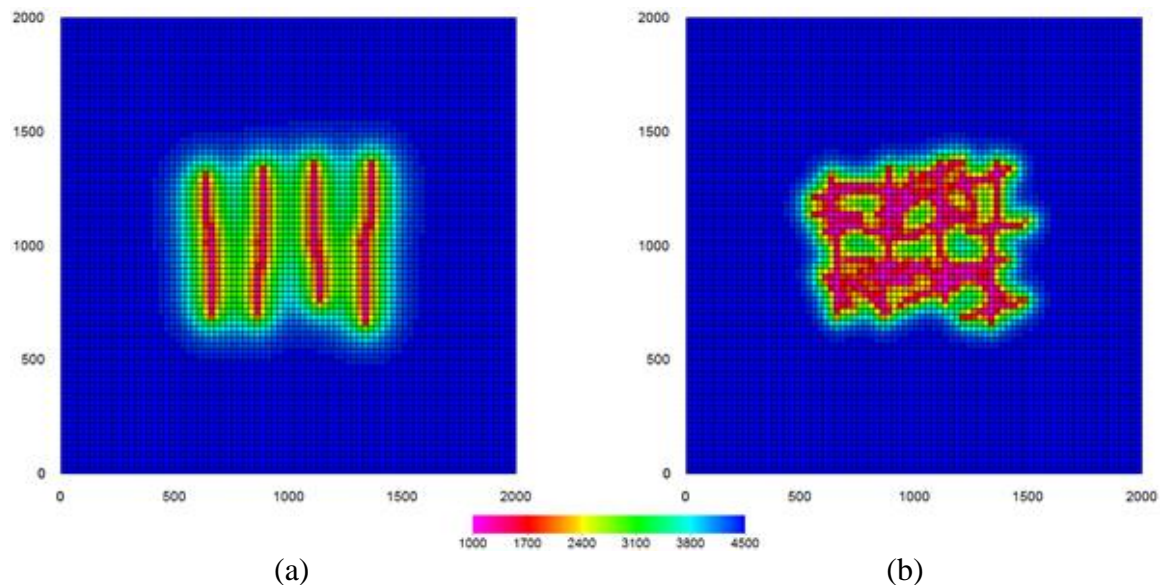


Figure 6.25: Pressure profiles for (a) the simple and (b) complex fracture networks after 3000 days. In this case, the rock matrix permeability is 50 nd.

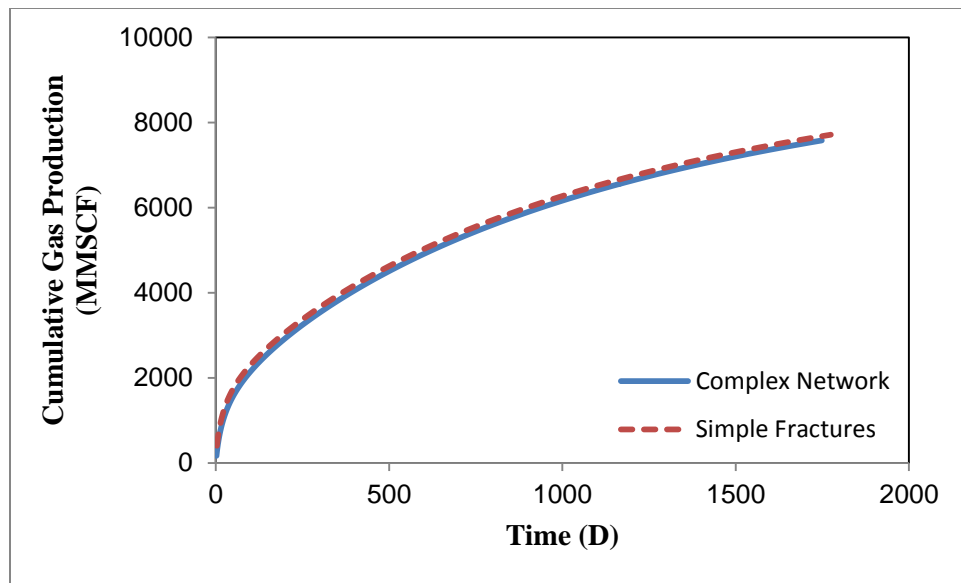


Figure 6.26: Cumulative gas production for the simple and complex fracture networks. In this case, the rock matrix permeability is  $50 \mu\text{d}$ .

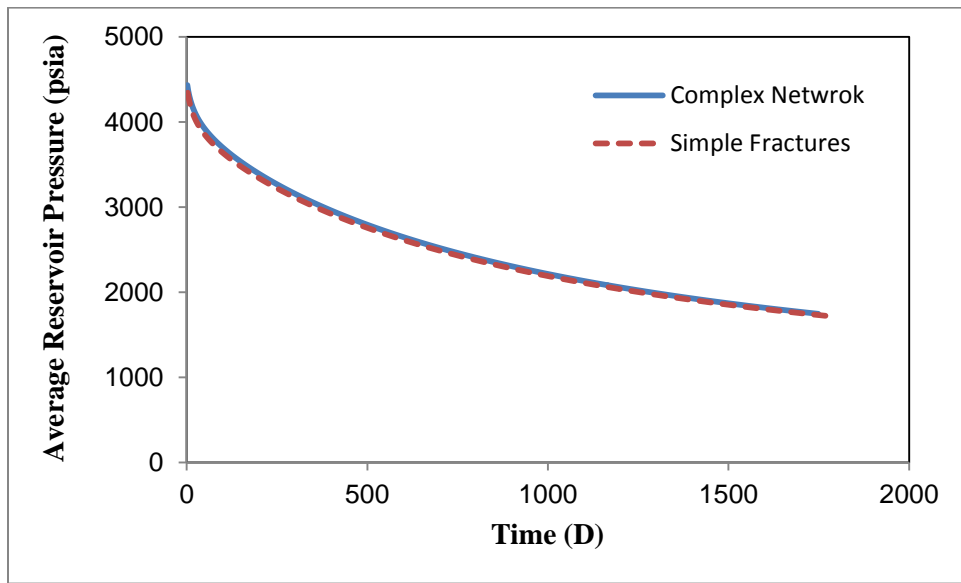


Figure 6.27: Average reservoir pressure versus time for the simple and complex fracture networks. In this case, the rock matrix permeability is  $50 \mu\text{d}$ .

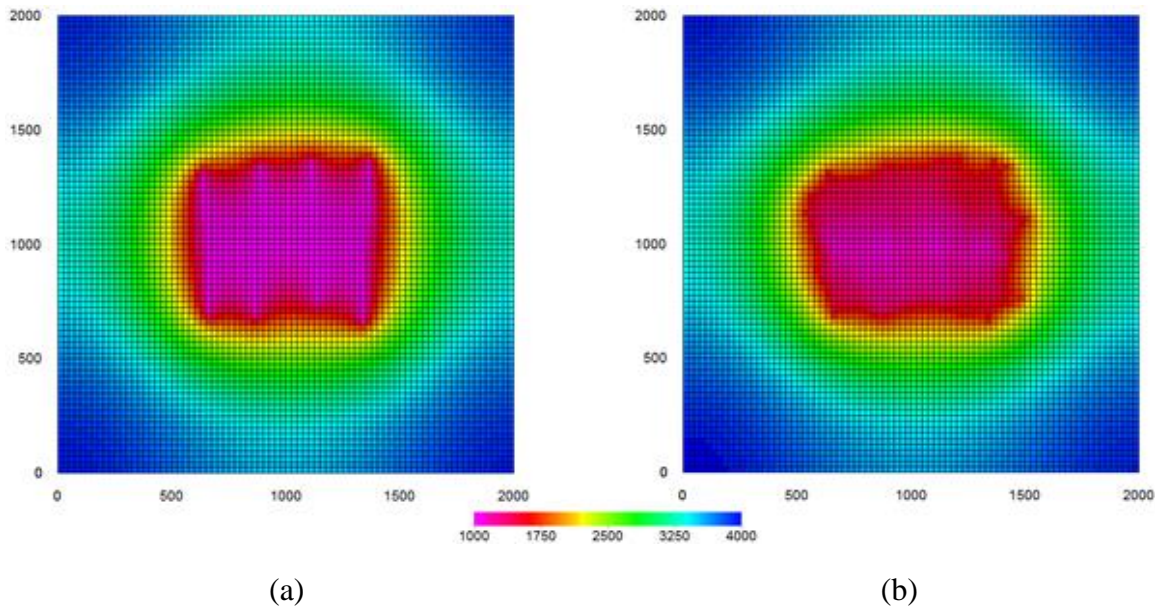


Figure 6.28: Pressure profiles for (a) the simple and (b) complex fracture networks after 400 days. In this case, the rock matrix permeability is  $50 \mu\text{d}$ .

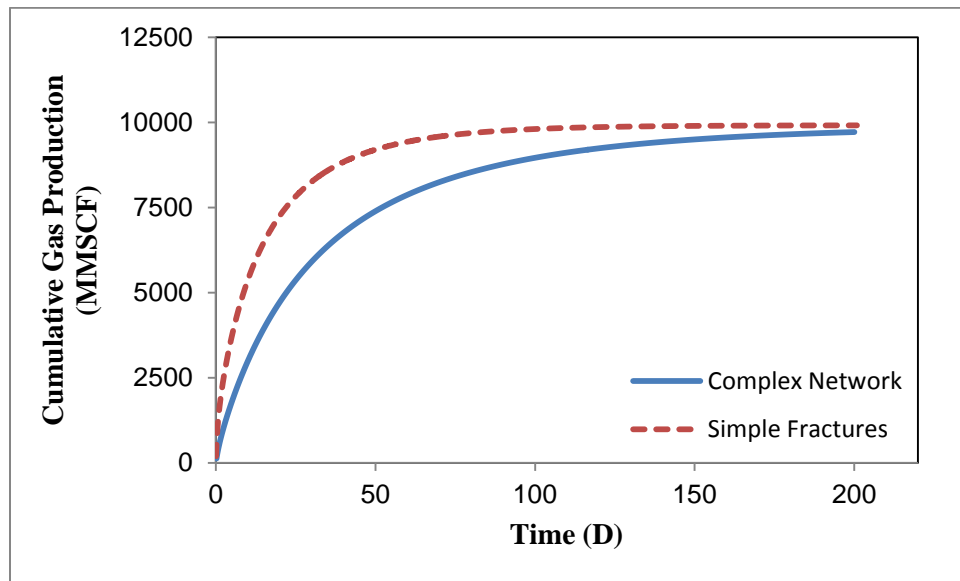


Figure 6.29: Cumulative gas production for the simple and complex fracture networks. In this case, the rock matrix permeability is  $5 \text{ md}$ .

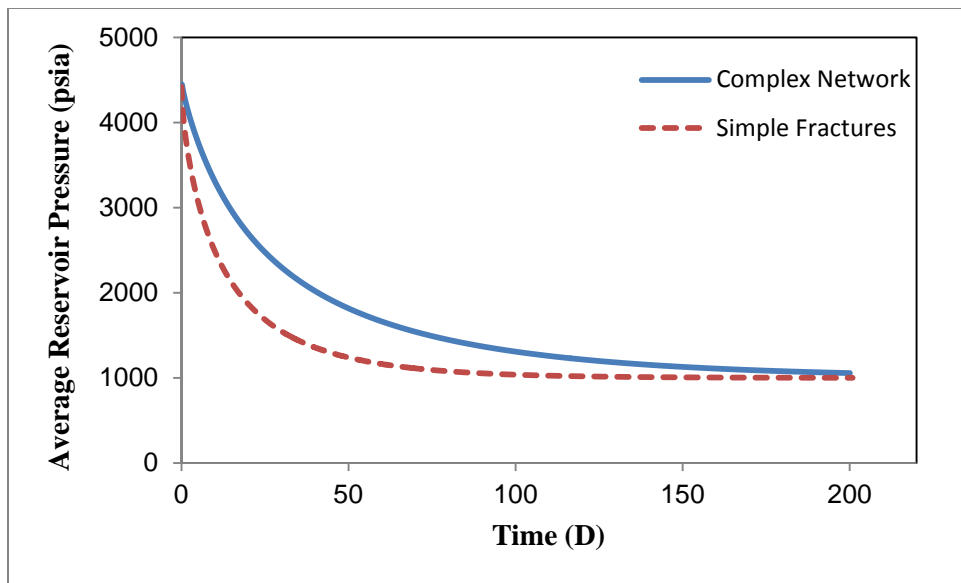


Figure 6.30: Average reservoir pressure versus time for the simple and complex fracture networks. In this case, the rock matrix permeability is 5 md.

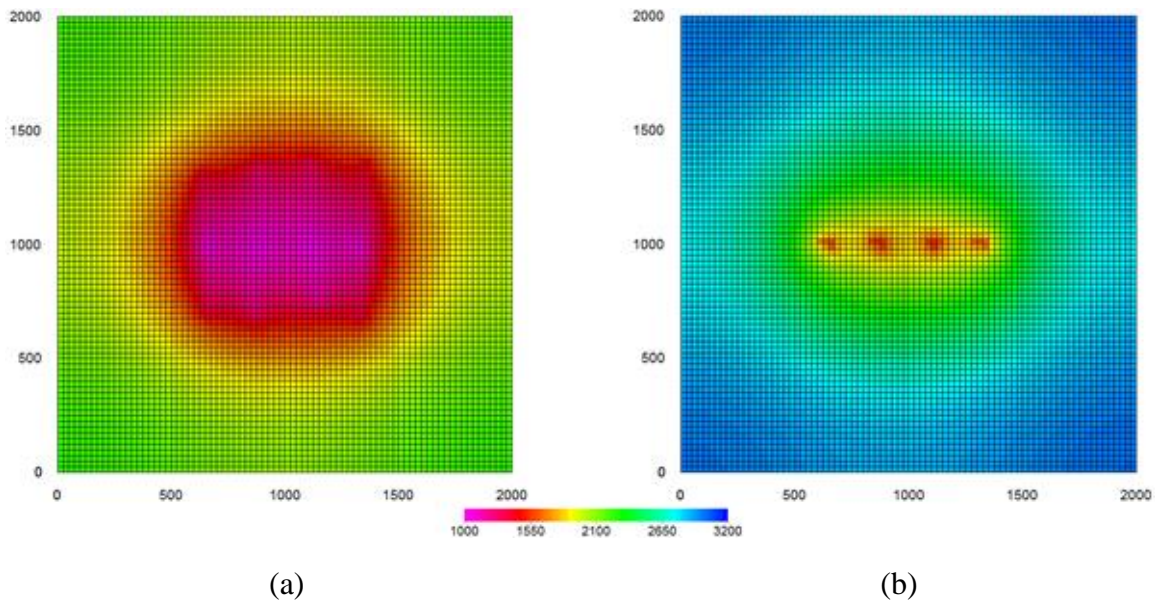


Figure 6.31: Pressure profiles for (a) the simple and (b) complex fracture networks after 400 days. In this case, the rock matrix permeability is 5 md.

### **6.3 INJECTION CONFORMANCE CONTROL**

Although creation of hydraulic fractures is an inevitable step for successful development of unconventional reservoirs, the existence of fractures and conduits is an unfavorable situation when water flooding is designed for a conventional reservoir. High conductivity fractures and conduits appear to localize the stream of displacing fluid and therefore leave a major part of reservoir intact by waterflood. As a remedy for this problem, a new technology called conformance control has developed. Conformance control consists of injection of carefully designed fluids such as polymer and polymer gels solutions to increase the sweep efficiency of water flooding via diverting the displacing fluid, water, to un-swept regions of the reservoir. This includes either blocking the high-perm zones and fractures, or decreasing the mobility ratio of the displacement process. To prepare the gel solutions, in addition to polymers, crosslinkers are required to further attach the polymer molecules together and form a high viscosity mixture. Gels have a much higher permeability reduction effect on high-perm zones compared to polymer solutions due to structure of their molecules. Also gels penetrate deeper into reservoir which allows access to farther regions for a more efficient treatment. To design an injection conformance control process, a detailed study of the behavior of gels solution under different conditions is required. It is essential to understand the impact of salinity, temperature, and water and oil compositions on the performance of the injected fluid. The gelation time, gel viscosity as a function of shear stress, gel strength, and gel adsorption are all the parameters needed to be accurately quantified before their direct application to a real field. In addition to laboratory core floods and experiments, reservoir simulations must be carried out to better understand the performance of gel solutions under different scenarios. UTGEL reservoir simulator, as mentioned in Chapter 3, has developed to model a variety of chemical flooding processes including conformance control using

several types of gel. There are different gelation types available in UTGEL such as Preformed Particle Gel (PPG), Colloidal Dispersion Gel (CDG), silicate gel, polymer/chromium chloride gel, and polymer/chromium malonate gel. In order to maximize the sweep efficiency of the water flood, in addition to studying gel quality, a detailed characterization of reservoir properties is vital. As presented in earlier sections of this chapter, the geometry and the configuration of fractures and channels have a substantial effect on the performance of the reservoir and the corresponding IOR processes. Thus, in designing a conformance control, characteristics of complex fractures and channels must be well understood as well in order to maximize the sweep efficiency of the waterflood by detecting un-swept zones. To achieve this goal, the EDFM approach has been added to UTGEL reservoir simulator as part of this research. UTGEL-EDFM simulator is capable of modeling a variety of chemical EOR methods including the conformance control in fractured reservoirs. In this chapter, to represent several applications of this reservoir simulator, a few case studies are presented. To do so, Preformed Particle Gel (PPG) is used as the gelation model. In the subsequent section, a brief discussion of permeability reduction factor and viscosity calculation for this type of gel is presented.

### **6.3.1 Preformed Particle Gel (PPG)**

Preformed particle gel (PPG) is a high temperature high salinity resistance gel formed on the surface using crosslinkers prior to injection (Bai *et al.* (2007) and (2008), and Taksaudom (2014)). This type of gel has higher strength and temperature tolerance compared to other types of polymers and microgels. PPG is specially applied to the reservoirs with high conductivity fractures and channels because of its large swelling

ratio. When this type of gel is injected into a reservoir, the permeability of high-perm zones is reduced significantly. This permeability reduction diverts the displacing fluid to intact portions of reservoir, such as low-perm layers. When modeling PPG in UTGEL, two parameters are evaluated for measuring their influence on fluid flow: permeability reduction factor and viscosity change.

### **6.3.1.1 Permeability Reduction Factor**

Permeability reduction occurs when gel particles enter a high-perm zone after swelling has occurred. The swelling ratio is defined based on Eq. (6.2), where  $SF$  is swelling factor,  $a_p$  and  $n_p$  are matching parameters, and  $C_{SEP}$  is effective salinity. This factor is used during simulation to calculate the size of gel particles.

$$SF = a_p (C_{SEP})^{n_p}. \quad (6.2)$$

If gel particles size is less than certain factors of pore diameter, gel can pass through the pore throat. To calculate the pore throat radius ( $r_h$ ), Eq. (6.3) is used, where  $\phi$  is porosity and  $\bar{k}$  is the average permeability given by Eq. (6.4). In the latter,  $u$  is velocity and  $k$  is absolute permeability given in different directions.

$$r_h = 1.15 \sqrt{\frac{8\bar{k}}{\phi}}. \quad (6.3)$$

$$\bar{k} = \left[ \frac{1}{k_x} \left( \frac{u_{x1}}{u_1} \right)^2 + \frac{1}{k_y} \left( \frac{u_{y1}}{u_1} \right)^2 + \frac{1}{k_z} \left( \frac{u_{z1}}{u_1} \right)^2 \right]^{-1}. \quad (6.4)$$

The permeability of the invaded cell is then modified by the factor given in Eq. (6.5), where  $R_{kfp}$  is the permeability reduction factor,  $a_{kp}$  and  $n_{kp}$  are matching parameters, and  $q$  is the flow rate.

$$R_{kfp} = a_{kp} q^{n_{kp}}. \quad (6.5)$$

### 6.3.1.2 Viscosity

The effective PPG viscosity ( $\mu_M$ ) at zero shear-rate is calculated by the Huggins equation (Shi *et al.* 2011) as a function of gel concentration in aqueous phase ( $C_{PPG}$ ) and solvent viscosity ( $\mu_s$ ). The other parameters in Eq. (6.6),  $A_{PPG,1}$  and  $A_{PPG,2}$ , are matching parameters for the model.

$$\mu_M = \mu_s \left[ 1 + A_{PPG,1} C_{PPG} + A_{PPG,2} C_{PPG}^2 \right]. \quad (6.6)$$

To include the effect of shear-rate on gel viscosity, Meter's equation is applied (Meter and Bird (1964)) where  $\mu_M^0$  is the microgel solution viscosity at zero shear-rate,  $P_\alpha$  and  $\dot{\gamma}_{1/2}$  are model parameters, and  $\dot{\gamma}_{eq}$  is the equivalent shear rate given by Eq. (6.8). In the latter,  $\dot{\gamma}_c$  is the shear-rate correction,  $|\mu_l|$  is the magnitude of flux for phase  $l$ ,  $k_{rl}$  is the relative permeability of phase  $l$ , and  $S_l$  is the saturation.

$$\mu_M = \mu_s + \frac{\mu_M^0 - \mu_s}{1 + \left( \frac{\dot{\gamma}_{eq}}{\dot{\gamma}_{1/2}} \right)^{P_\alpha - 1}}. \quad (6.7)$$

$$\dot{\gamma}_{eq} = \frac{\dot{\gamma}_c |\mu_l|}{\sqrt{\bar{k} k_{rl} \phi S_l}}. \quad (6.8)$$

For more details about PPG characteristics and modeling, one is referred to Taksaudom (2014). Also, for other types of gels, several models are available in UTGEL (Technical UTGEL V.01 (2013)) whose description is out of scope of this work. For the following case studies, PPG model is only employed.

### 6.3.2 PPG Injection Timing

When a conformance control is planned for a waterflood in a reservoir, it is crucial to determine the most optimum gel injection time. The goal is to block the high perm zones and divert water to un-swept regions before the water front reaches the producer wells. To do so, an accurate characterization of water invasion pattern is essential. The understanding of reservoir heterogeneity, and specifically the embedded high perm channels and fractures, can improve our ability to predict the water invasion profiles and thus to design an efficient conformance control job.

The objective of this section is to show the significance of PPG injection timing through the following case study. The example consists of a quarter of five-spot pattern with one injector and one producer located at the opposite corners. The reservoir and fluid properties are summarized in Table 6.3. A highly conductive channel, made of 4 vertical fractures, is inserted into the reservoir as shown in Figure 6.32. The permeability of fractures is 90000 md. This channel is intended to decrease the oil recovery through aggravating the water sweep efficiency. Four different schedules are studied for this problem. First, the entire waterflood is performed without conformance control. Then, in the next three scenarios, a 0.2 pore volume of PPG is injected along the water, but at different time windows. The injection schedules are summarized in Figure 6.33. From schedule-2 to schedule-4, the PPG injection is performed later after starting the

waterflood. PPG is injected at 1000 ppm concentration; for permeability reduction calculations based on Eq. (6.5),  $a_{kp}$  and  $n_{kp}$  are set to 30 and -3, respectively.

Figure 6.34 shows the incremental oil recovery for all of the scenarios after a total injection of 0.9 PV. As illustrated in this graph, when gel treatment is applied (schedules-2 to -4) higher oil recovery is achieved. However, although the same amount of PPG is injected into the reservoir in each conformance control treatment, different recovery improvements are achieved. For early PPG injection, recovery improvement is 12 percent while this number for late injection reduces to 8 percent. In fact, injection of PPG earlier in the process limits the water front movement in the high perm channel and improves the oil sweep efficiency. As shown in Figures 6.35 and 6.36, the schedule-2 results in higher oil production rate and lower water-cut. For this schedule, water breakthrough is delayed about 1100 days (0.14 PV) compared to schedule-1. In late treatment, although the water breakthrough time remains unchanged compared to schedule-1, a decrease is observed in water-cut after 5000 days (0.55 PV). Also, Figure 6.37 compares the water saturation profiles after 100 and 200 days. It is evident that the water front movement is constrained in the case of early PPG injection (Figure 6.37a). This is attributed to the diversion of water flow from the high-perm channel to the surrounding matrix gridblocks because of gel blockage in the fractures. Thus, water has reached the producer later and water-cut has remained the lowest among all the four cases. On the other hand, for the intermediate and late treatments, since the fractures have already been washed before PPG injection, the invasion profile is not affected by gel injection. However, because of high viscosity of the gel solution, the displacement efficiency is higher inside the swept zone which results in an increase in oil production when the oil bank reaches the producer (Figure 6.37b).

Overall Properties		Relative Permeability Curves for Matrix	
Matrix Porosity (fraction)	0.2	Irreducible Water Saturation	0.2
Matrix Permeability (md)	50	Water Rel. Perm. End Point	0.8
Channel Permeability (md)	90000	Water Rel. Perm. Exponent	4
Channel Aperture (ft)	0.1	Residual Oil Saturation	0.2
Initial Reservoir Pressure (psi)	3000	Oil Rel. Perm. End Point	0.7
Initial Water Saturation	0.2	Oil Rel. Perm. Exponent	2
Initial Oil Saturation	0.8	C <sub>10</sub> H <sub>22</sub> Properties	
Reservoir Temperature (°F)	60	Critical Pressure (psia)	350
Rock Compressibility (psi <sup>-1</sup> )	0	Critical Temperature (°R)	1500
Fluid Compressibility (psi <sup>-1</sup> )	0	Molecular Weight (lb/lb-mole)	142.23
Well Properties		Parachor	
Well Radius (ft)	0.25	Acentric Factor	0.488
Producer BHP (psi)	3000	Water Viscosity (cp)	1
Injector Rate (STB/D)	890	Oil Viscosity (cp)	5

Table 6.3: Rock and fluid properties of the reservoir model in section 6.3.2. The relative permeability curves are straight lines for the fractures.

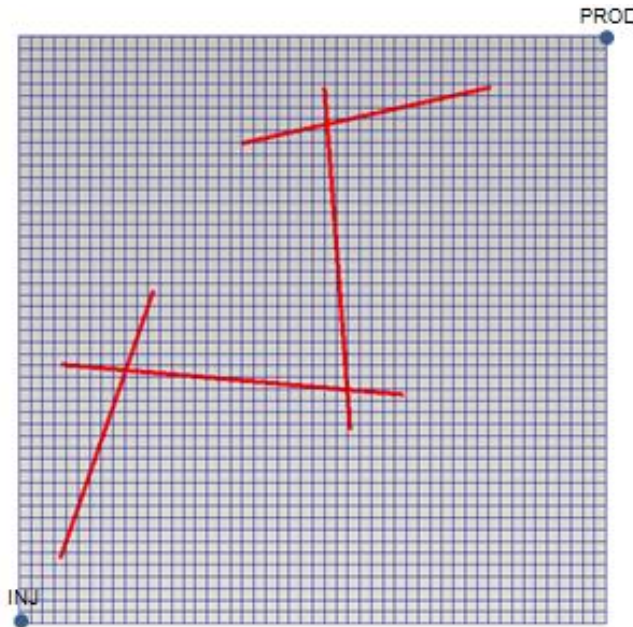


Figure 6.32: A reservoir model with a high conductivity channel made with 4 intersecting fracture planes.

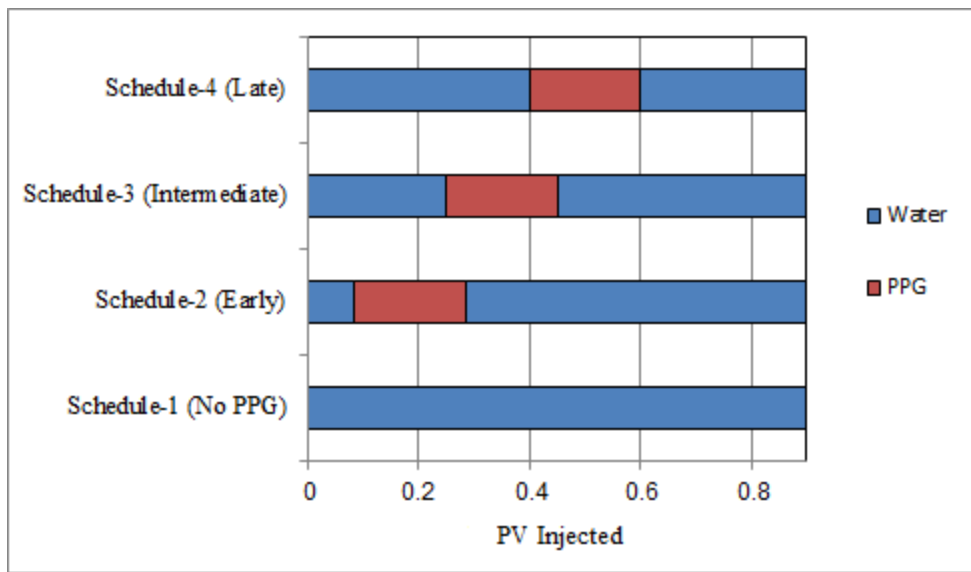


Figure 6.33: Injection schedules for the waterflood conformance control case study presented in section 6.3.2.

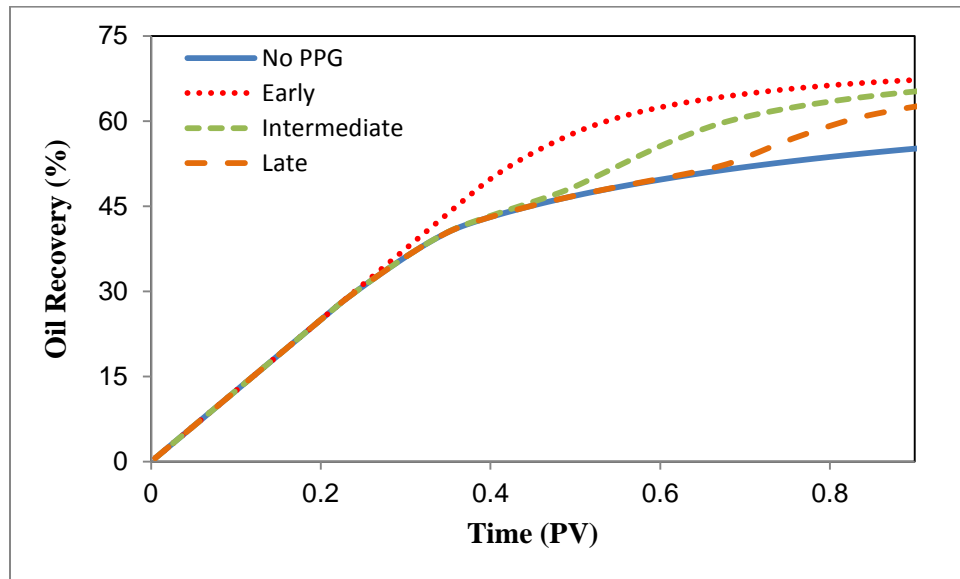


Figure 6.34: Oil recovery for PPG injection timing case study. The results are shown for early, intermediate, and late injections of PPG as well as no PPG treatment result.

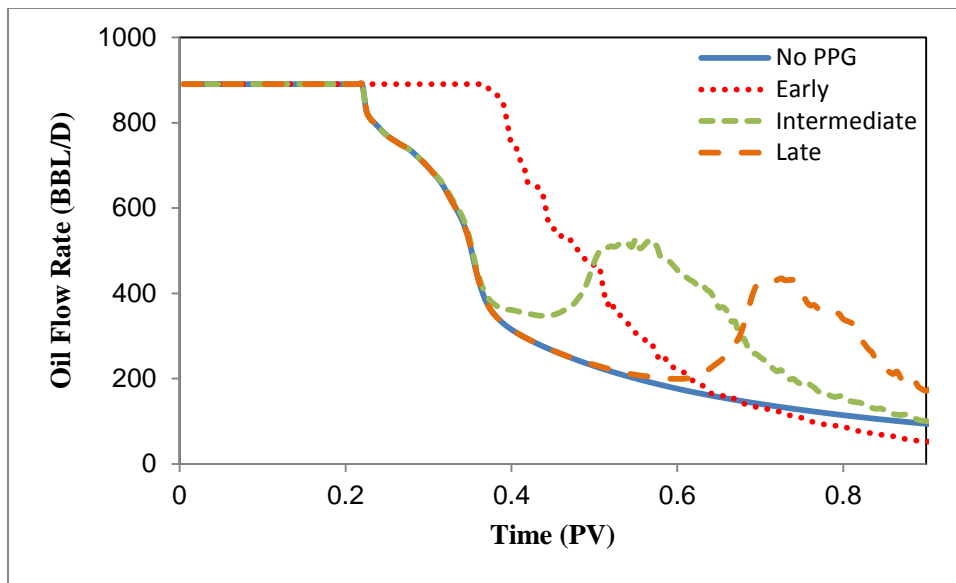


Figure 6.35: Oil production rates for PPG injection timing case study. The results are shown for early, intermediate, and late injections of PPG as well as no PPG treatment result.

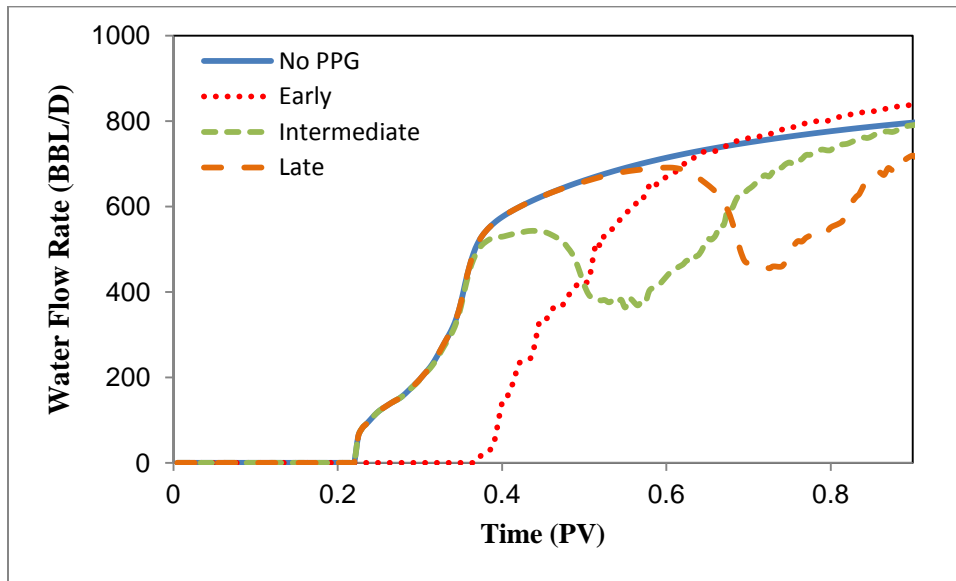
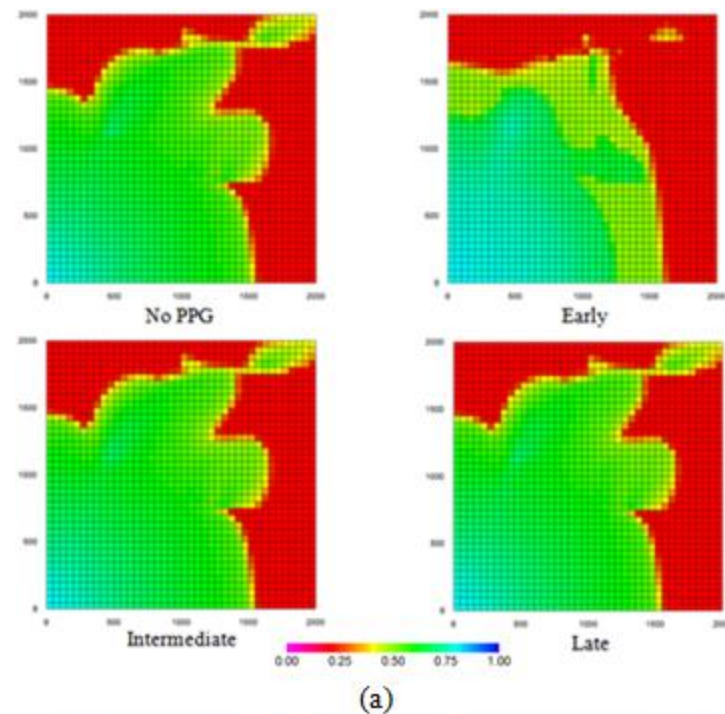
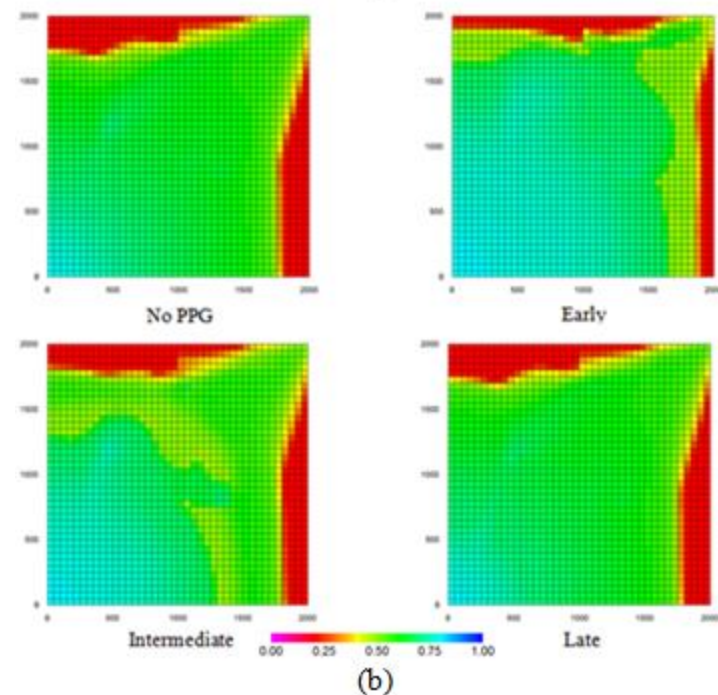


Figure 6.36: Water production rates for PPG injection timing case study. The results are shown for early, intermediate, and late injections of PPG as well as no PPG treatment result.



(a)



(b)

Figure 6.37: Water saturation profiles after (a) 0.25, and (b) 0.45 PV injection. In part (a), the PPG has only been injected in the “Early” scenario, while in part (b), the “Intermediate” injection has been performed as well.

### 6.3.3 PPG Concentration

For waterflood in heterogeneous reservoirs with noticeable contrast between rock matrix and channels permeabilities, higher viscosity and permeability reduction factor are required for gel solution. This can be achieved by adjusting PPG concentration (Eqs. (6.5) and (6.6)). The higher the gel concentration, the more conformance control is obtained. However, in terms of economics, an analysis must be made to understand whether higher gel concentrations could result in viable incremental oil recoveries. To do so, a comprehensive modeling tool is required to capture heterogeneous characteristics of the reservoir, such as fractures and channels, and to study their impact on the efficiency of conformance control. In the last section of this chapter, a case study is presented using UTGEL-EDFM to determine the effect of gel concentration on the vertical sweep efficiency of a waterflood process. The model reservoir as shown in Figure 6.38 is a three-dimensional problem comprising of 3 layers with different number of channels. The grid is  $30 \times 30 \times 3$  and the gridblock dimensions are 50, 50, and 150 ft in X-, Y-, and Z-directions, respectively. The arbitrary inclined channels, all with 50000 md permeability, are distributed into these layers such that the degree of complexity and heterogeneity increases from top to bottom. The red channel intersects all the formation as well as the injector well, while the blue and green fractures penetrate only one and two layers, respectively. Thus, the top, middle, and bottom layers have 1, 4, and 8 channels. The well pattern is an inverted five-spot where 5343 barrels of water are injected per day to reach 1 PV, and the BHP for the producers is 3000 psi. The injection schedule is 0.05, 0.25, and 0.3 PV of pre-treatment waterflood, gel injection, and post-treatment waterflood, respectively. The other properties are the same as ones given in Table 6.3, except for the matrix permeability which is 30 md.

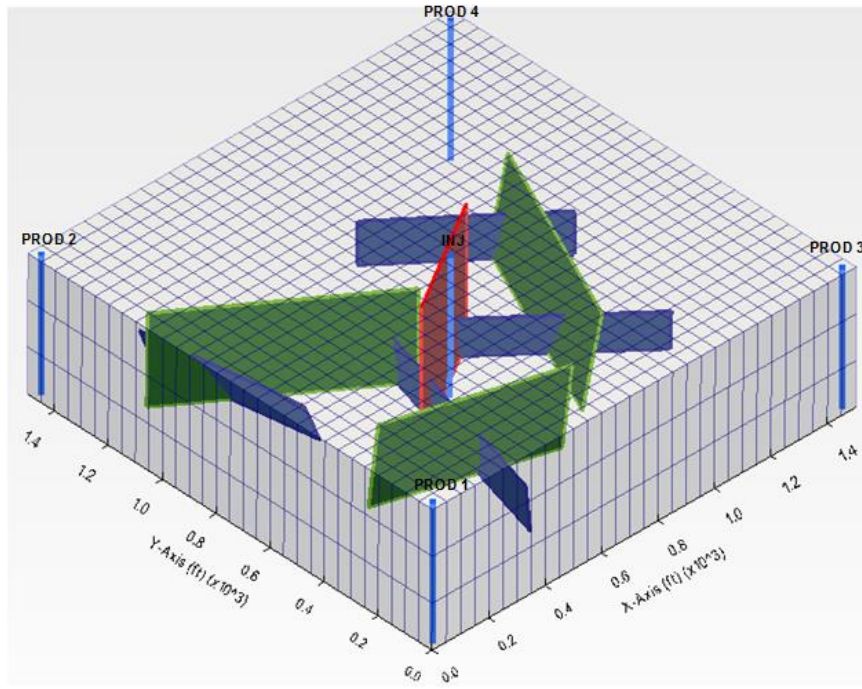


Figure 6.38: A reservoir model with 8 channels for the case study in section 6.3.3. The red channel intersects all the formation as well as the injector well while the blue and green fractures penetrate only one and two layers, respectively.

Three scenarios are studied to investigate the effect of PPG concentration on the performance of waterflood. First, the waterflood is performed without conformance control. Then, in the next two cases, 0.25 PV of gel solution is injected with different concentrations, 1000 and 4000 ppm. The gel concentration not only affects the viscosity calculations but also alters the permeability reduction factors. To calculate the reduction factors,  $a_{kp}$  and  $n_{kp}$  are set to 20 and -3, respectively. Figure 6.39 compares the incremental oil recoveries obtained from the waterflood and PPG treatments. It is observed that 11 and 15 percent increments in oil recovery are achieved due to injection of 1000 and 4000 ppm gel solutions, respectively. Moreover, gel solution not only reduces the total water production at producers as shown in Figure 6.40, but also

enhances the oil production (Figure 6.41) and the sweep efficiency by diverting the displacing fluid to un-swept regions. This fact is illustrated in water invasion profiles shown in Figure 6.42 as well. The profiles are shown after 1320 days (after almost 0.2 PV injection). It is clear that water channelings after PPG treatments are limited significantly due to blockages, and the sweep efficiency increases accordingly. These tasks are more efficiently carried out by the injection of 4000 ppm gel compared to the 1000 ppm concentration. In this study, the higher gel concentration results in extra 4 percent in oil recovery, which can be compared to the extra cost for solution preparation. On the other hand, if water production is examined for the producers, as shown in Figure 6.40, it is evident that higher gel concentration can reduce the produced water treatment cost by decreasing the water production. Thus, a detailed economic analysis must be made to assess the profitability of injecting an extra PPG along the solution.

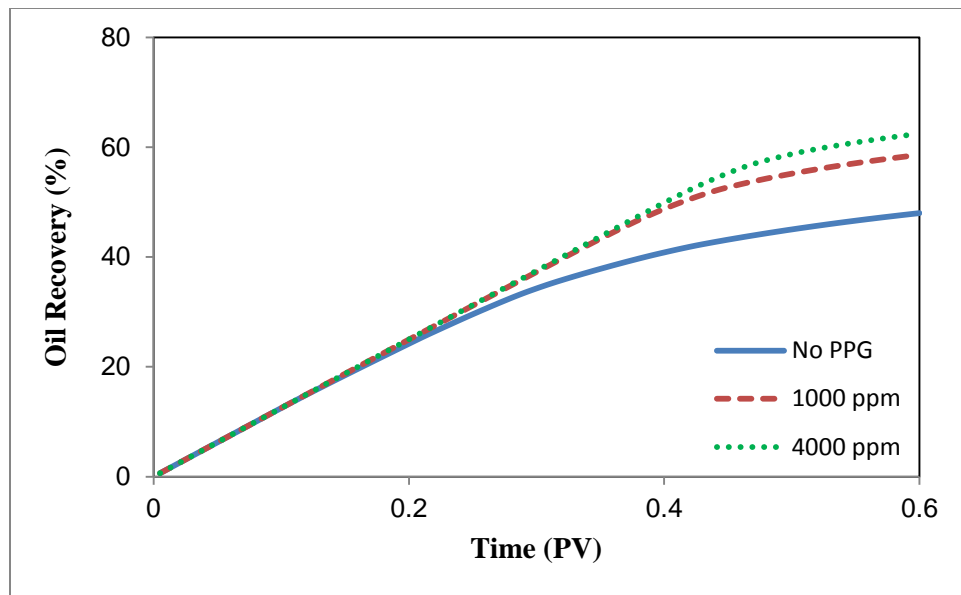


Figure 6.39: Oil recovery for the case study of section 6.3.3. The results are shown for 1000 and 4000 ppm as well as the waterflood with “No PPG”.

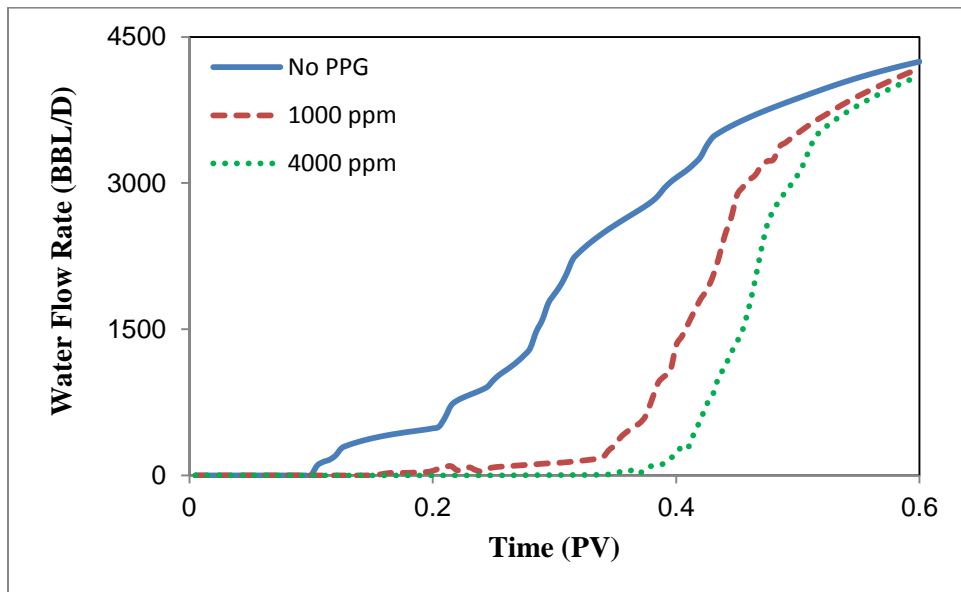


Figure 6.40: Water production rates for the case study of section 6.3.3. The results are shown for 1000 and 4000 ppm as well as the waterflood with “No PPG”.

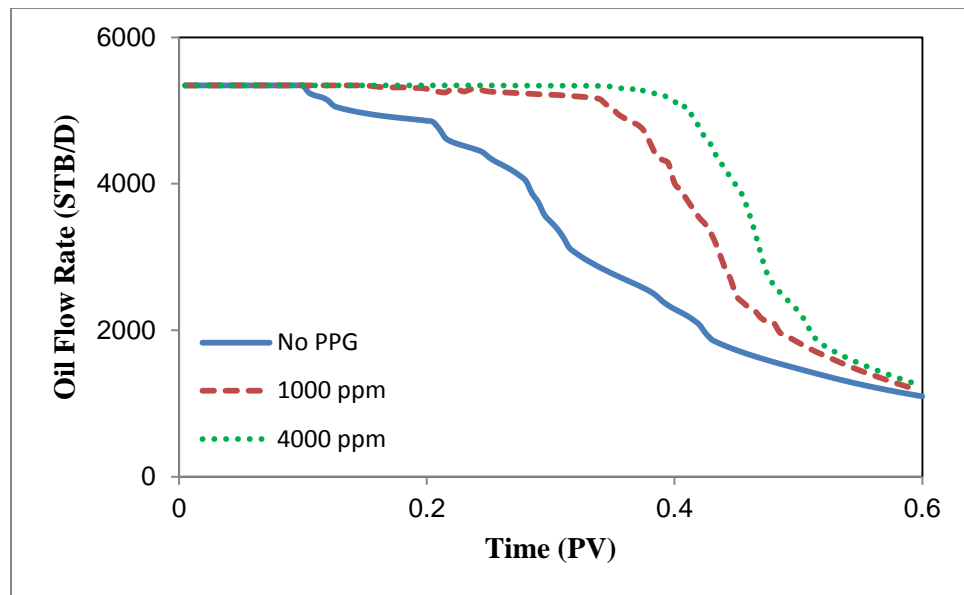


Figure 6.41: Oil production rates for the case study of section 6.3.3. The results are shown for 1000 and 4000 ppm as well as the waterflood with “No PPG”.

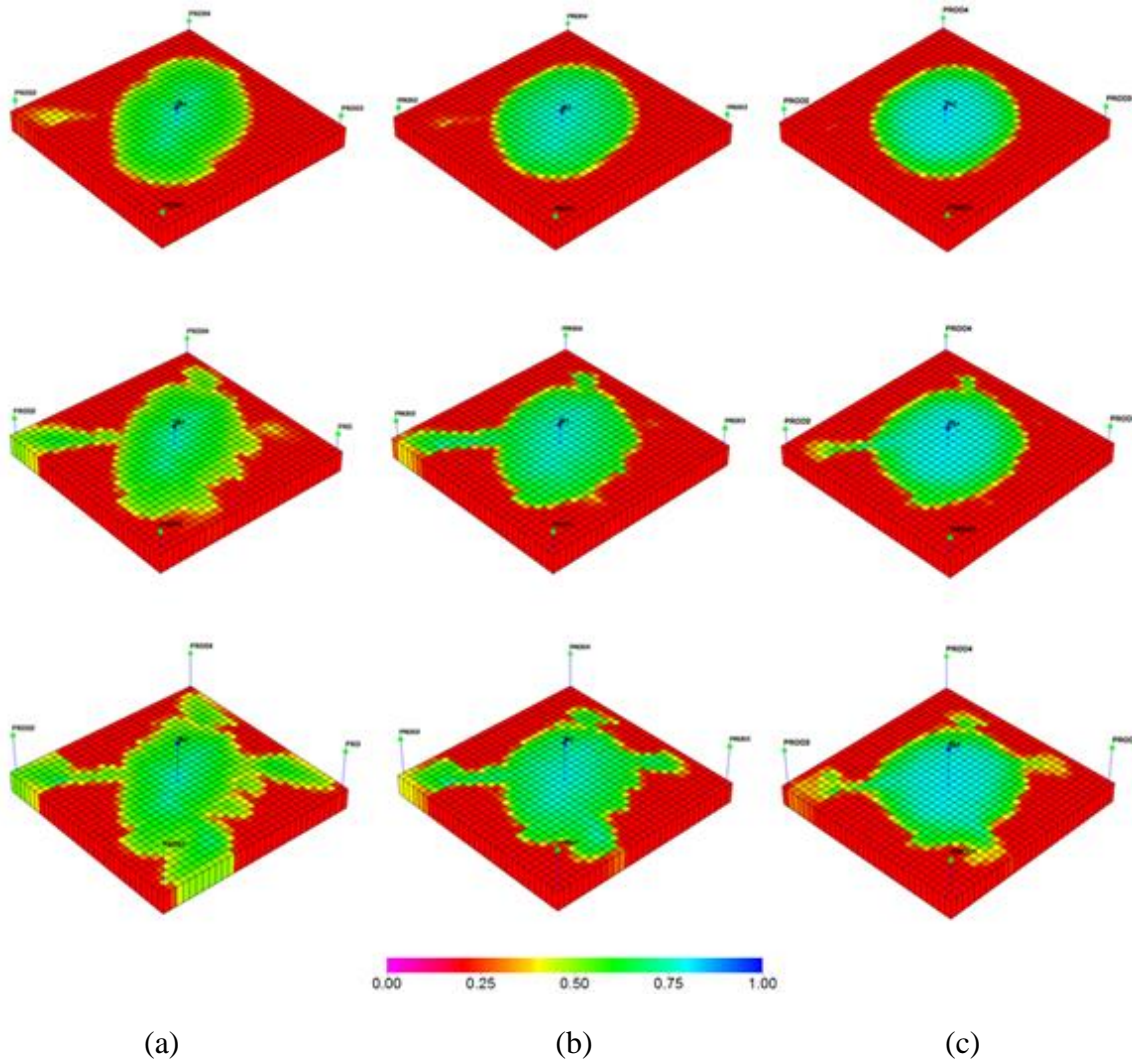


Figure 6.42: Water saturation profiles after 0.2 PV total injection for (a) waterflood with “No PPG”, (b) waterflood with injection of 1000 ppm gel, and (c) waterflood with injection of 4000 ppm gel. In each column, saturation profiles are shown for the 3 layers, starting from the top layer at the top to the bottom layer at the bottom.

## **Chapter 7: Summary, Conclusions, and Recommendations**

In this section, a summary of the chapters, as well as the conclusions for this work, is presented. Subsequently, the recommendations for future research are given.

### **7.1 SUMMARY AND CONCLUSIONS**

1. The Embedded Discrete Fracture Model (EDFM) was first developed by Li and Lee (2008), and later was extended by Moinfar (2013) to model slanted fractures with arbitrary orientations. EDFM combines the benefits of the dual continuum and discrete fracture models. In this approach, each fracture plane is embedded inside the matrix grid and intersects a number of the gridblocks. As a result, the fracture plane is discretized into several unstructured cells similar to DFM. However, the matrix domain remains structured and is composed of cubical cells. Thus, to capture the geometry of fractures, grid refinement in the vicinity of fractures is not required. Hence, accurate results can be obtained with much larger gridblocks compared to fine-grid simulations. The communications between matrix and fracture cells and also between fracture to fracture cells are then defined based on the definition of transmissibility factors developed by Li and Lee (2008) and Moinfar (2013).
2. The EDFM approach was implemented into The University of Texas in-house reservoir simulators UTCOMP and UTGEL, providing efficient and robust tools to study flow in complex fracture geometries and associated networks. Since UTCOMP and UTGEL reservoir simulators have been already geared with numerous models for studying primary, secondary, and enhanced oil recovery

- methods, the EDFM implementation creates a more realistic environment to investigate the behavior of fractured reservoirs and the performance of hydraulic fracturing job. To calculate transmissibility factors, a stand-alone preprocessing code was developed by Cavalcante Filho *et al.* (2015). The preprocessing code generates a list of non-neighboring connections and the corresponding properties to be used as extra input for the reservoir simulators.
3. UTCOMP-EDFM is capable of modeling a variety of Improved Oil Recovery methods (IOR) in fractured reservoirs, such as water flooding, miscible and immiscible gas injections for multiphase three-dimensional problems. Moreover, the UTCOMP-EDFM provides the capability to model complicated fracture networks with significant applications in hydraulic fracturing studies.
  4. Furthermore, UTGEL-EDFM is capable of modeling conformance control in reservoirs with complex high permeability channels and conduits. Studying other processes, such as polymer flooding and tracer flooding in fractured reservoirs, is available in UTGEL-EDFM as well.
  5. To implement EDFM in UTCOMP and UTGEL reservoir simulators, a novel method was designed in which the non-neighboring connections (NNC) were treated as additional dimensions. Since in conventional reservoir simulators the number of connections for every gridblock is limited to six, to account for fluid transfers between matrix and fracture cells, NNC concept was applied. To implement this concept in UTCOMP and UTGEL, the governing formulations were modified such that the fluid transfer through NNCs was computed using new directions, rather than X-, Y-, and Z-directions.
  6. To verify the accuracy of UTCOMP-EDFM and UTGEL-EDFM, several numerical simulation examples and one semi-analytical solution were performed.

First, the EDFM results were compared to a fine-grid simulation results. To do so, a reservoir model containing 3 vertical fractures was generated. Good agreement between EDFM and fine-grid results was observed while the simulation run times decreased 110 to 120 times. Next, to verify more complex fracture geometries, UTCOMP-EDFM and UTGEL-EDFM were compared against the earlier implementation of EDFM in GPAS reservoir simulator by Moinfar (2013). Two reservoir models with arbitrary oriented dip-angled fractures were studied. Again excellent agreement was observed. Finally, the implementation of well-fracture intersection was verified against a semi-analytical solution developed by Zhou *et al.* (2014) and Wei *et al.* (2014).

7. To show the capabilities and applications of UTCOMP-EDFM and UTGEL-EDFM, several case studies were presented. In the first part, the significance of the natural fracture networks on the performance of a reservoir model was investigated. The simulation outcomes indicated that considering the configuration of the background fracture networks can significantly improve the well placement design. Moreover, the role of capillary imbibition in oil production out of the water-wet reservoirs was evaluated for several fracture networks. It was observed that high capillary effects decrease the impact of fracture network on the reservoir performance.
8. UTCOMP-EDFM was also applied to study the hydraulic fractures efficiency. In this part, the effect of fracture network complexity on cumulative gas production was investigated. A sensitivity analysis was performed on rock matrix permeability to evaluate the performance of the created network in different conditions. It was observed that in a very tight formation, a complex network is preferred to infinite conductivity planar fractures. However, in moderate to high

permeability reservoirs, the creation of high conductivity primary fractures satisfies the purpose of the stimulation job.

9. The existence of highly conductive pathways such as channels, conduits, and fractures is not a favorable situation all the time. These features can deteriorate the efficiency of water flooding or cause problems for injector wells. Gel treatment is one of the remedies for this problem. UTGEL-EDFM was employed to investigate a few case studies in which PPG was injected to increase sweep efficiency. Several injection timings and several gel concentrations were specified for water flooding processes and their impact on oil recovery was evaluated henceforth. EDFM approach enabled consideration of more realistic channels and conduits compared to the conventional methods.

## 7.2 RECOMMENDATIONS

1. Implementation of the EDFM in the more general reservoir simulator, UTCHEM, enables investigation of a variety of chemical enhanced oil recovery methods in fractured reservoirs. Using the thermal feature of UTCHEM (Lashgari (2014)), one can study several production mechanisms in heavy oil fractured reservoirs.
2. Over the progress of this research, new features have been added to UTCOMP. Thus, we suggest that these new capabilities, such as modeling low salinity water injection (Kazemi Nia Korrani (2014)), to be added to the current version of UTCOMP-EDFM.
3. To further speedup simulation runs, implementation of the fully implicit formulation, especially for fracture cells, is suggested. The small control-volume of fracture cells often results in a significant increase in the simulation run time.

4. Transfer of pre-processing code to FORTRAN is a major recommendation. This eliminates the need for extra inputs and it further facilitates the simulation run process.
5. Incorporating EDFM with higher-order methods, available in UTCOMP, can increase the accuracy of simulations. This allows selection of larger matrix gridblocks which in turn improves the simulation run time.
6. Comparison of UTCOMP-EDFM and UTGEL-EDFM with real field data is suggested to verify their applicability in studying large-scale problems.

## Appendix: Semi-Analytical Solution

Based on Zhou *et al.* (2014), when a rectangular source is considered in a reservoir, the pressure drawdown for every point is calculated with Eq. (A-1), where  $p(x, y, z, t)$  is pressure at point  $(x, y, z)$  and time  $t$ ,  $U(t-t_0)$  is Heaviside's unit step function,  $\phi$  is porosity,  $c_t$  is total compressibility,  $a$  is reservoir length,  $b$  is reservoir width,  $q$  is the flux to the rectangular source,  $\eta$  is hydraulic diffusivity,  $\Theta_3$  is elliptic theta function of the third kind, and  $\Theta_3^I$  is integral of elliptic theta function. The rectangular source coordinates are  $(x_0, y_{01}, 0)$ ,  $(x_0, y_{02}, 0)$ ,  $(x_0, y_{01}, d)$ , and  $(x_0, y_{02}, d)$ .

$$\begin{aligned}
 p(x, y, z, t) = & \frac{U(t-t_0)}{2\phi c_t a} \int_0^{t-t_0} q(t-t_0-\tau) \\
 & \times \left\{ \Theta_3 \left[ \frac{\pi(x-x_0)}{2a}, e^{-\left(\frac{\pi}{b}\right)^2 \eta_x \tau} \right] + \Theta_3 \left[ \frac{\pi(x+x_0)}{2a}, e^{-\left(\frac{\pi}{b}\right)^2 \eta_x \tau} \right] \right\} \\
 & \times \left\{ \Theta_3^I \left[ \frac{\pi(y-y_{01})}{2b}, e^{-\left(\frac{\pi}{b}\right)^2 \eta_y \tau} \right] + \Theta_3^I \left[ \frac{\pi(y+y_{01})}{2b}, e^{-\left(\frac{\pi}{b}\right)^2 \eta_y \tau} \right] \right\} \\
 & \times \left\{ +\Theta_3^I \left[ \frac{\pi(y-y_{02})}{2b}, e^{-\left(\frac{\pi}{b}\right)^2 \eta_y \tau} \right] + \Theta_3^I \left[ \frac{\pi(y+y_{02})}{2b}, e^{-\left(\frac{\pi}{b}\right)^2 \eta_y \tau} \right] \right\} \\
 & \times \left\{ 2\Theta_3^I \left[ \frac{\pi z}{2b}, e^{-\left(\frac{\pi}{b}\right)^2 \eta_y \tau} \right] + \Theta_3^I \left[ \frac{\pi(z-d)}{2d}, e^{-\left(\frac{\pi}{b}\right)^2 \eta_y \tau} \right] \right\} d\tau. \tag{A-1}
 \end{aligned}$$

The elliptic theta function of the third kind and its integral are

$$\Theta_3(\pi x, e^{-2\pi^2 t}) = \begin{cases} 1 + 2 \sum_{n=1}^{\infty} e^{-2n^2\pi^2 t} \cos(2n\pi x) & \text{for } e^{-2\pi^2 t} < \frac{1}{\pi} \\ \frac{1}{\sqrt{\pi t}} \sum_{n=-\infty}^{+\infty} e^{-\frac{(x+n)^2}{t}} & \text{for } e^{-2\pi^2 t} \geq \frac{1}{\pi} \end{cases}, \quad (\text{A-2})$$

and

$$\Theta_3^f(\pi x, e^{-2\pi^2 t}) = \int_0^x \Theta_3(\pi x', e^{-2\pi^2 t}) dx' = \begin{cases} x + \frac{1}{\pi} \sum_{n=1}^{+\infty} \frac{e^{-n^2\pi^2 t}}{n} \sin(2n\pi x) & \text{for } e^{-2\pi^2 t} < \frac{1}{\pi} \\ \frac{1}{2} \sum_{n=-\infty}^{+\infty} \left[ \operatorname{erf}\left(\frac{x+n}{\sqrt{t}}\right) - \operatorname{erf}\left(\frac{n}{\sqrt{t}}\right) \right] & \text{for } e^{-2\pi^2 t} \geq \frac{1}{\pi} \end{cases}. \quad (\text{A-3})$$

When there are multiple fractures, non-aligned with major coordinates, the superposition concept is applied to calculate pressure drawdown as

$$p(x, y, z, t) = \frac{U(t-t_0)}{4\phi c_t ab} \int_0^{t-t_0} q_j(t-t_0-\tau) G_j(x, y, z, t) d\tau, \quad (\text{A-4})$$

where

$$\begin{aligned}
G_j(x, y, z, t) = & \int_0^{x_{j2}-x_{j1}} q_j(t-t_0-\tau) \\
& \times \left[ \Theta_3 \left\{ \frac{\pi[x-(x_{j1}+x')]^2}{2a}, e^{-\left(\frac{\pi}{a}\right)^2 \eta_x \tau} \right\} + \Theta_3 \left\{ \frac{\pi[x+(x_{j1}+x')]^2}{2a}, e^{-\left(\frac{\pi}{a}\right)^2 \eta_x \tau} \right\} \right] \\
& \times \left[ \Theta_3 \left\{ \frac{\pi[y-(x_{j1}+x') \tan \theta_j]^2}{2b}, e^{-\left(\frac{\pi}{a}\right)^2 \eta_y \tau} \right\} + \Theta_3 \left\{ \frac{\pi[y+(x_{j1}+x') \tan \theta_j]^2}{2b}, e^{-\left(\frac{\pi}{a}\right)^2 \eta_y \tau} \right\} \right] \\
& \times \left\{ 2\Theta_3 \left[ \frac{\pi z}{2b}, e^{-\left(\frac{\pi}{b}\right)^2 \eta_y \tau} \right] + \Theta_3 \left[ \frac{\pi(z-d)}{2d}, e^{-\left(\frac{\pi}{b}\right)^2 \eta_y \tau} \right] \right. \\
& \left. + \Theta_3 \left[ \frac{\pi(z+d)}{2d}, e^{-\left(\frac{\pi}{b}\right)^2 \eta_y \tau} \right] \right\} dx' d\tau.
\end{aligned} \tag{A-5}$$

## References

- Aguilera, R. (1995), *Naturally Fractured Reservoirs*, Second Edition, PennWell Publishing Company.
- Aldejain, A.A. (1999), Implementation of Dual-Porosity Model in a Chemical Flooding Simulator, PhD Dissertation, The University of Texas at Austin.
- Baca, R.G., Arnett, R.C., and Langford, D.W. (1984), Modelling Fluid Flow in Fractured Porous Rock Masses by Finite-Element Techniques, *International Journal for Numerical Methods in Fluids*, 4(04), 337-348.
- Bai, B., Huang, F., Liu, Y., Seright, R.S., and Wang, Y. (2008), Case Study on Preformed Particle Gel for In-Depth Fluid Diversion, SPE 113997, SPE Symposium on Improved Oil Recovery, Tulsa, Oklahoma, USA, 20-23 April.
- Bai, B., Li, L., Liu, Y., Liu, H., Wang, Z., and You, C. (2007), Preformed Particle Gel for Conformance Control: Factors Affecting its Properties and Applications, *SPE Reservoir Evaluation and Engineering*, 10(04), 415-422.
- Baliga, B.R. and Patankar, S.V. (1980), A New Finite-Element Formulation for Convection-Diffusion Problems, *Numerical Heat Transfer*, 3(04), 393-409.
- Barenblatt, G.I., Zheltov, I.P., and Kochina, I.N. (1960), Basic Concepts in the Theory of Seepage of Homogeneous Liquids in Fissured Rocks [Strata], *Journal of applied mathematics and mechanics*, 24(05), 1286-1303.
- Bhuyan, D., Lake, L.W., and Pope, G.A. (1990), Mathematical Modeling of High-pH Chemical Flooding, *SPE Reservoir Engineering*, 5(02), 213-220.
- Cavalcante Filho, J.S.A., Shakiba, M., Moinfar, A., and Sepehrnoori, K. (2015), Implementation of a Preprocessor for Embedded Discrete Fracture Modeling in an IMPEC Compositional Reservoir Simulator, SPE 173289, SPE Reservoir Simulation Symposium, Houston, Texas, USA, 23-25 February.
- Chang, Y.B. (1990), Development and Application of an Equation of State Compositional Simulator, PhD Dissertation, The University of Texas at Austin.

- Chen, C.C. and Raghavan, R. (1997), A Multiply-Fractured Horizontal Well in a Rectangular Drainage Region, *SPE Journal*, 2(04), 455-465.
- Chen, J. (1993), New Approaches to Dual Porosity Modeling of Waterflooding in Naturally Fractured Reservoirs, PhD Dissertation, The University of Texas at Austin.
- Cinco L.H., Samaniego V.F., and Dominguez A.N. (1978), Transient Pressure Behavior for a Well with a Finite-Conductivity Vertical Fracture, *SPE Journal*, 18(04), 253-264.
- Cipolla, C.L., Warpinski, N.R., Mayerhofer, M., Lolon, E.P., and Vincent, M. (2010), The Relationship Between Fracture Complexity Reservoir Properties and Fracture-Treatment Design, *SPE Production and Operations*, 25(04), 438-452.
- Coats, K.H. (1989), Implicit Compositional Simulation of Single-Porosity and Dual-Porosity Reservoirs, SPE 18427, SPE Symposium on Reservoir Simulation, Houston, Texas, USA, 6-8 February.
- Coats, K.H., Dempsey, J.R., and Henderson, J.H. (1971), The Use of Vertical Equilibrium in Two-Dimensional Simulation of Three-Dimensional Reservoir Performance, *SPE Journal*, 11(01), 63-71.
- Datta Gupta, A. (1986), Three-Dimensional Simulation of Chemical Flooding, PhD Dissertation, The University of Texas at Austin.
- De Swaan O.A. (1976), Analytic Solutions for Determining Naturally Fractured Reservoir Properties by Well Testing, *SPE Journal*, 16(03), 117-122.
- Dean, R.H. and Lo, L. (1988), Simulations of Naturally Fractured Reservoirs, *SPE Reservoir Engineering*, 3(02), 638-648.
- Fu, Y., Yang, Y.K., and Deo M.D. (2005), Three-Dimensional, Three-Phase Discrete-Fracture Reservoir Simulator Based on Control Volume Finite Element (CVFE) Formulation, SPE 93292, SPE Reservoir Simulation Symposium, Houston, Texas, USA, January 31- February 2.
- Gilman, J.R. (1986), An Efficient Finite-Difference Method for Simulating Phase Segregation in the Matrix Blocks in Double-Porosity Reservoirs, *SPE Reservoir Engineering*, 1(04), 403-413.

- Gilman, J.R. and Kazemi, H. (1983), Improvements in Simulation of Naturally Fractured Reservoirs, *SPE Journal*, 23(04), 695-707.
- Hajibeygi, H., Karvounis, D., and Jenny, P. (2011), A Hierarchical Fracture Model for the Iterative Multi-Scale Finite Volume Method, *Journal of Computational Physics*, 230(24), 8729-8743.
- Hill, A.C. and Thomas, G.W. (1985), A New Approach for Simulating Complex Fractured Reservoirs, SPE 13537, Middle East Oil Technical Conference and Exhibition, Bahrain, 11-14 March.
- Hoteit, H. and Firoozabadi, A. (2005), Multicomponent Fluid Flow by Discontinuous Galerkin and Mixed Methods in Unfractured and Fractured Media, *Water Resources Research*, 41(11).
- Juanes, R., Samper, J., and Molinero, J. (2002), A General and Efficient Formulation of Fractures and Boundary Conditions in the Finite-Element Method, *International Journal for Numerical Methods in Engineering*, 54(12), 1751-1774.
- Karimi-Fard, M. and Firoozabadi, A. (2003), Numerical Simulation of Water Injection in Fractured Media using the Discrete-Fracture Model and the Galerkin Method, *SPE Reservoir Evaluation and Engineering*, 6(02), 117-126.
- Karimi-Fard, M., Durlofsky, L.J., and Aziz, K. (2004), An Efficient Discrete-Fracture Model Applicable for General-Purpose Reservoir Simulators, *SPE Journal*, 9(02), 227-236.
- Kazemi Nia Korrani, A. (2014), Mechanistic Modeling of Low Salinity Water Injection, PhD Dissertation, The University of Texas at Austin.
- Kazemi, H. (1969), Pressure Transient Analysis of Naturally Fractured Reservoirs with Uniform Fracture Distribution, *SPE Journal*, 9(04), 451-462.
- Kazemi, H. and Merrill, L.S. (1979), Numerical Simulation of Water Imbibition in Fractured Cores, *SPE Journal*, 19(03), 175-182.
- Kazemi, H., Merrill, L.S., Porterfield, K.L., and Zeman, P.R. (1976), Numerical Simulation of Water-Oil Flow in Naturally Fractured Reservoirs, *SPE Journal*, 16(06), 317-326.

- Kim, J.G. and Deo, M.D. (2000), Finite Element Discrete-Fracture Model for Multiphase Flow in Porous Media, *AICHE Journal*, 46(6), 1120-1130.
- Lake, L.W., Carey, G.F., Pope, G.A., and Sepehrnoori, K. (1984), Isothermal Multiphase Multicomponent Fluid Flow in Permeable Media Part 1: Description and Mathematical Formulation, *In Situ*, 8(1), 1-40.
- Lashgari, H. (2014), Development of a Four-Phase Thermal-Chemical Reservoir Simulator for Heavy Oil, PhD Dissertation, The University of Texas at Austin.
- Lee, S.H., Jensen, C.L., and Lough, M.F. (2000), Efficient Finite-Difference Model for Flow in a Reservoir With Multiple Length-Scale Fractures, *SPE Journal*, 5(03), 268-275.
- Lee, S.H., Lough, M.F., and Jensen, C.L. (2001), Hierarchical Modeling of Flow in Naturally Fractured Formations with Multiple Length Scales, *Water Resources Research*, 37(3), 443-455.
- Li, L. and Lee, S.H. (2008), Efficient Field-Scale Simulation of Black Oil in a Naturally Fractured Reservoir through Discrete Fracture Networks and Homogenized Media, *SPE Reservoir Evaluation and Engineering*, 11(04), 750-758.
- Litvak, B.L. (1985), Simulation and Characterization of Naturally Fractured Reservoirs, Reservoir Characterization Technical Conference, Dallas, Texas, USA, April 29 – May 1.
- Long, J.C.S. and Witherspoon, P.A. (1985), The Relationship of the Degree of Interconnection to Permeability in Fracture Networks, *Journal of Geophysical Research: Solid Earth (1978–2012)*, 90(B4), 3087-3098.
- Long, J.C.S., Remer, J.S., Wilson, C.R., and Witherspoon, P.A. (1982), Porous Media Equivalents for Networks of Discontinuous Fractures, *Water Resources Research*, 18(3), 645-658.
- Mayerhofer, M.J., Lolon, E.P., Youngblood, J.E., and Heinze, J.R. (2006), Integration of Microseismic-Fracture-Mapping Results with Numerical Fracture Network Production Modeling in the Barnett Shale, SPE Annual Technical Conference and Exhibition, San Antonio, Texas, USA, 24-27 September.

- Meter, D.M., and Bird, R.B. (1964), Tube Flow of Non-Newtonian Polymer Solutions: PART I: Laminar Flow and Rheological Models, *AICHE Journal*, 10(6), 878-881.
- Moinfar, A. (2013), Development of an Efficient Embedded Discrete Fracture Model for 3D Compositional Reservoir Simulation in Fractured Reservoirs, PhD Dissertation, The University of Texas at Austin.
- Moinfar, A., Varavei, A., Sepehrnoori, K., and Johns, R.T. (2012), Development of a Novel and Computationally-Efficient Discrete-Fracture Model to Study IOR Processes in Naturally Fractured Reservoirs, SPE 154246, SPE Improved Oil Recovery Symposium, Tulsa, Oklahoma, USA, 14-18 February.
- Moinfar, A., Varavei, A., Sepehrnoori, K., and Johns, R.T. (2014), Development of an Efficient Embedded Discrete Fracture Model for 3D Compositional Reservoir Simulation in Fractured Reservoirs, *SPE Journal*, 19(02), 289-303.
- Monteagudo, J.E.P. and Firoozabadi, A. (2004), Control-Volume Method for Numerical Simulation of Two-Phase Immiscible Flow in Two- and Three-Dimensional Discrete-Fractured Media, *Water Resources Research*, 40(7).
- Naimi-Tajdar, R., Han, C., Sepehrnoori, K., Arbogast, T.J., and Miller, M.A. (2007), A Fully Implicit Compositional Parallel Simulator for IOR Processes in Fractured Reservoirs, *SPE Journal*, 12(03), 367-381.
- Noorishad, J. and Mehran, M. (1982), An Upstream Finite Element Method for Solution of Transient Transport Equation in Fractured Porous Media, *Water Resources Research*, 18(3), 588-596.
- Odeh, A.S. (1965), Unsteady-State Behavior of Naturally Fractured Reservoirs, *SPE Journal*, 5(01), 60-66.
- Paluszny, A., Matthäi, S.K., and Hohmeyer, M. (2007), Hybrid Finite Element–Finite Volume Discretization of Complex Geologic Structures and a New Simulation Workflow Demonstrated on Fractured Rocks, *Geofluids*, 7(2), 186-208.
- Peaceman, D.W. (1983), Interpretation of Well-Block Pressures in Numerical Reservoir Simulation with Nonsquare Grid Blocks and Anisotropic Permeability, *SPE Journal*, 23(03), 531-543.

- Pruess, K. and Narasimhan, T.N. (1985), A Practical Method for Modeling Fluid and Heat Flow in Fractured Porous Media, *SPE Journal*, 25(01), 14-26.
- Rahimi Zeynal, A., Snelling, P., Neuhaus, C.W., and Mueller, M. (2014), Correlation of Stimulated Rock Volume from Microseismic Pointsets to Production Data - A Horn River Case Study, SPE 169541, SPE Western North American and Rocky Mountain Joint Meeting, Denver, Colorado, USA, 17-18 April.
- Rossen, R.H. (1977), Simulation of Naturally Fractured Reservoirs with Semi-Implicit Source Terms, *SPE Journal*, 17(03), 201-210.
- Rossen, R.H. and Shen, E.I. (1989), Simulation of Gas-Oil Drainage and Water-Oil Imbibition in Naturally Fractured Reservoirs, *SPE Reservoir Engineering*, 4(04), 464-470.
- Saad, N. (1989), Field Scale Studies with a 3D Chemical Flooding Simulator, PhD Dissertation, The University of Texas at Austin.
- Saidi, A.M. (1983), Simulation of Naturally Fractured Reservoirs, SPE 12270, SPE Reservoir Simulation Symposium, San Francisco, CA, USA, 15-18 November.
- Saidi, A.M. (1987), *Reservoir Engineering of Fractured Reservoirs: Fundamental and Practical Aspects*, Total Edition Presse.
- Shi, J., Varavei, A., Huh, C., Delshad, M., Sepehrnoori, K., and Li, X. (2011), Viscosity Model of Preformed Microgels for Conformance and Mobility Control, *Energy & Fuels*, 25(11), 5033-5037.
- Sonier, F., Souillard, P., and Blaskovich, F.T. (1988), Numerical Simulation of Naturally Fractured Reservoirs, *SPE Reservoir Engineering*, 3(4), 1114-1122.
- Taksaudom, P. (2014), Simulation Study of Preformed Particle Gel for Conformance Control, MS Thesis, The University of Texas at Austin.
- Tarahhom, F. (2008), Development of an Implicit Full-Tensor Dual Porosity Compositional Reservoir Simulator, PhD Dissertation, The University of Texas at Austin.
- Thambynayagam, R.M. (2011). *The diffusion handbook: Applied solutions for engineers*, McGraw Hill Professional.

- Therrien, R. and Sudicky, E.A. (1996), Three-Dimensional Analysis of Variably-Saturated Flow and Solute Transport in Discretely-Fractured Porous Media, *Journal of Contaminant Hydrology*, 23(1), 1-44.
- Thomas, L.K., Dixon, T., and Pierson, R.G. (1983), Fractured Reservoir Simulation, *SPE Journal*, 23(01), 42-54.
- UTCHEM Technical Documentation 9 (2000), The University of Texas at Austin.
- UTCOMP Technical Documentation 3.8 (2011), The University of Texas at Austin.
- UTGEL Technical Documentation V.01 (2010), The University of Texas at Austin.
- Van Golf-Racht, T.D. (1982), *Fundamentals of fractured reservoir engineering*, Elsevier.
- Warren, J.E. and Root, P.J. (1963), The Behavior of Naturally Fractured Reservoirs, *SPE Journal*, 3(03), 245-255.
- Wu, Y. S. and Pruess, K. (1988), A Multiple-Porosity Method for Simulation of Naturally Fractured Petroleum Reservoirs, *SPE Reservoir Engineering*, 3(01), 327-336.
- Yu, W., Huang, S., Wu, K., Sepehrnoori, K., and Zhou, W. (2014), Development of a Semi-Analytical Model for Simulation of Gas Production in Shale Gas Reservoirs, SPE 1922945, SPE/AAPG/SEG Unconventional Resources Technology Conference, Denver, Colorado, USA, 25-27 August.
- Zhou, W., Banerjee, R., Poe, B.D., Spath, J., and Thambynayagam, M. (2014), Semi-analytical Production Simulation of Complex Hydraulic-Fracture Networks, *SPE Journal*, 19(01), 6-18.